LSU Master's Theses   Graduate School

2007

Evaluation of MVCT images with skin collimation for electron treatment planning

Allen Beardmore
Louisiana State University and Agricultural and Mechanical College

EVALUATION OF MVCT IMAGES WITH SKIN COLLIMATION FOR ELECTRON TREATMENT PLANNING

A Thesis

Submitted to the Graduate Faculty of the
Louisiana State University and
Agricultural and Mechanical College
in partial fulfillment of the
requirements for the Degree of
Master of Science

in

The Department of Physics & Astronomy

by
Allen Brown Beardmore
B.S. Furman University, 2004
August 2007

Acknowledgements

I thank the members of my thesis committee who put time and effort into making my project what it is. I especially thank my advisor, Dr. Rosen, who met with me and patiently discussed the project and encouraged me to continue to do my best. I thank Dr. Hogstrom for his guidance and expertise concerning electron beam treatment planning and Dr. Cheek for his helpfulness in answering my computer questions. I thank Eddie Singleton and Chad Dunn for taking time to teach me how better to use Pinnacle[3].

I thank my wife, Katie, who encouraged me the entire time I worked on this project. She has been a constant help by listening patiently as I try to explain what it is I do and offering positive feedback. She has helped me most by encouraging me to do everything for the glory of God.

I thank Mary Bird Perkins Cancer Center for the use of its facilities, especially the TomoTherapy Hi·Art unit and treatment planning computers. I thank the members of the staff of MBPCC for their willingness to assist me by answering my questions and accommodating my need of the treatment machines.

Table of Contents

List of Tables

List of Figures

ABSTRACT

Purpose: To evaluate the accuracy of electron beam dose calculations in MVCT images containing lead alloy masks.

Method and Materials: A phantom consisting of two 30x30x5 cm^3 slabs of CIRS plastic water® was imaged using kVCT (GE Lightspeed-RT) and MVCT (TomoTherapy Hi·Art). Nine MVCT scans were taken with different square masks of lead alloy (Cerrobend®, density = 9.4 $g \cdot cm^{-3}$) on top of the phantom. The masks contained square apertures of 3x3 cm^2, 6x6 cm^2 and 10x10 cm^2 and had thicknesses of 6 mm, 8 mm and 10 mm. The same collimation was simulated in the kVCT images by creating regions-of-interest (ROI) duplicating the sizes, shapes, and density of the masks. Using the Philips Pinnacle[3] treatment planning system, twelve treatment plans were created for the combination of four electron energies (6, 9, 12, and 16 MeV) and the three apertures. For each plan, the mask thickness appropriate for the electron energy was used and the dose distributions calculated using the kVCT and MVCT images were compared. In uniform dose regions dose differences were calculated; in high dose-gradient regions distances-to-agreement (DTA) were measured.

Results: In the uniform dose region, the maximum differences of doses in the MVCT images from doses in the kVCT images were greater than or equal to ±5% for all but one opening and energy combination. In the high dose-gradient region, more than half of the maximum DTA values exceeded 2 mm. Analysis of the MVCT images showed that the differences were largely due to two errors. First, the presence of the masks caused distortions in the MVCT numbers such that the calculated dose in the MVCT images penetrated less deeply. Second, distortion in the shape of the image of the collimation caused the calculation algorithm to scatter excess electrons into the central axis of the beam.

Conclusion: The presence of Cerrobend® masks in MVCT imaging produces distortions in the CT numbers that make electron beam dose calculations insufficiently accurate for electron beam treatment planning.

Chapter 1 Introduction

1.1 Function of skin collimation in treatment delivery

Surface (skin) collimation is often used in electron beam therapy for the purposes of sparing critical structures adjacent to the target by shaping the radiation beam and blocking leakage dose due to scattered electrons (Hogstrom *et al* 1991). Skin collimation is also used in conjunction with off-surface bolus (scatter plate) to restore the sharp beam penumbra after the beam has been scattered and the energy degraded by the scatter plate (Hogstrom *et al* 1991). Because of the superficiality of some cancers in the head and neck region and the importance of avoiding nearby critical structures, skin collimation is most often used in the treatment of cancers in this area. Cancers in the head and neck most often treated with electrons and requiring collimation include basal cell and squamous cell carcinomas of the eyelids, lip, tip of nose and ear (Tapley *et al* 1976). The accurate positioning of skin collimation within the beam is very important when setting up the patient for treatment. The skin collimation must have its inner edge inside the penumbra cast by the geometric (light) field edge of the uncollimated beam and its outer edge must extend well past the geometric field edge (Hogstrom *et al* 1991). This maintains the dose uniformity within the treatment field by narrowing the penumbra and, where used in conjunction with a scatter plate, protects the patient from dose from scattered electrons (Hogstrom *et al* 1991).

1.2 Incorporating skin collimation in treatment planning

For accurate dose calculation, the skin collimation must be accurately included in the treatment planning process. Current commercial treatment planning systems have neither accurate nor efficient method for doing this because of software limitations and problems in imaging with skin collimation.

There are two straightforward potential methods for adding skin collimation into the treatment planning process. The first method, currently used in the Mary Bird Perkins Cancer Center (MBPCC), is to manually draw the skin collimation onto the transverse CT images as an anatomic structure after the scan (Fig 1). After the structure has been created, its density can be changed to that of Pb (11.3 g·cm^{-3}) or Cerrobend$^{®}$ (9.4 g·cm^{-3}). However, this process is subjective, inaccurate, and time consuming. To my knowledge, no commercial treatment planning systems presently have software capabilities for easily adding skin collimation so that contours must be entered manually, slice by slice. The skin collimation can be contoured by following the outline of the patient surface which is clearly seen on the CT image (Fig 1). Most importantly, the beam-defining edges of the collimator must be correct on every slice, matching the daily setup. Uniformity of thickness of the collimation is not important so long as it stops the electron (in the clinic the actual masks used for daily treatments are of uniform thickness). The minimum thickness must equal or exceed the range of the electrons for the energy of the electron beam. Similarly, treatment planning systems have no methods for modeling the scatter plate so that it must be manually contoured, a task even more difficult than drawing the skin collimation. However, the problem of the scatter plate is not addressed in this research.
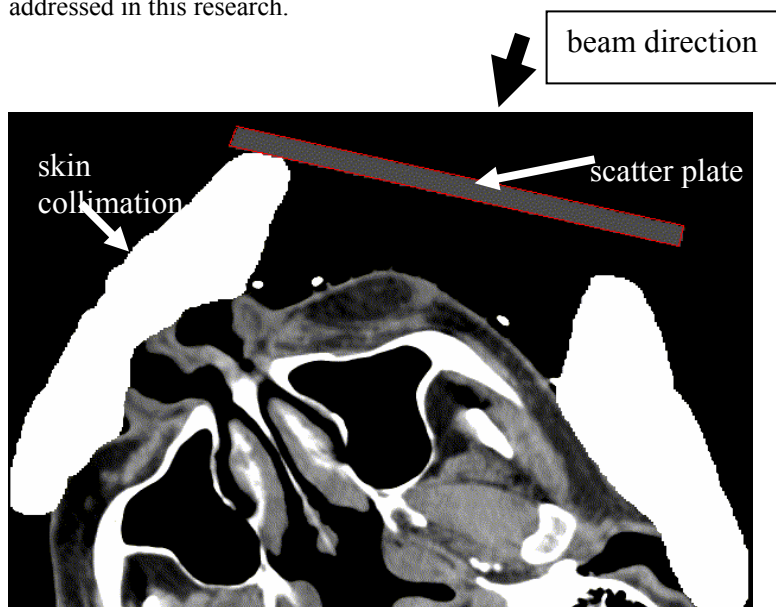
Figure 1. Skin collimation and scatter plate drawn onto the kVCT images in the treatment planning system.

A possible second method is to CT scan the patient with the constructed skin collimation in place so that it is contained in the image set. However, there is a physical limitation to the accuracy of this solution with conventional CT scanners because of the low photon energy of kVCT. Kilovoltage photons are greatly attenuated in the presence of high-Z materials such as Cerrobend® so that detector signals are very small for paths that transverse such materials (Coolens *et al* 2003). This high attenuation is not well modeled by conventional CT image reconstruction algorithms, resulting in extreme distortions and streak artifacts in the images (Yazdia *et al* 2005) (Fig 2). Dose calculations will therefore be inaccurate when using kVCT images acquired with skin collimation in place.

(a)   (b)
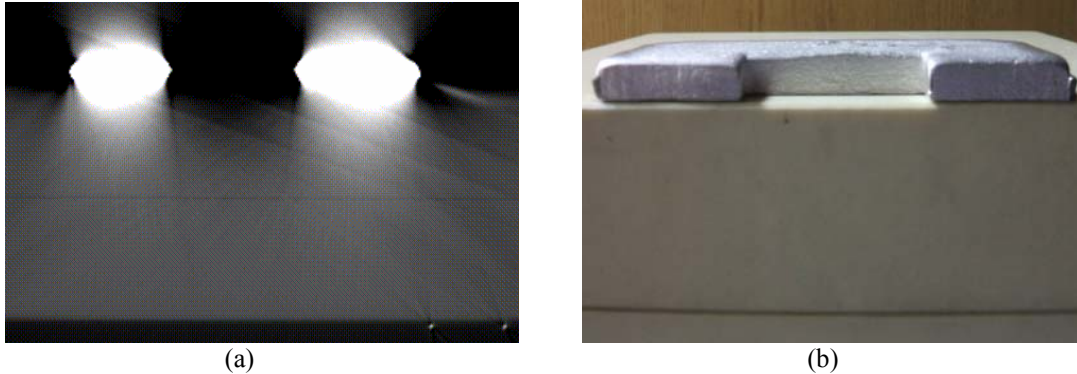
Figure 2. (a) Axial kVCT image of a CIRS plastic water® phantom with 1cm of Cerrobend® on top, demonstrating the streaking and distortions produced in kVCT images by high-Z materials; (b) photograph of phantom and Cerrobend®.

1.3 MVCT as a potential solution to treatment planning with skin collimation

It has been observed that high-density materials (e.g. aluminum, titanium, and copper) produce dramatically less distortion in MVCT images than in kVCT images (Ozer *et al* 2006, Meeks *et al* 2006). A potential solution to part of the problem of treatment planning with skin collimation is to scan the patient with the skin collimation in place using MVCT. This would avoid the inaccurate and time consuming process of manual contouring. Megavoltage photons are less attenuated by high-Z materials such as Cerrobend®, which means that more photons penetrate the skin collimation and are registered by the detectors. This produces more accurate reconstruction with conventional algorithms, giving more accurate CT numbers and less streaking artifacts. MVCT image sets are also more relevant for treatment planning because the CT numbers are directly related to electron density, making them more relevant than kVCT for dose calculations and inhomogeneity corrections (Ruchala *et al* 1999).

The TomoTherapy Hi·Art® system, one of which is owned by MBPCC, has an onboard MVCT scanner (3.5 MV) for image guided radiation therapy (IGRT). It is capable of scanning a patient and sending the images to a Philips Pinnacle[3] treatment planning system (TPS) for dose calculations. Figure 3 shows an image of the same setup as Figure 2 (plastic water® phantom with skin collimation) taken with TomoTherapy MVCT. The amount of streaking and image distortion normally due to high-Z Cerrobend® is dramatically reduced, clearly highlighting MVCT's potential usefulness. This improvement in image quality could potentially enable Monte Carlo algorithms or a recommissioned pencil beam redefinition algorithm (PBRA) to correctly calculate dose in the presence of multiple beam modifiers such as skin collimation and scatter plate.
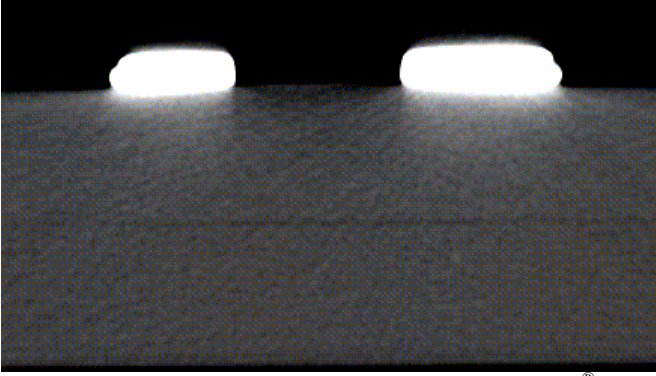
Figure 3. Axial MVCT image of a CIRS plastic water® phantom with 1cm of Cerrobend® on top, demonstrating reduced streaking and distortions in MVCT images with high-Z materials.

1.4 Purpose

        The goal of this research is to investigate the use of MVCT imaging of phantoms with skin collimation in place for the purpose of electron beam treatment planning.

1.5 Hypothesis

        The hypothesis of this research is that using MVCT images with skin collimation for treatment planning, doses delivered from 6-16 MeV electron beams can be calculated to ±5% dose difference agreement in the uniform-dose region and ±2mm distance-to-agreement in high dose-gradient regions compared to doses calculated using kVCT images with manually contoured skin collimation. The uniform dose region is defined as those doses $\geq$90% of the maximum dose along the central axis for a 10x10 cm^2 open field at 100 cm SSD and the high dose-gradient region is defined as 10%<doses<90% of the maximum dose along the central axis for a 10x10 cm^2 open field at 100 cm SSD.

1.6 Specific aims

        Aim 1. Construct CT number-to-density tables for MVCT and kVCT images.

        Aim 2. Compare dose calculations in MVCT and kVCT images of a plastic water phantom without skin collimation.

        Aim 3. Compare dose calculations in MVCT and kVCT images of a head phantom and patient without skin collimation.

        Aim 4. Construct Cerrobend® masks to simulate the range of dimensions of skin collimation used in the clinic.

        Aim 5. Compare doses calculated on MVCT images of a plastic water® phantom with skin collimation in place to doses calculated on kVCT images of the same phantom with skin collimation drawn onto the images during treatment planning.

Chapter 2 Aim 1

2.1 Aim 1: Construct CT number-to-density tables for MVCT and kVCT images
        TomoTherapy MVCT images are currently used for image-guided radiation therapy (IGRT) at MBPCC but not for clinical dose calculations. Consequently, there is no clinically available CT number-to-density conversion table. The purpose of this aim was to generate MV and kV CT number-to-density conversion tables for the dose calculations in Aims 2, 3 and 5.

2.2 Methods and materials
        A CIRS model 062 electron density phantom was scanned. This phantom is composed of an outer 'torso' and an inner 'head' section and has a series of plugs of known physical densities (Figs 4, 5). A CT scan of the phantom provided a relationship between CT number and physical density for both kVCT and MVCT images. The relationships are tabulated and entered into Pinnacle[3] for its dose calculations.
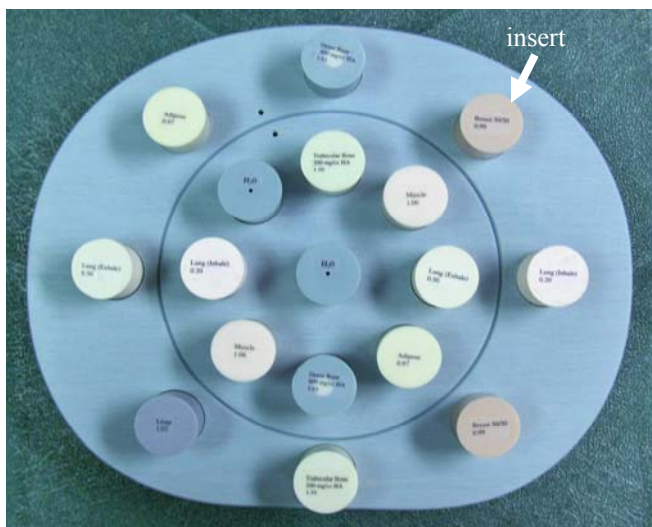
Figure 4. CIRS model 062 phantom.

2.2.1 MVCT density tables
        To create a measured MVCT number-to-density table, the CIRS 'torso' phantom was scanned two consecutive times using the "Fine" slice thickness (2 mm) on the TomoTherapy unit. The whole 'torso' was scanned rather than simply the 'head' in order to include the maximum number of inserts. The resulting images were transferred to Pinnacle[3]. Using the contouring tools of Pinnacle[3], a circular region-of-interest (ROI) was created within the image of each insert (Fig 5). The ROI was at least 5 mm in diameter and no bigger than 15 mm in diameter in order to sample a large number of pixels at the center of the insert and to avoid CT number variations at the edges of the 29.5-32.5 mm inserts. Pinnacle[3] calculated and reported the mean CT number in each ROI. The reported CT numbers from the two sets of scans were averaged and used to create a CT number-to-density table.

region-of-interest on insert
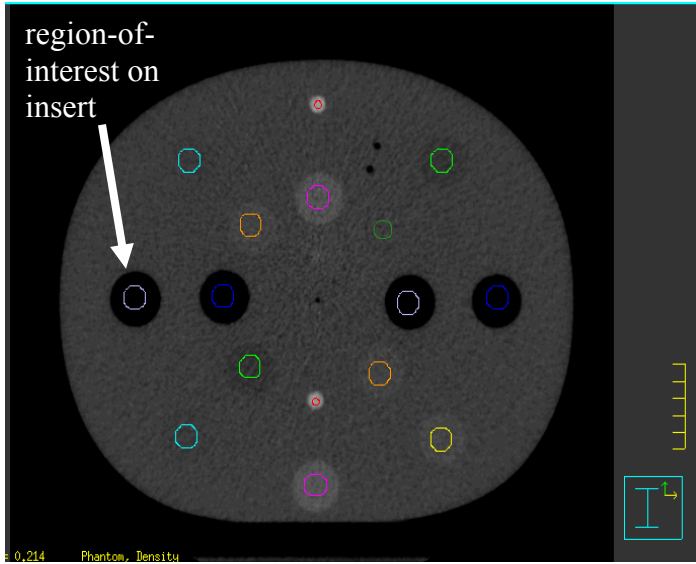
Figure 5. Axial MVCT image of CIRS model 062 electron phantom.

To minimize the effect of possible fluctuations in CT numbers between measurement days, scans of the CIRS phantom to generate CT number-to-density conversion tables were performed on the same days as the image sets were acquired for dose calculations. A total of four separate tables were created.

2.2.2 kVCT density tables

The CIRS phantom was scanned on the GE Lightspeed RT scanner to produce a kVCT number-to-density conversion table (Fig 6). The scanner was set at 120kVp and the slice thickness was 2.5 mm instead of 2 mm. The average of two scans taken on the same day was used for the CT numbers.
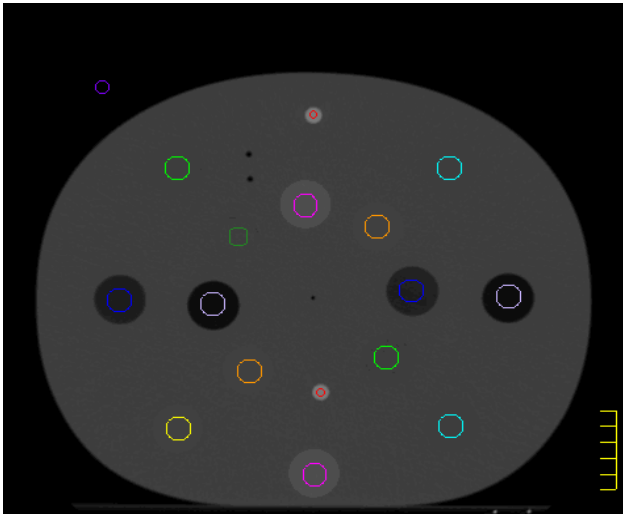
Figure 6. Axial kVCT image of CIRS model 062 electron phantom

2.3 Creation of aim-specific CT number-to-density tables

Three of the four tables created for the MVCT image dose calculations and the one table created for the kVCT image dose calculations were modified in order that the CT number for plastic water correctly predict its collision stopping power ratio. In calculating electron beam doses, Pinnacle[3] determines collision stopping power and angular scattering power ratios from physical density, which is determined from a CT number. Therefore, the physical densities in the CT number-to-density tables were altered to relate the proper collision stopping power and angular scattering power ratios to CT numbers. The stopping power for water $(S/\rho)_{water}$ for electrons is 1.968 MeV·g^{-1}·cm^2 and the stopping power for CIRS plastic $(S/\rho)_{plastic}$ for electrons is 1.971 MeV·g^{-1}·cm^2. This results in a relative stopping power of 1.002,

5

which in the Pinnacle[3] lookup table corresponds to a density of 0.981 MeV·g·cm^{-3} (Table 1). Therefore, in order for Pinnacle[3] to use the correct stopping power and angular scattering power ratios for the phantom calculations in Aims 2, 3 and 5, the densities in the CT number-to-density tables were modified by a correction factor that produced a density value of 0.981 for the phantom density.

Table 1. Patient collision stopping power and angular scattering power data.

Physical Density (g·cm^{-3})	Collision Stopping Power Ratio	Angular Scattering Power Ratio
0.000	0.001	0.001
0.291	0.311	0.292
0.927	0.933	0.729
1.000	1.027	0.912
1.047	1.051	1.040
1.100	1.098	1.135
1.427	1.422	1.863
1.940	1.940	3.026
2.900	11.300	11.900

2.3.1 Aim 2 and Aim 5 modified tables

The modified MVCT number-to-density table used for Aim 2 was created from the table measured on November 21, 2006. A CIRS plastic water® phantom, consisting of two slabs of size 30x30x5 cm^3, was scanned on the same day and an ROI was drawn in the center to obtain a mean CT number. The mean CT number was 1032, which corresponded to a density value of 1.020 g·cm^{-3}. Therefore, the densities in the range from 0.967 g·cm^{-3} to 1.07 g·cm^{-3} were scaled by a factor of 0.964 (=0.981/1.020). This same factor was applied to the same range of densities for the MVCT number-to-density tables used for the dose calculations done in Aim 5.

The modified kVCT number-to-density table used for Aim 2 was similarly modified. The mean CT number measured for the plastic water phantom was 1075, which corresponded to a density value of 1.080 g·cm^{-3}. Therefore, densities in the kVCT table in the range from 0.495 g·cm^{-3} to 1.16 g·cm^{-3} were scaled by a factor of 0.910 (=0.981/1.080).

2.3.2 Aim 3 modified tables

The modified MVCT number-to-density table used for Aim 3 was created from the table measured on November 28, 2006. The CIRS model 065 radiosurgery head phantom was scanned on the same day and an ROI drawn in a section of soft tissue to obtain a mean CT number. The mean CT number was 1066, which corresponded to a density value of 1.063 g·cm^{-3}. Therefore, the densities in the range from 0.967 g·cm^{-3} to 1.07 g·cm^{-3} were scaled by a factor of 0.923 (=0.981/1.063).

The modified kVCT number-to-density table was created in the same way except that the mean CT number was 1032, which corresponded to a density value of 1.032 g·cm^{-3}. Therefore, densities in this table in the range from 0.967 g·cm^{-3} to 1.07 g·cm^{-3} were reduced by a factor of 0.950 (=0.981/1.03).

2.4 Results

Four MVCT number-to-density conversion tables were measured and three modified tables were created. Each table was date-specific, meaning that it was used to calculate doses only for the images acquired on the same day as the measurement of the table. The measured tables show good consistency over the fifteen days that the data were acquired (Table 3). The table used to calculate dose in the patient (November 13, 2006) was not modified. The modified data are shown in Table 3. The measured kVCT number-to-density conversion table and its modified version are shown in Table 4.

Table 2. MV CT number-to-density data.

Material	Physical Density (g·cm⁻³)	CT number Nov, 13 2006	CT number Nov, 17 2006	CT number Nov, 21 2006	CT number Nov, 28 2006	Mean and standard deviation
vacuum	0	0	0	0	0	0 ± 0
air	0.001	2	4	4	1	3 ± 1.5
lung (inhale)	0.195	231	232	232	232	232 ± 0.5
lung (exhale)	0.495	504	508	504	507	506 ± 2.1
adipose	0.967	974	974	974	977	975 ± 1.5
breast	0.991	1008	1011	1008	1013	1010 ± 2.5
water	1.000	1022	1020	1017	1019	1020 ± 2.1
muscle	1.062	1060	1064	1061	1065	1063 ± 2.4
liver	1.071	1076	1077	1076	1080	1077 ± 1.9
trabecular bone	1.161	1148	1148	1146	1151	1148 ± 2.1
dense bone	1.609	1504	1508	1506	1507	1506 ± 1.7

Table 3. Modified MV CT number-to-density tables.

Material	Physical density (g·cm⁻³)	Aim 2 modified physical density (g·cm⁻³) Nov 21, 2006	Aim 3 modified physical density (g·cm⁻³) Nov 28, 2006	Aim 5 modified physical density (g·cm⁻³) Nov 17, 2006	Aim 5 modified physical density (g·cm⁻³) Nov 28, 2006
vacuum	0.000	0.000	0.000	0.000	0.000
air	0.001	0.001	0.001	0.001	0.001
lung (inhale)	0.195	0.195	0.195	0.195	0.195
lung (exhale)	0.495	0.495	0.495	0.495	0.495
adipose	0.967	0.929	0.893	0.933	0.932
breast	0.991	0.952	0.915	0.956	0.955
water	1.000	0.961	0.923	0.965	0.964
muscle	1.062	1.021	0.980	1.025	1.024
liver	1.071	1.029	0.989	1.034	1.032
trabecular bone	1.161	1.161	1.161	1.161	1.161
dense bone	1.609	1.609	1.609	1.609	1.609

Table 4. Measured and modified kV CT number-to-density data.

Material	CT number	Physical density (gcm^{-3})	Aim 2 modified physical density (gcm^{-3})	Aim 3 modified physical density (gcm^{-3})
vacuum	0	0	0	0
air	2	0.001	0.001	0.001
lung (inhale)	223	0.195	0.195	0.195
lung (exhale)	495	0.495	0.479	0.495
adipose	939	0.967	0.880	0.919
breast	976	0.991	0.902	0.941
water	1008	1.000	0.910	0.950
muscle	1054	1.062	0.966	1.009
liver	1062	1.071	0.975	1.017
trabecular bone	1242	1.161	1.057	1.161
dense bone	1927	1.609	1.537	1.609

Chapter 3 Aim 2

3.1 Aim 2: Compare dose calculations in MVCT and kVCT images of a plastic water phantom

The goal of Aim 2 was to determine the accuracy of electron dose calculations when using MVCT images of a plastic water phantom with no skin collimation (no high-Z distortions).

3.2 Methods and materials

Two slabs of 30x30x5 cm^3 CIRS plastic water$^®$ were stacked on top of each other to produce a flat surface, water-like phantom that could easily be CT scanned on the GE Lightspeed RT and on the TomoTherapy MVCT unit. This phantom was scanned once on each machine, and the resulting image sets were exported to Pinnacle[3] (Fig 7).
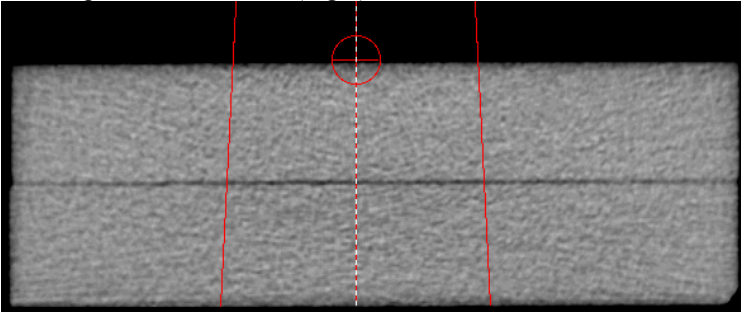
Figure 7. Axial MVCT image of a CIRS plastic water phantom image with the geometry of a 10x10 cm^2 beam.

3.2.1 Treatment planning

Two simple treatment plans were created on each image set. The first plan was a 9 MeV beam perpendicular to the phantom with an open 10x10 cm^2 applicator and a prescription of 100 monitor units (MUs) delivered at 100 cm SSD. The second plan had the same parameters and prescription except its energy was 16 MeV. Calculated doses were extracted from the kVCT and MVCT image sets by aligning the posterior edge of the dose grid to the posterior edge of the phantom in order to avoid surface distortion (Figure 8). The dose grid had the same dimensions for each set of images.

The vertical coordinate of the posterior edge of the phantom in both image sets was determined using a two step process. First, the couch was removed from the image set by contouring an ROI aligned to the surface of the couch and overriding the density to be that of air. Second, a point-of-interest (POI) and a posterior beam were created. The beam isocenter was set at the POI and then the SSD of the beam was set to 100 cm (Figure 8). Pinnacle[3] has a default threshold density value of 0.60 g/cm^3 for identifying the surface of the patient. In determining SSD, Pinnacle[3] ray-traces along the central axis of the beam from the source until it encounters a voxel with density above the threshold value. Therefore, the first central-axis voxel with density above the threshold was taken as the posterior edge of the phantom. This method was used because it puts the dose grid in the same position relative to the phantom regardless of possible distortions in the anterior surface.
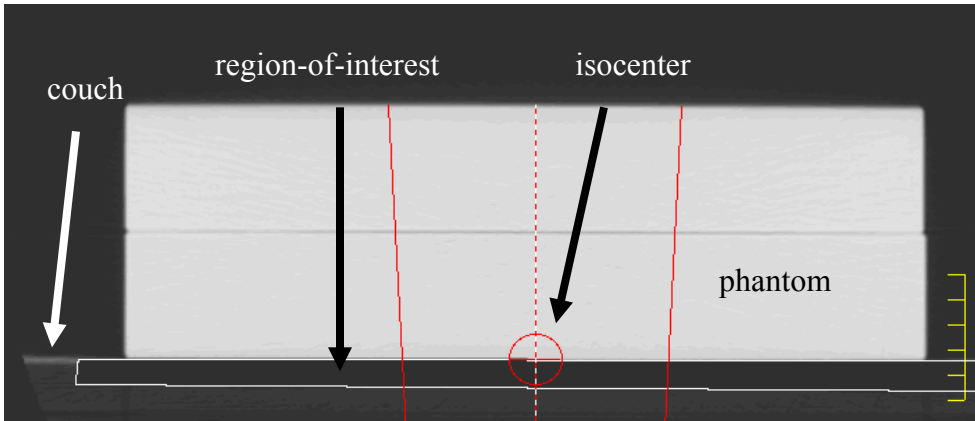
Figure 8. CT scan of plastic water phantom in which the couch was removed by setting its density to 0.000 g·cm^3. The isocenter point is the intersection of a posterior beam at 100 cm SSD with the phantom surface.

Two-dimensional dose matrices were exported from Pinnacle[3] to SigmaPlot®. Isodose curves and central-axis depth-dose curves were generated in SigmaPlot®. For comparison purposes, these curves were aligned with respect to the back edge of the plastic water®, which corresponded to the back edge of the dose grid (Figure 9). Because the dose grid was 15.8 cm in the anterior-posterior direction and the phantom was 10 cm in the same direction, the first 5.8 cm of the dose matrix were subtracted in order to align the isodose curves. This assured that the 0 cm depth for the depth dose and isodose curves corresponded to the surface of the plastic water® in the kVCT image set. The following is the equation used to determine the phantom's surface (i.e. 0.0 cm in SigmaPlot®) with PS defined as phantom surface, DG defined as the length of the dose grid in the anterior-posterior direction, PT defined as the phantom thickness in the same direction and FG defined as the front coordinate of the dose grid, placed at -5.8:
$PS = DG - PT + FG$.
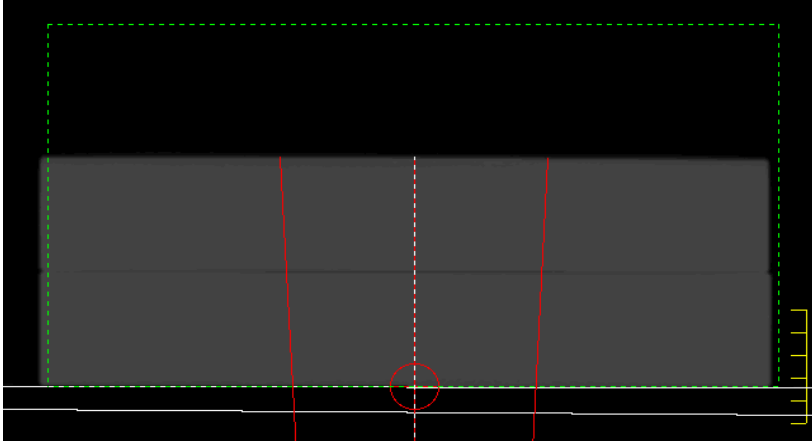
Figure 9. The dose grid (green dash line) on a kVCT image with the posterior edge at the posterior edge of phantom.

3.2.2 Comparison methods

For each beam energy, the MVCT isodose distributions and central-axis depth dose curves were superimposed onto the kVCT curves for visual comparison. Dose differences between the two matrices were computed in SigmaPlot® by subtracting the MVCT calculated doses from those of the kVCT. Dose differences were only evaluated in the uniform-dose region. The range of dose differences was extracted and recorded.

Distance-to-agreement (DTA) was determined for high dose-gradient regions by manual measurement with a ruler normal to the superimposed isodose distributions. The maximum DTA for each comparison was recorded. The uniform dose region is defined as those doses ≥90% of the maximum dose along the central-axis for a 10x10 cm^2 open field at 100 cm SSD and the high dose-gradient region is defined as 10%<doses <90% of the maximum dose along the central-axis for a 10x10 cm^2 open field at 100 cm SSD.

3.3 Results

The superimposed isodose distributions and depth doses are shown in Figures 10-13. The positions of maximum dose difference are identified with a red ellipse. The positions of maximum DTA are identified with a blue ellipse. The ranges of dose differences and maximum DTAs are shown in Table 4. As can be seen the dose differences and DTAs fell within the hypothesis criteria for both energies (<5% and ±2 mm, respectively).

10
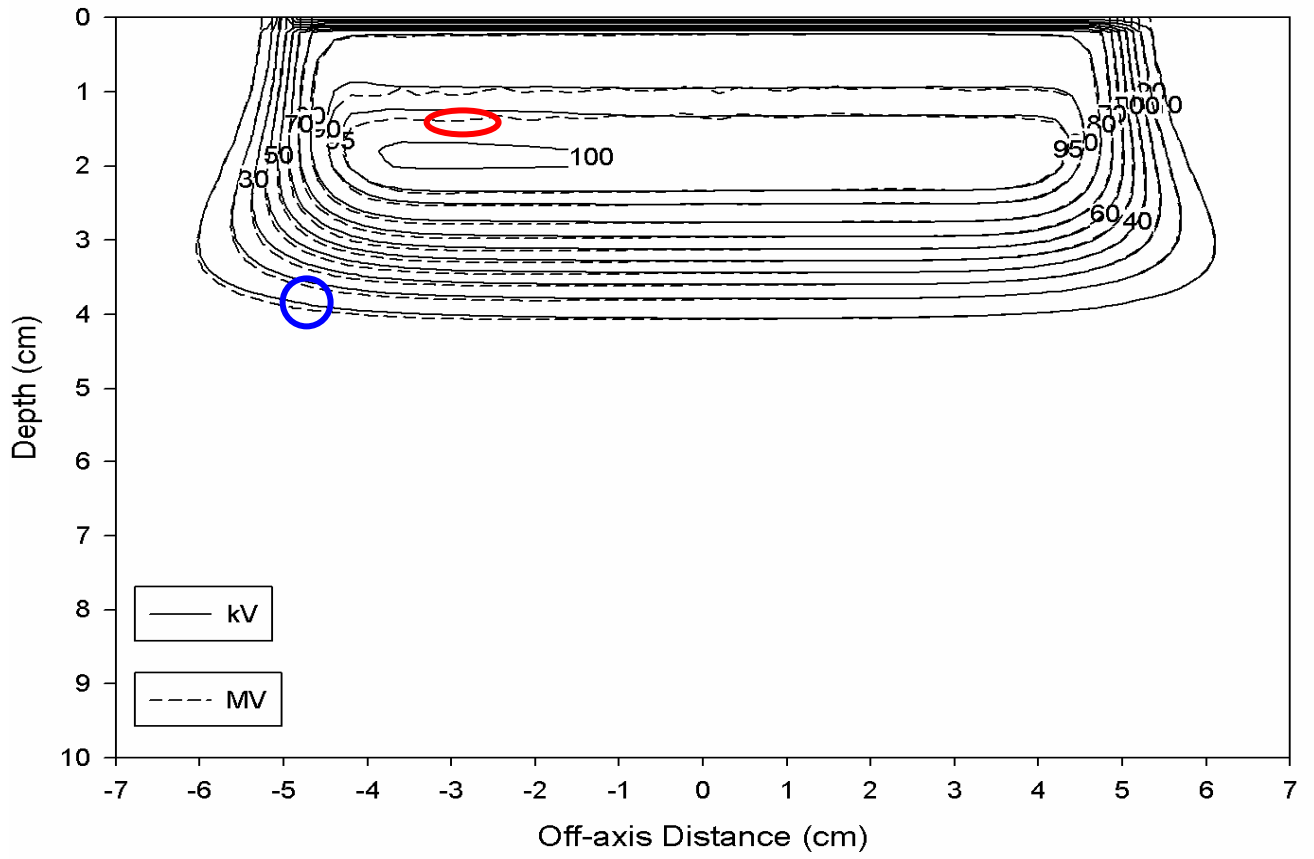
Figure 10. 9 MeV isodose curves computed on MVCT and kVCT images. The field size was 10x10 cm^2 and the SSD = 100 cm.
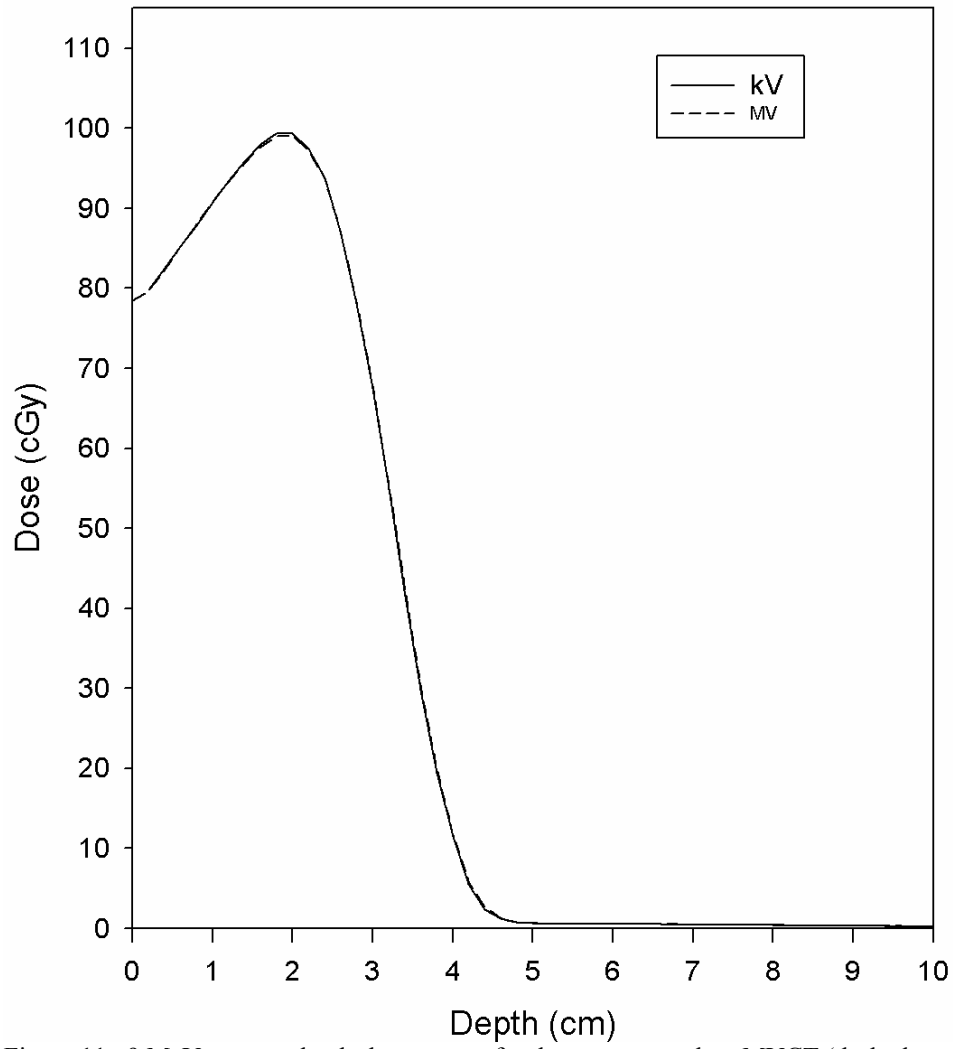
Figure 11. 9 MeV percent depth-dose curves for doses computed on MVCT (dashed curve) and kVCT (solid curve) images.
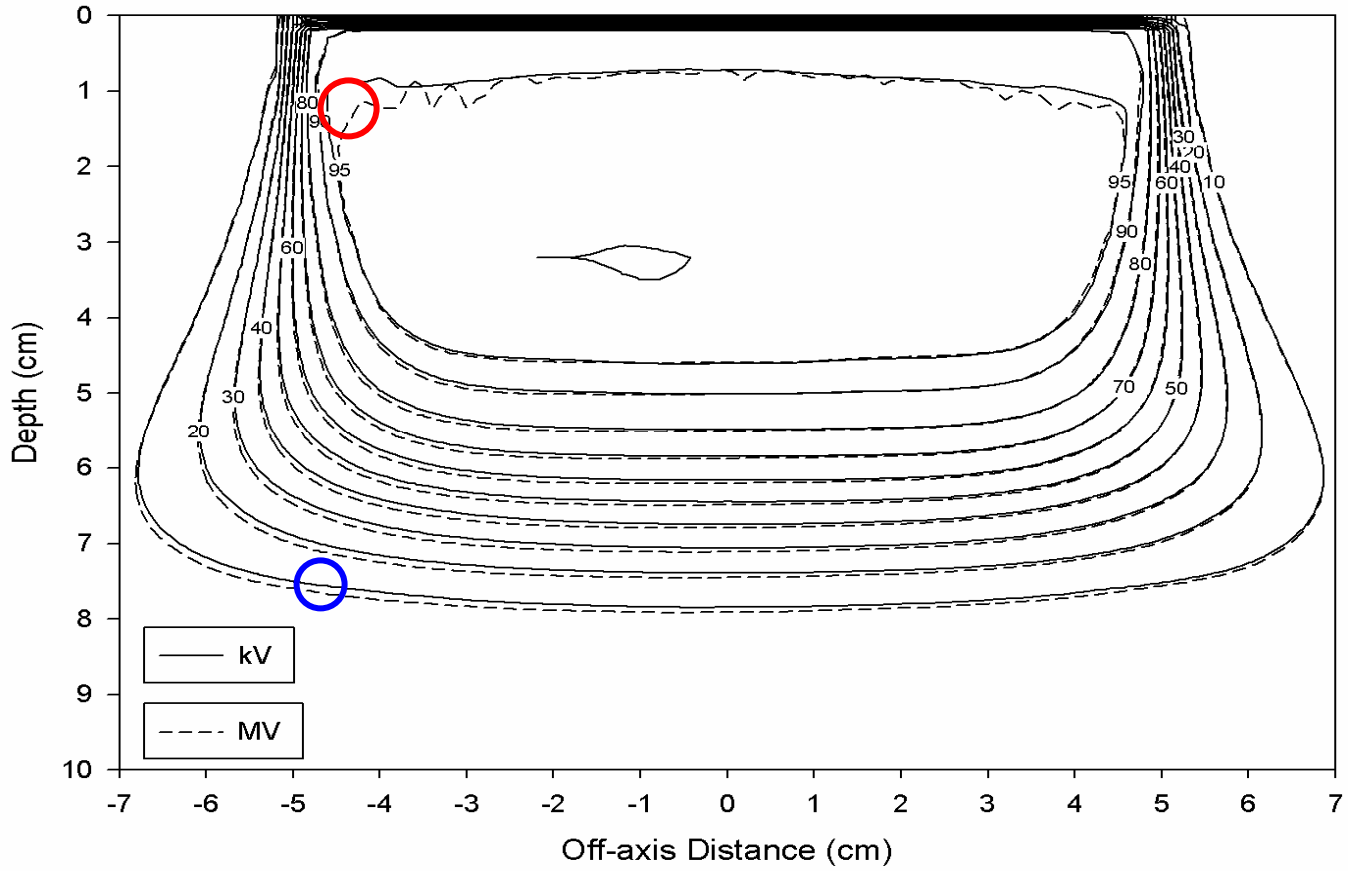
Figure 12. 16 MeV isodose curves computed on MVCT and kVCT images. The field size was 10x10 cm^2 and the SSD = 100 cm.
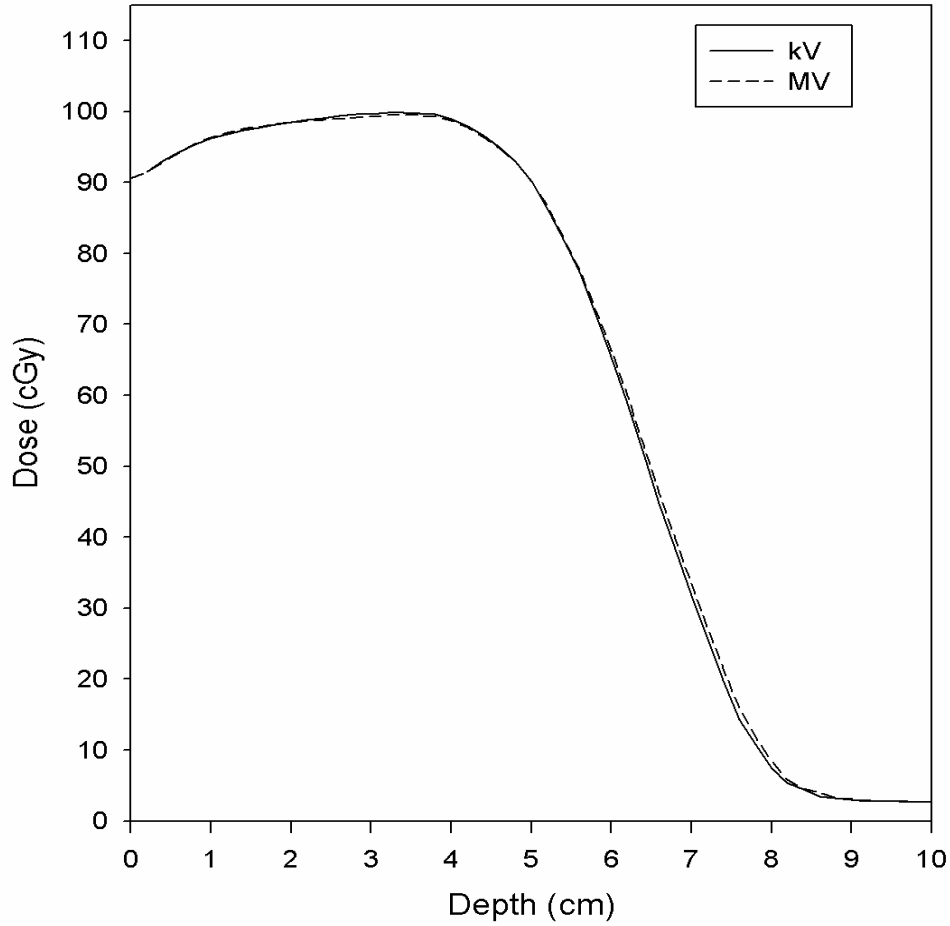
Figure 13. 16 MeV depth-dose curves for doses computed on MVCT (dashed curve) and kVCT (solid curve) images.

Table 5. Ranges of dose differences in the uniform-dose region and maximum DTAs in high dose-gradient regions.

Energy	Ranges of dose differences (%) (uniform-dose region)	Maximum DTA (mm) (gradient regions)
9 MeV	[2.2, -1.3]	0.8
16 MeV	[2.3, -1.2]	1.2

3.4 Conclusion

The results demonstrated that TomoTherapy MVCT images for a plastic water phantom can produce electron beam dose calculations clinically equivalent as those produced from kVCT images.

Chapter 4 Aim 3

4.1 Aim 3: Compare dose calculations in MVCT and kVCT images of a head phantom and patient
       The goal of Aim 3 was to evaluate the accuracy of electron beam dose calculations in MVCT images of an anthropomorphic head phantom and a patient case, both without high-density skin collimation.

4.2 Methods and materials
       A radiosurgery head phantom, CIRS model 605, was chosen to provide a CT data set for phantom dose calculations (Fig 14). This phantom was scanned once on a GE Lightspeed RT machine (2.5 mm slice thickness) and once on a TomoTherapy MVCT unit (2.5 mm slice thickness). Both image sets were exported to a Pinnacle[3] workstation for treatment planning (Figs 15, 16). The advantage of using a head phantom is that the anatomy is physically the same in both the kVCT and MVCT scans and the images could be taken with the same slice thickness.

Figure 14. Photograph of CIRS model 605 radiosurgery head phantom.
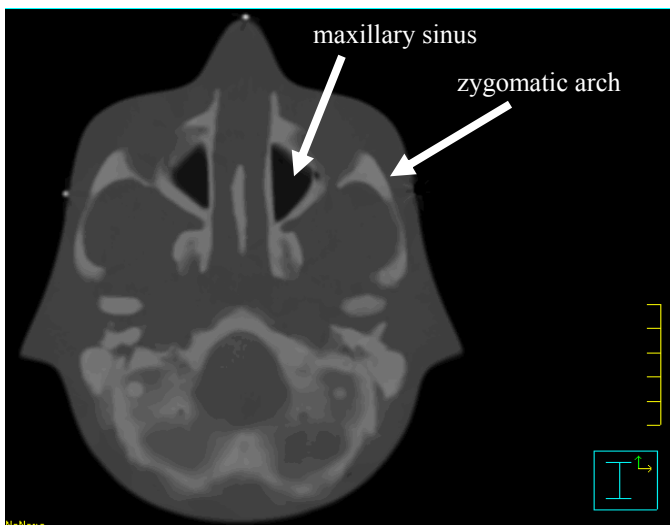
Figure 15. Axial kVCT image of CIRS model 605 radiosurgery head phantom with labeled anatomy. This slice was chosen for the central axis of the electron beam.
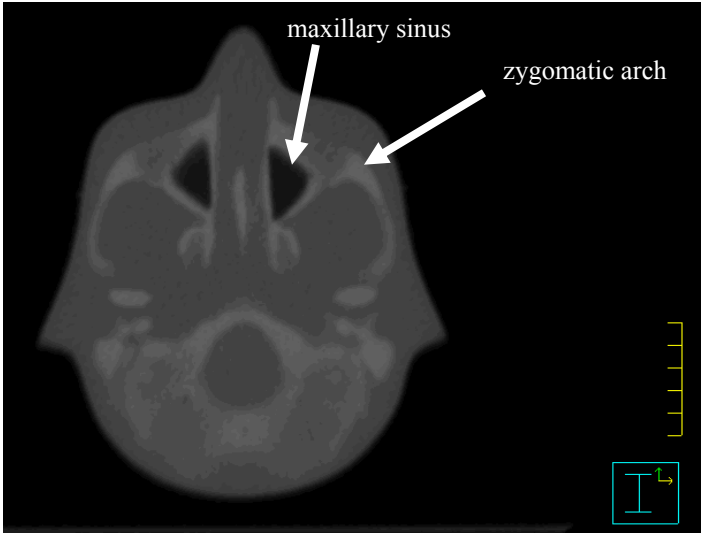
Figure 16. Axial MVCT image of CIRS model 605 radiosurgery head phantom with labeled anatomy. This slice was chosen for the central axis of the electron beam.

Doses were also calculated on MVCT and kVCT images of a patient. The selected patient had a squamous cell carcinoma of the floor of tongue, had been scanned on a GE Lightspeed (2.5 mm slice thickness), and was currently undergoing radiation treatment on the TomoTherapy system. The daily MVCT scan (4 mm slice thickness) taken for IGRT was selected. Both the kVCT and MVCT images were exported to a Pinnacle[3] workstation. The kVCT image set was changed to make a new image set with a slice thickness of 5 mm. This was done by averaging two slices to make one. This reduced some of the potential effects that different slice thicknesses could have on the dose calculation comparison. Because the two image sets were taken approximately 2 months apart, some anatomical differences were observed (Figs 17, 18). The clinical kVCT number-to-density conversion table was used for kVCT dose calculations. The MVCT number-to-density conversion table created on November 13 was used for dose calculation purposes.
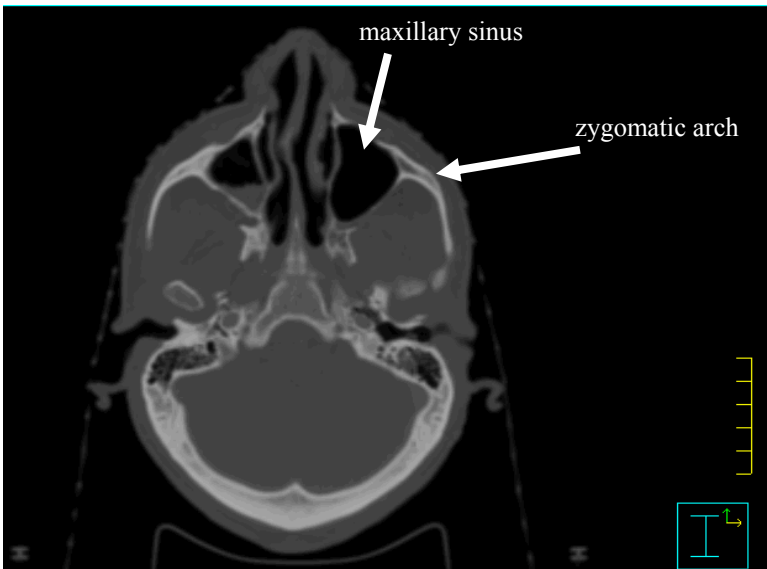
Figure 17. Axial kVCT image of the patient. This slice was chosen for the central axis of the electron beam.
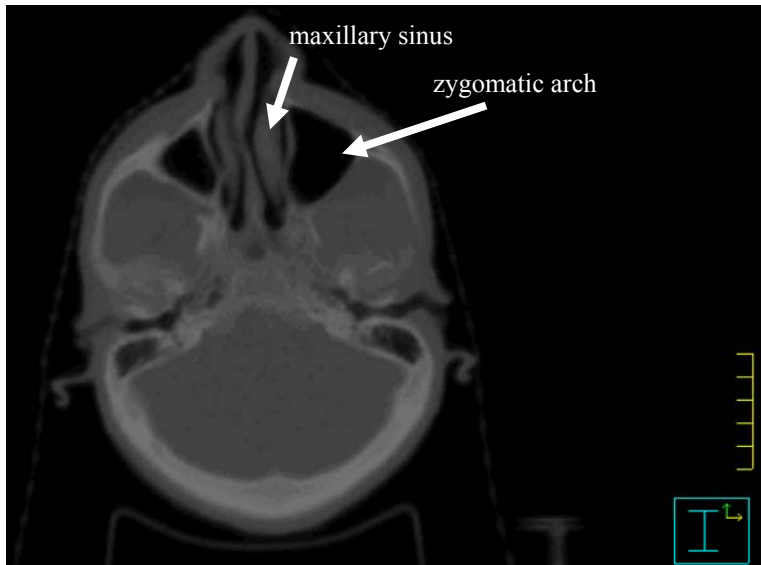
Figure 18. Axial MVCT image of the patient. This slice was chosen for the central axis of the electron beam.

4.2.1 Image registration

In Pinnacle[3] the two phantom and two patient image sets were manually registered using the Image Fusion module. The fusion process in Pinnacle[3] can be done automatically using a local correlation algorithm. However, manual registration was used for two reasons. First, both image sets must have the exact same treatment delivered. Therefore, any rotation during registration must be known exactly because the angle of the gantry with respect to the image must be the same. The automatic registration algorithm does not give the rotation information. Second, the software used to generate isodose curves from the exported dose grid information (SigmaPlot® 9.0) does not have a rotation capability for its two dimensional contour graphs, so the degree of rotation of the automatic fusion could not be matched even if the amount were known. In the manual registration process, no rotations were used and the fusion of the images was done using anatomy in the region of treatment.

4.2.2 Phantom and patient treatment planning

The head phantom and patient CT images were treated with the same setup. The axial slices chosen for the central axes (CAX) of the beams included both bone and air inhomogeneities and had anatomy conducive to manual registration of the kVCT and MVCT image sets (Figs. 15-18). Two simple treatment plans were created on each image set. Both plans were open beams with a 6x6 cm^2 applicator at a gantry angle of 125° and an SSD of 100 cm. One was a 9 MeV beam and the other a 16 MeV beam. The oblique angle for this beam was chosen to include both bone and air heterogeneities. The prescription was set to 100 MUs.

Calculated doses were compared in the axial slice containing the isocenter of the beam. Doses were not evaluated in superior or inferior slices for the patient for two reasons. First, the patient's head was not in exactly the same location for both the kVCT and MVCT scans and, therefore, image sets could only be accurately registered in one slice by using the anatomy in the region of treatment. Second, because the kVCT and MVCT scans had different slice thicknesses, the closest superior and inferior slices that were at the same physical locations were 2cm above and below the isocenter. This distance increased the inaccuracies associated with registration of local anatomy. The dose grid information for each axial slice was exported to Sigma Plot® and isodose plots were generated.

4.2.3 Comparison methods

The maximum dose differences in the uniform region were calculated by subtracting the MVCT calculated dose matrix from the kVCT calculated dose matrix and then finding the differences with the largest absolute values.

4.3 Results

4.3.1 Phantom treatment plans (9, 16 MeV)

Figures 19-24 show the central axis axial slices of the kVCT and MVCT image sets with the isodose curves, beam profile and isocenter displayed in order to give proper anatomical orientation to the

17

corresponding isodose curves displayed in SigmaPlot®. On the SigmaPlot® overlays, the position of maximum dose difference is indicated by a red ellipse. The position of maximum DTA is indicated by a blue ellipse.
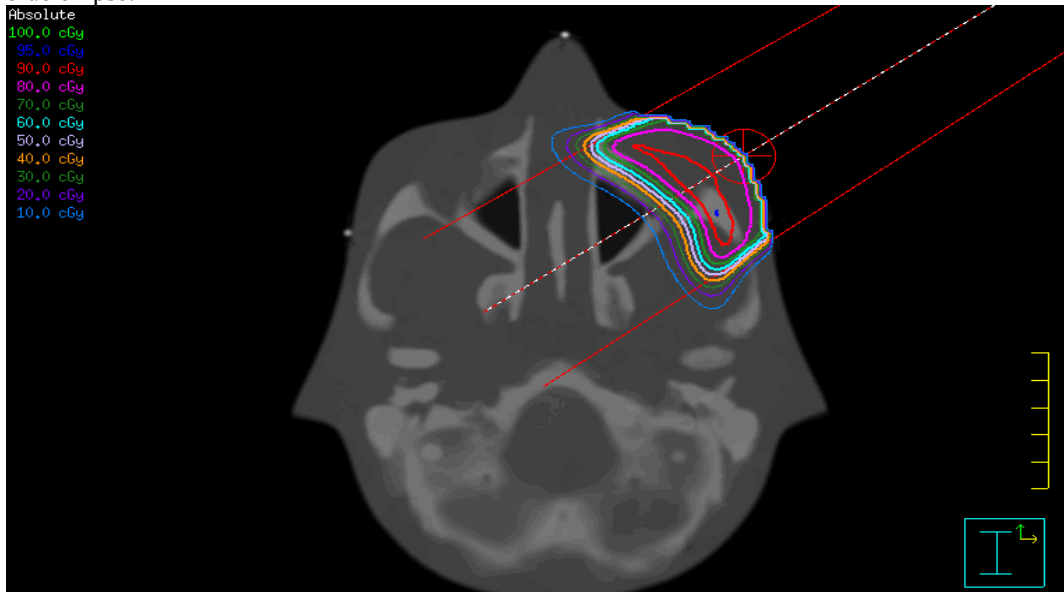
Figure 19. Axial kVCT image of head phantom with isodose curves, beam profile, and isocenter (9 MeV).
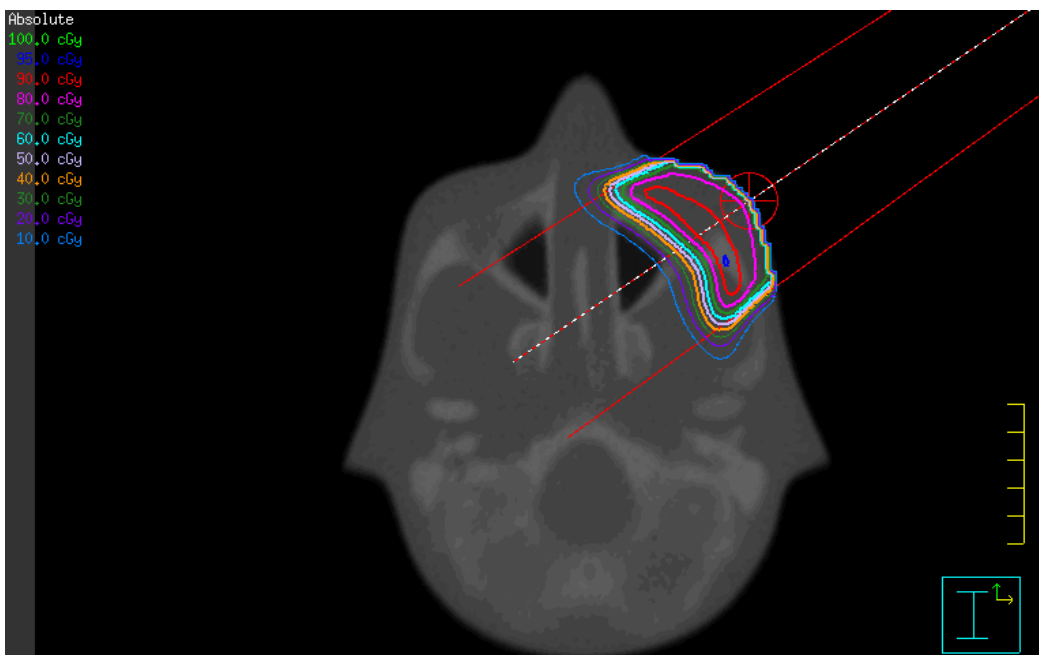
Figure 20. Axial MVCT image of head phantom with isodose curves, beam profile, and isocenter (9 MeV).
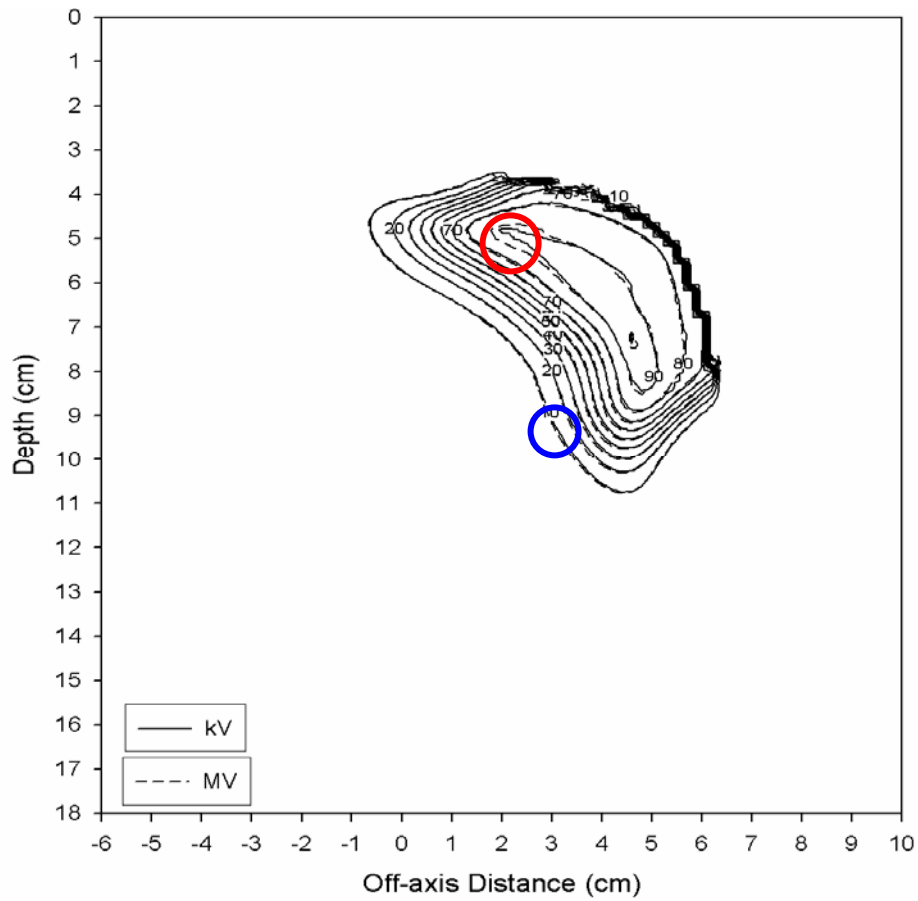
Figure 21. Isodose curve comparison for phantom case (9 MeV). The red ellipse indicates the position of maximum dose difference. The blue ellipse indicates the positions of maximum DTA.

Figure 22. Axial kVCT image of head phantom with isodose curves, beam profile, and isocenter (16 MeV).
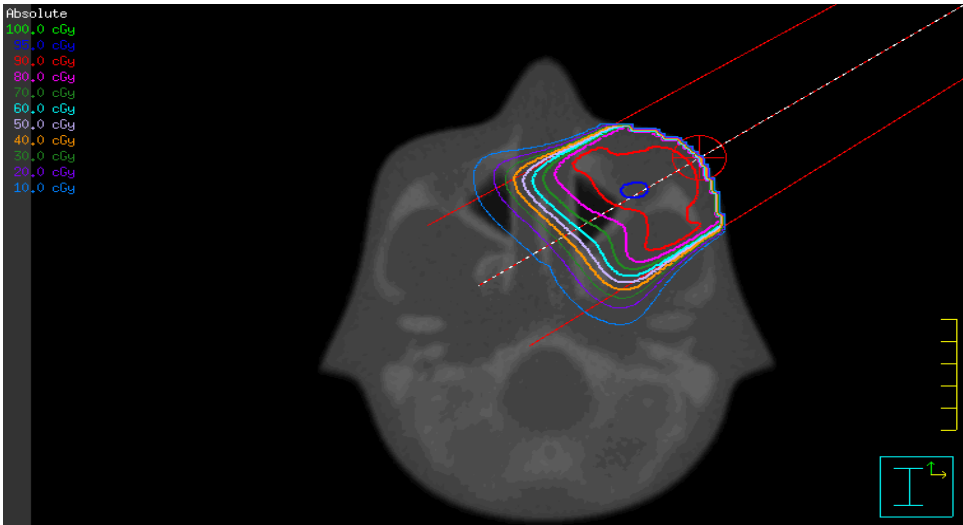
Figure 23. Axial MVCT image of head phantom with isodose curves, beam profile, and isocenter (16 MeV).

Figure 24. Isodose curve comparison for phantom case (16 MeV). The red ellipse indicates the position of maximum dose difference. The blue ellipse indicates the positions of maximum DTA.

The ranges of dose differences in the uniform region were calculated by subtracting the MVCT calculated dose matrix from the kVCT calculated dose matrix and then finding the differences with the largest absolute values. The results are shown in Table 6. Both the low energy (9 MeV) and the high energy (16 MeV) beams meet the hypothesis criteria of ±5% dose difference in the uniform region and ±2 mm DTA in the high dose-gradient region. These results are similar to the plastic water® case.

Table 6. Ranges of dose differences for the head phantom in the uniform region and maximum DTAs in the high dose-gradient regions.

Energy	Ranges of dose difference (%) (uniform-dose region)	Maximum DTA (mm) (gradient regions)
9 MeV	[1.2, -2.0]	0.5
16 MeV	[4.3, -2.0]	1.0

4.3.2 Patient treatment plans (9, 16 MeV)

Figures 25-30 show the central axis axial slices of the kVCT and MVCT image sets of the patient with the isodose curves, beam profile and isocenter displayed in order to give proper anatomical orientation to the corresponding isodose curves displayed in SigmaPlot®.
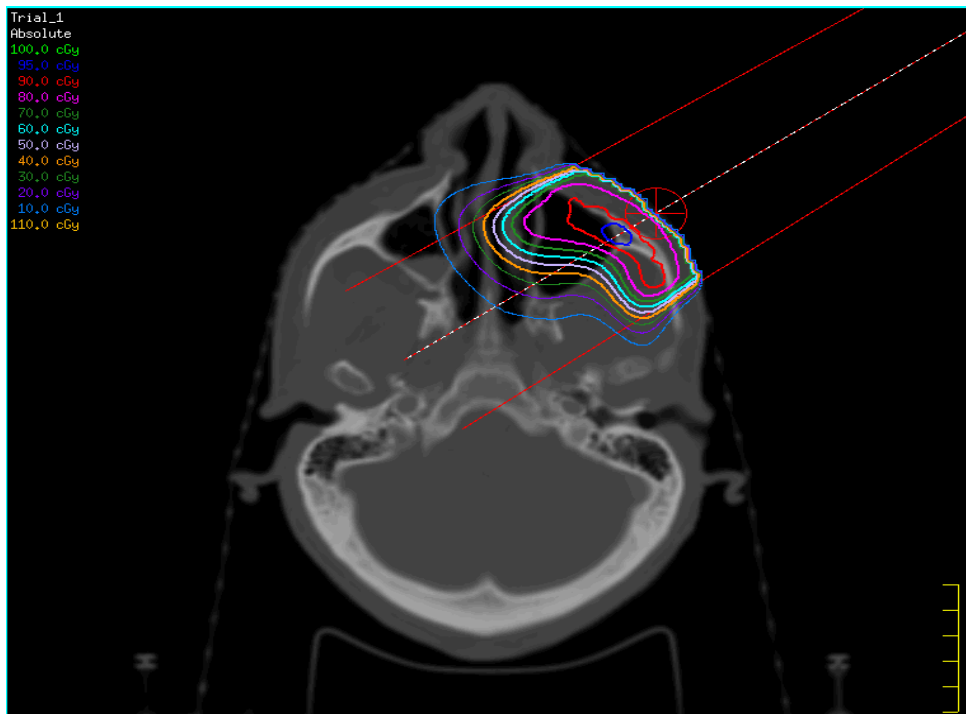
Figure 25. Patient's central axis kVCT slice with isodose curves (9 MeV).
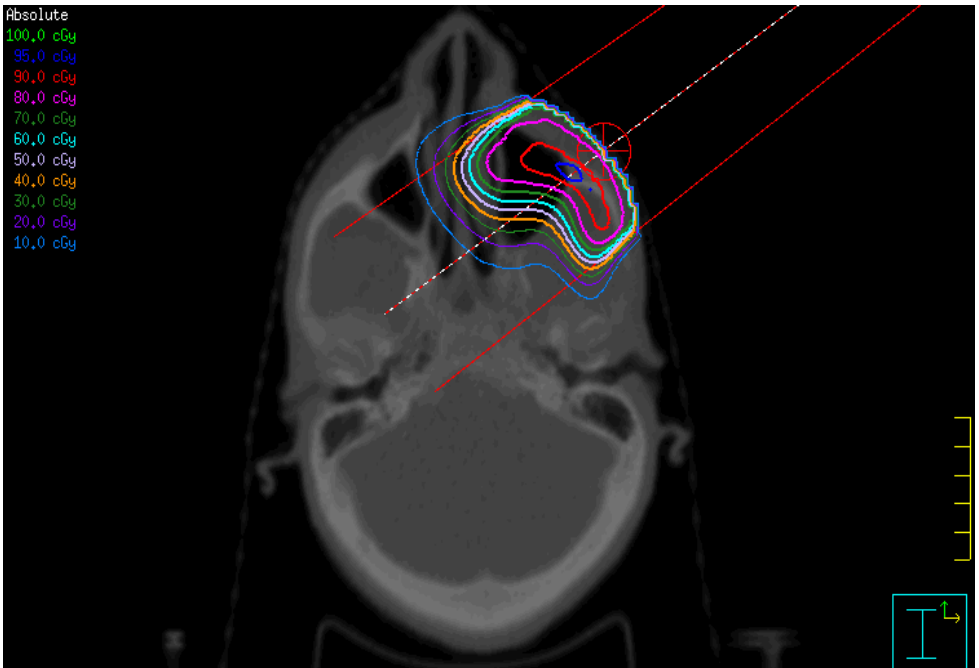
Figure 26. Patient's central axis MVCT slice with isodose curves (9 MeV).
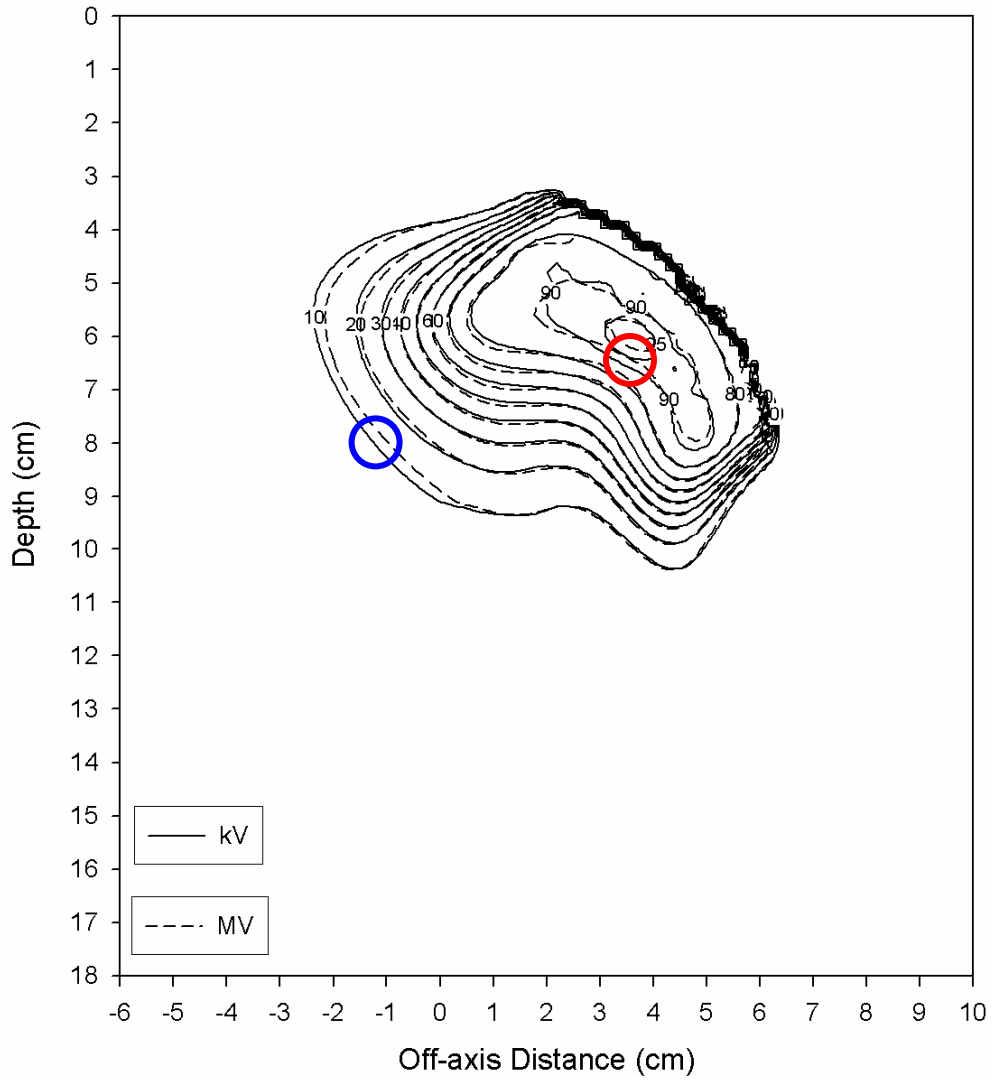
Figure 27. Isodose curve comparison for patient case (9 MeV). The red ellipse indicates the position of maximum dose difference. The blue ellipse indicates the positions of maximum DTA.
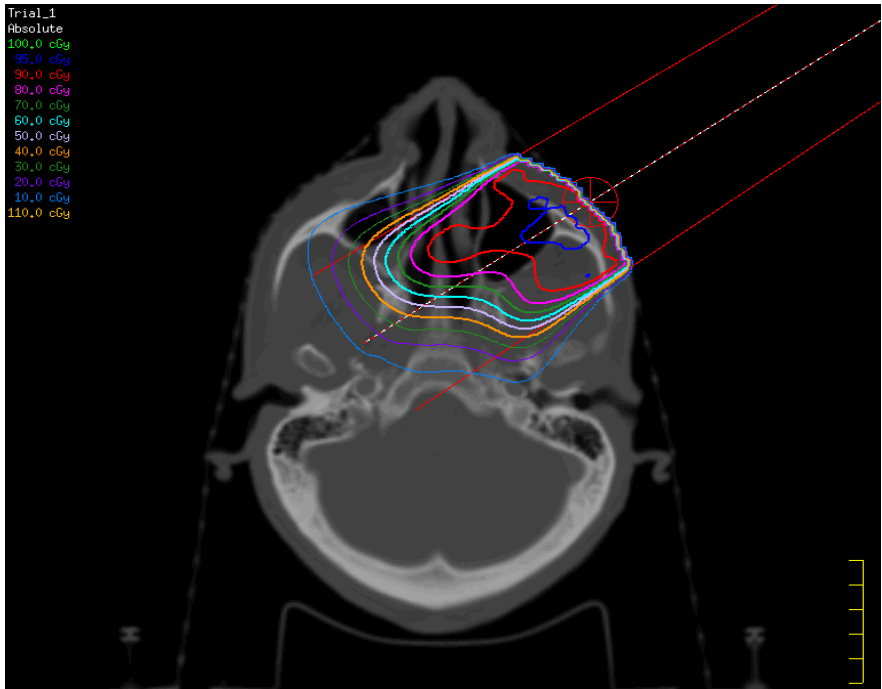
Figure 28. Patient's central axis kVCT slice with isodose curves (16 MeV).
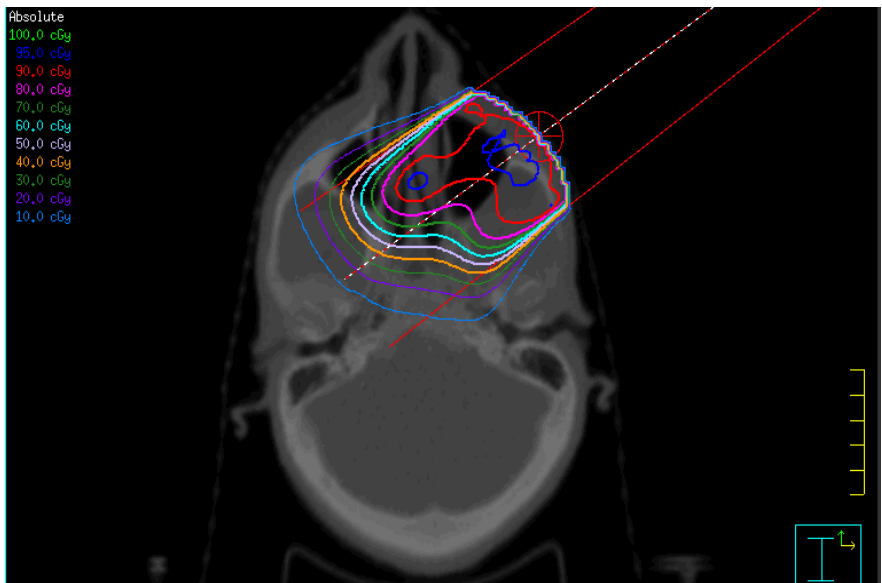
Figure 29. Patient's central axis MVCT slice with isodose curves (16 MeV).
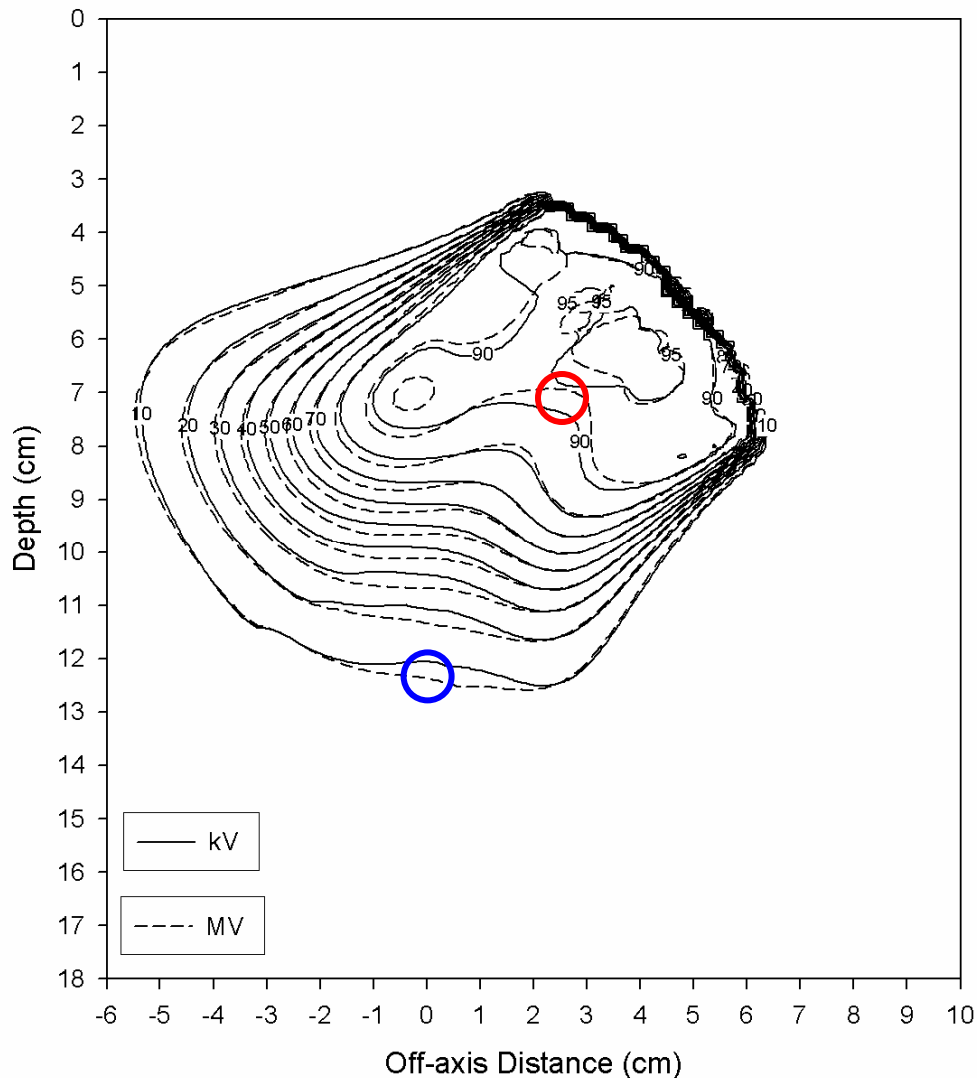
Figure 30. Isodose curve comparison for patient case (16 MeV). The red ellipse indicates the position of maximum dose difference. The blue ellipse indicates the positions of maximum DTA.

The range of dose differences in the uniform region was calculated by subtracting the MVCT calculated dose matrix from the kVCT calculated dose 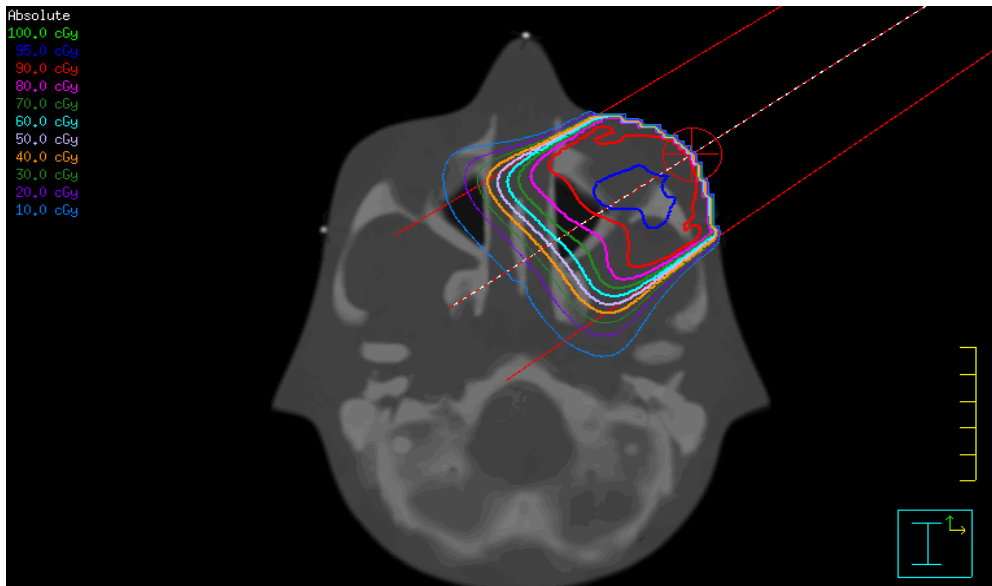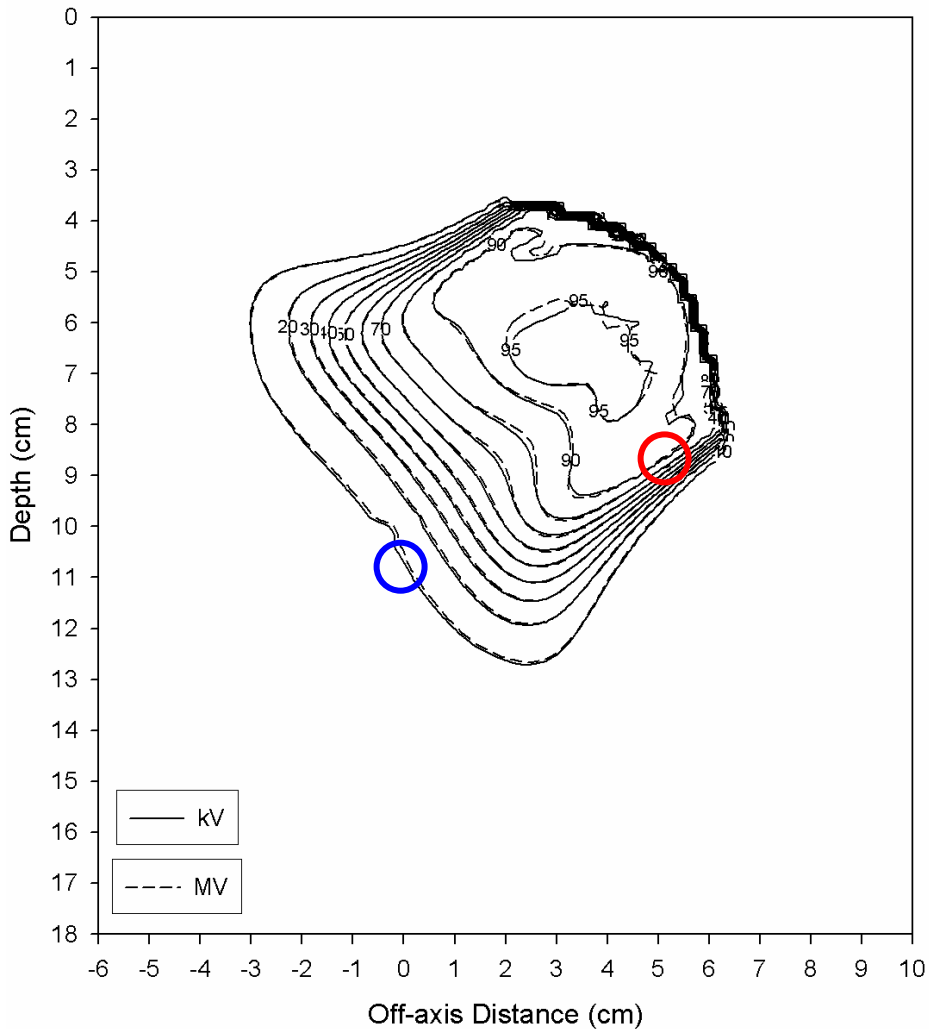matrix and then finding the differences with the largest absolute values. The results are shown in Table 7. Both the low energy (9 MeV) and the high energy (16 MeV) beams meet the hypothesis criteria of ±5% dose difference in the uniform region. These results are similar to the phantom case.

The maximum DTA for doses less than 90% of maximum exceeds ±2 mm for both energies (Table 7). It is important to note that the DTA which did not meet the ±2 mm criteria were found at the 10% isodose lines. Not only is this region not as clinically relevant as the target region but this disparity may be the results of anatomical changes. Because the patient was scanned on the Lightspeed machine approximately 2 months prior to the TomoTherapy unit scan, it is possible that the anatomy changed to the point where dose calculations were affected. That this is true at least in some regard is seen by examining the patient's right maxillary sinus on the kVCT and MVCT scans. In the kVCT image the sinus is partially filled with fluid while in the MVCT image the fluid is not present. While this does not directly impact the dose calculation in the region of the target, it suggests that there were changes in anatomy that could have affected the dose calculations. Also, the difference in slice thicknesses may have caused inaccuracies in the dose calculations. Results from attempting to quantify this possibility were inconclusive as the patient was not able to be scanned at 2.5 mm slice thickness on the TomoTherapy unit.

Table 7. Ranges of dose differences for the patient in the uniform region and maximum DTAs in the high dose-gradient regions.

Energy	Ranges of dose difference (%) (uniform-dose region)	Maximum DTA (mm) (gradient regions)
9 MeV	[4.4, -2.4]	3.0
16 MeV	[4.0, -2.5]	3.9

4.4 Conclusions

4.4.1 Phantom study

The results for the phantom study indicate that calculated doses from electron beams in complex geometrical cases are accurate in MVCT images between 9 MeV and 16 MeV. The higher energy case results were slightly worse than for those of the low energy case but still fell well within the hypothesis criteria.

4.4.2 Patient study

The results for the patient study suggest that calculated doses from electron beams are not accurate in MVCT images. Both energies failed the hypothesis criteria in having DTA that were greater than 2mm. However, it is highly likely that the major cause of the dose disagreements was either a change in the anatomy between the time of kVCT imaging and MVCT imaging or slice thickness difference. The DTA values are outside the target, essentially by definition. The dose differences in the target were within ±5%.

Chapter 5 Aim 4

5.1 Aim 4: Construction of Cerrobend® masks to simulate the range of skin collimation used in the clinic

Cerrobend® masks were needed for testing MVCT images with skin collimation (Aim 5). Clinically used masks were studied and a set of representative test masks was made for use in Aim 5.

5.2 Methods and materials

5.2.1 Clinical masks

A typical patient Cerrobend® mask is shown in Fig 31. The important characteristics of a mask are the opening size, the thickness, and the lateral extent. The opening size is critical and is determined by the size of the treatment area. The thickness is determined by the beam energy. It must equal or exceed the minimum thickness needed to stop the electron beam. The lateral extent of the mask is not a precisely defined dimension. It needs to be large enough to meet the minimum shielding criteria and not so large as to be uncomfortable for the patient.
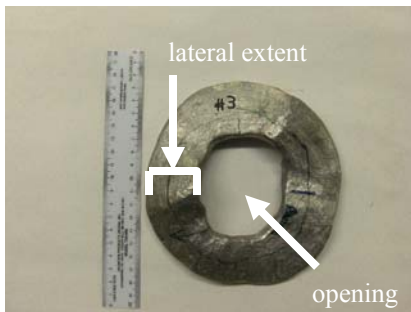
Figure 31. Photograph of typical clinical Cerrobend® mask.

However, we expect that the amount of Cerrobend® on the patient will directly impact the quality of the MVCT image. The size of the opening affects the portion of the CT image in the path of the beam, with smaller openings having a greater impact than larger openings (Fig 32, 33). Therefore, it is important to perform testing with masks that represent the range of clinical situations.
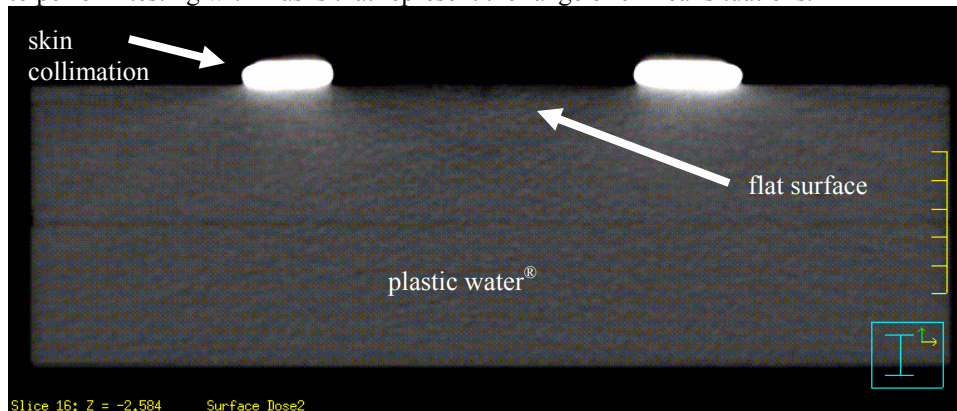
Figure 32. Cerrobend® mask with a 10x10 cm^2 opening on the surface of CIRS plastic water®.
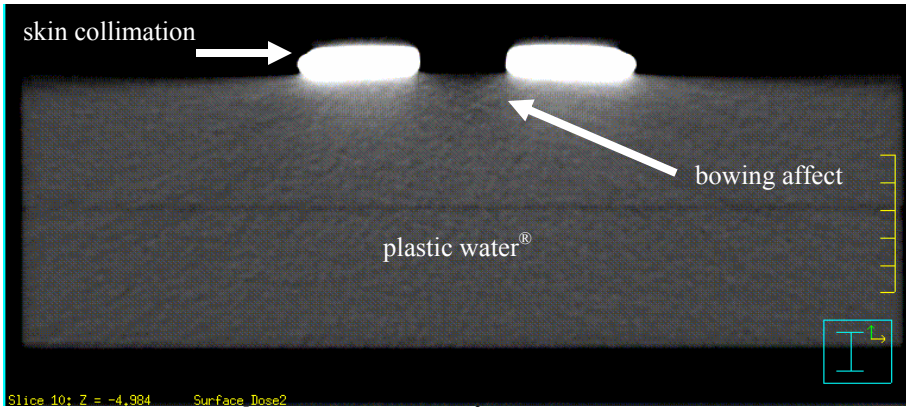
Figure 33. Cerrobend® mask with a 3x3 cm^2 opening on the surface of CIRS plastic water®.

Twelve clinical Cerrobend® masks used for patient treatment were collected, measured, and characterized. The opening size was approximated as an ellipse and its major and minor axes dimensions were measured. The lateral extent was measured at each end of the major and minor axes. Masks with very small openings, such as those used for treatments involving the eyelid, were not included because in such cases the monitor units (MUs) are calculated by hand instead of using treatment planning software.

5.2.2 Construction of test masks

Three styrofoam squares were cut by the Compu●cutter® system with sizes of 3x3 cm^2, 6x6 cm^2 and 10x10 cm^2. These squares were placed inside steel frames of size 10x10 cm^2, 15x15 cm^2 and 15x15 cm^2 respectively. Cerrobend® was poured around the foam squares and made to the desired thickness (6 mm, 8 mm, and 10 mm) required for adequate shielding for energies of 6, 9, 12, and 16 MeV (Fig 34). This process produced a total of nine square masks with clinically relevant opening sizes, lateral extensions and thicknesses (Table 8).
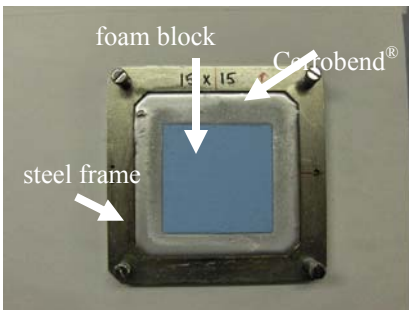
Figure 34. Cerrobend® mask formed within the steel frame and around a styrofoam insert.

Table 8. Constructed mask dimensions.

Mask number	Opening size (cm^2)	Lateral extent (cm)	Thickness (mm)
1	3x3	3.5	6
2	6x6	4.5	6
3	10x10	2.5	6
4	3x3	3.5	8
5	6x6	4.5	8
6	10x10	2.5	8
7	3x3	3.5	10
8	6x6	4.5	10
9	10x10	2.5	10

5.3 Results

The characteristics of the individual clinical masks are given in Table 9. As can be seen, the dimensions varied considerably. The data are summarized in Table 10, which shows the maximum, minimum and average values for the lateral extent and opening size. These values guided the dimensions of the Cerrobend® masks produced in this aim for the tests of Aim 5. Smaller dimensions were chosen for the lateral extent of the test masks with respect to the clinical sizes because clinical masks are often made larger than necessary in this region to avoid any possible shielding problems. Examples of the test masks are shown in Figures 35-38.

Table 9. Dimensions of clinical Cerrobend® masks.

Clincial mask dimensions	Opening	size (cm)	Lateral	extent (cm)
Mask number	major axis	minor axis	major axis ends	minor axis ends
1	7.5	5.0	5.0 , 5.5	4.5 , 6.0
2	8.0	7.0	4.0 , 3.5	4.5 , 4.0
3	7.0	6.0	4.5 , 4.0	4.5 , 4.5
4	8.0	6.0	5.0 , 5.0	5.0 , 5.0
5	11.0	10.0	3.0 , 4.0	3.0 , 4.0
6	13.0	6.0	4.5 , 3.5	5.5 , 5.0
7	2.5	2.0	5.0 , 7.0	5.0 , 5.5
8	4.0	2.0	6.0 , 4.0	6.0 , 5.0
9	6.0	6.0	6.0 , 6.0	6.5 , 5.0
10	12.5	8.0	3.0 , 3.0	4.0 , 4.0
11	4.5	4.0	3.5 , 3.5	3.5 , 3.5
12	6.0	3.5	3.5 , 4.0	4.0 , 4.0

Table 10. Maximum, minimum and mean clinical mask dimensions.

Clinical mask data	Maximum distance (cm)	Minimum distance (cm)	Mean distance (cm)
Lateral Extent			
major axis	7.0	3.0	4.4
minor axis	6.0	3.0	4.7
Opening Size			
Major axis	13.0	2.5	7.5
minor axis	10.0	2.0	5.5

Figure 35. Photograph of a mask with a 3x3cm^2 opening.

Figure 36. Photograph of a mask with a 6x6 cm^2 opening.

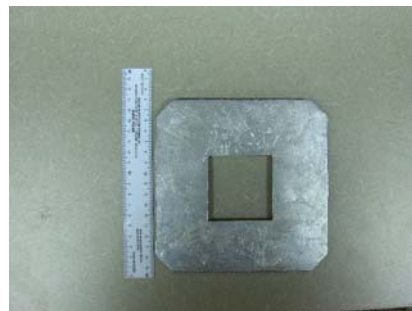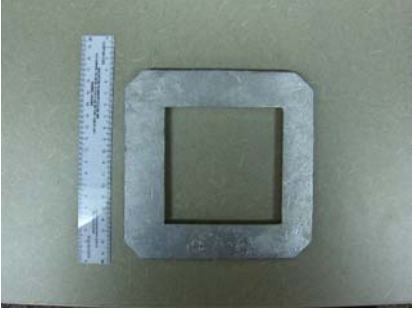Figure 37. Photograph of a mask with a 10x10 cm^2 opening.

Figure 38. Photograph showing a 6 mm thick mask next to a 10 mm thick mask.

Chapter 6 Aim 5

6.1 Aim 5: Comparison of dose calculations in MVCT and kVCT images with skin collimation.
        The purpose of this aim was to evaluate the accuracy of dose calculations in MVCT images with skin collimation.
6.2 Methods and materials
        Two slabs of 30x30x5 cm^3 CIRS plastic water® (density=1.03g·cm^{-3}), used clinically for machine QA, were stacked on top of each other to provide a simple geometry phantom that could easily be CT scanned with or without the Cerrobend® masks.
6.2.1 kVCT treatment planning
        The two slabs were scanned on a GE Lightspeed RT machine (120 kvp, 2.5 mm slice thickness) and exported to a Pinnacle^3 workstation. In Pinnacle^3, regions-of-interest (ROIs) were created on the surface of the phantom to mimic the nine different masks created in Aim 4 (Fig 39). Because only one image set was used in Pinnacle^3 and a total of nine different treatment fields needed to be simulated, the treatment planning was performed in stages. After each collimation ROI was formed, the corresponding treatment field was created, the dose was calculated, and the result was exported to SigmaPlot®.

(a)   (b)
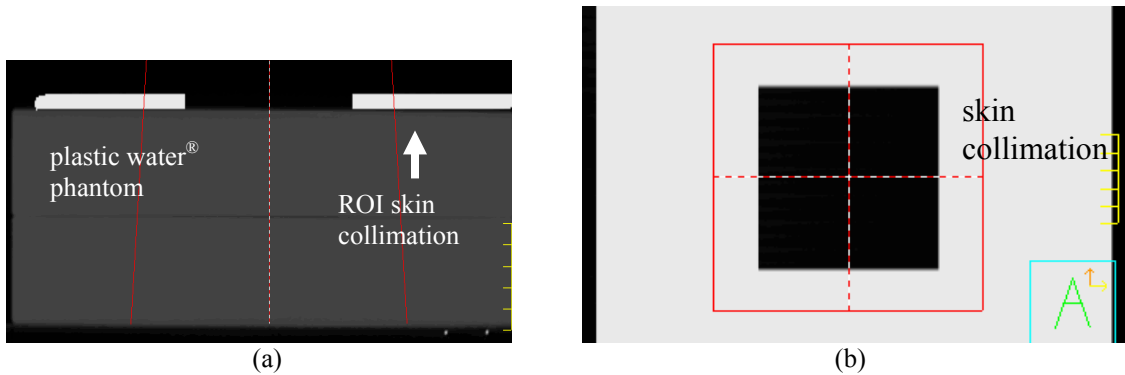
Figure 39. (a) Axial view of ROI Cerrobend® in kVCT image; beam edges are in red. (b) Beam's eye view of ROI Cerrobend® in kVCT image; beam outline is in red.

        Two important modifications were made to ensure that the ROIs behaved as skin collimation in the dose calculations.   The first modification required creating a special table in Pinnacle^3 for computing stopping power ratios and scattering power ratios from patient density. Pinnacle^3 uses a look-up table to convert densities to collision stopping power and angular scatter power ratios for the purpose of electron dose calculation. However, Pinnacle^3 limits densities in this table to a maximum value of 3 g·cm^{-3}. This is not high enough to correctly model Cerrobend®. Collision stopping power and angular scattering power ratios for Cerrobend® were chosen to be 11.3 and 11.9 respectively based on work done previously by Dr. Kenneth Hogstrom[12]. The workaround for this problem was to insert those values into the table for a corresponding density value of 2.9 g·cm^{-3} (Table 11). These values would allow Pinnacle^3 to terminate the transport of electrons through the ROIs mimicking Cerrobend®. The second modification was to make the density of the ROI equal to the highest density value allowed by Pinnacle^3 (3 g·cm^{-3}).

Table 11. Patient collision stopping power and angular scattering power data.

Physical Density (g·cm⁻³)	Collision Stopping Power Ratio	Angular Scattering Power Ratio
0.000	0.001	0.001
0.291	0.311	0.292
0.927	0.933	0.729
1.000	1.027	0.912
1.047	1.051	1.040
1.100	1.098	1.135
1.427	1.422	1.863
1.940	1.940	3.026
2.900	11.300	11.900

6.2.2 MVCT treatment planning

The two slabs were also scanned with each of the nine Cerrobend® masks on the TomoTherapy unit and exported to the Pinnacle³ treatment planning station. This was completed over a period of two days. For each day an MVCT number-to-density table was created as mentioned in Aim 1. Figure 40 shows one of the masks on the plastic water® phantom.
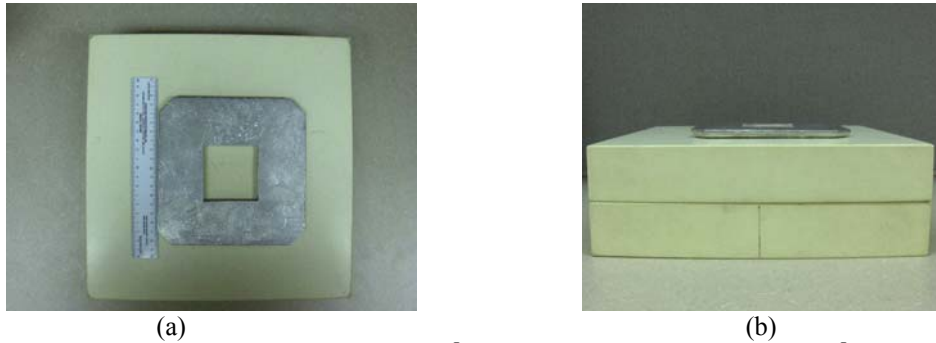

<center>(a)   (b)</center>

Figure 40. (a) Beam's eye view of Cerrobend® mask on top of CIRS plastic water® phantom. (b) Lateral view of Cerrobend® on top of CIRS plastic water® phantom.

6.2.3 Density versus depth

The penetration of a radiation beam in a given material depends in part on the density of that material. The density of an object that has been CT scanned is determined by converting the measured CT number to a density according to a CT number-to-density calibration curve. Therefore, distortions in imaging that cause changes in the CT numbers will result in corresponding density changes and corresponding changes in calculated doses.

In order to assess the impact of the skin collimation on the distortion of density, density was measured as a function of depth along the central axis of the treatment beams. Because of inherent noise in the images, CT numbers were averaged within ROIs created on the kVCT image set and on each MVCT image set to provide a mean density (Fig 41). A total of 16 ROIs were created on image sets with treatment beams of 6-12 MeV and 20 ROIs were created on image sets with a 16 MeV beam. The ROIs were cuboids with dimensions of 1x0.4 cm² and a thickness equal to the slice thickness. The mean density was computed in each of these ROIs using Pinnacle³ and assigned to the depth at the center of the ROI.
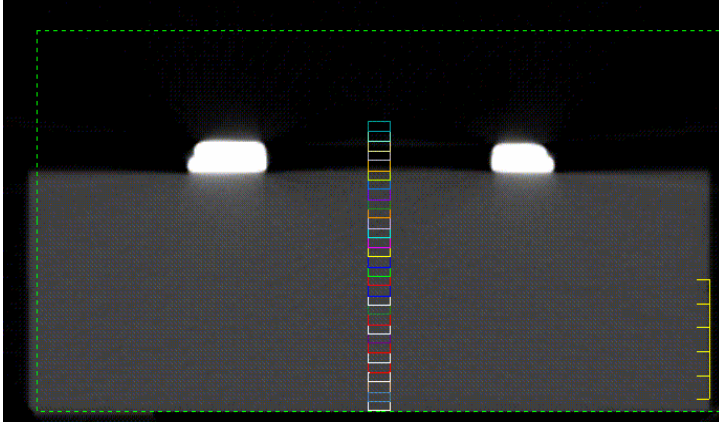
Figure 41. Central axis ROIs on MVCT image.

The mean densities were also used to obtain a radiological depth versus dose curve along the central axis. The radiological depth is defined as the sum over segments of the product of the segment length and the inhomogeneity density of the region corresponding to the segment and was calculated at each dose point by a simple equation (Siddon *et al*). The mean density of each ROI (ρ_{ROI}), the physical thickness of each ROI (Δd), and the physical depth at the center of each ROI (d_i) were used to compute the radiological depth ($d_{eq, i}$) at the center of each ROI from the following equations:

for n=1

$$d_{eq,1} = \frac{\Delta d}{2} * \rho_{ROI,1}$$

for n>1

$$d_{eq,n} = d_{eq,1} + \sum_{i=2}^{n} \frac{\Delta d}{2} * \{\rho_{ROI,i-1} + \rho_{ROI,i}\}.$$

The dose at the center of each ROI (D_i) was calculated by Pinnacle[3] and the radiological depth and dose values were used to create the plot (D_i vs. $d_{eq, i}$).

6.2.4 Dose extraction methods

Dose grids of identical dimensions were defined for all CT image sets. Then, the kVCT and MVCT image sets were registered spatially by aligning the posterior edge of the dose grid to the posterior edge of the plastic water® (Figure 42). The coordinate of the posterior edge of the plastic water® in both CT sets was determined by the same two step process outlined in Aim 2. This method put the dose grid in the same position relative to the phantom regardless of possible distortions in the anterior surface of the images due to the skin collimation.
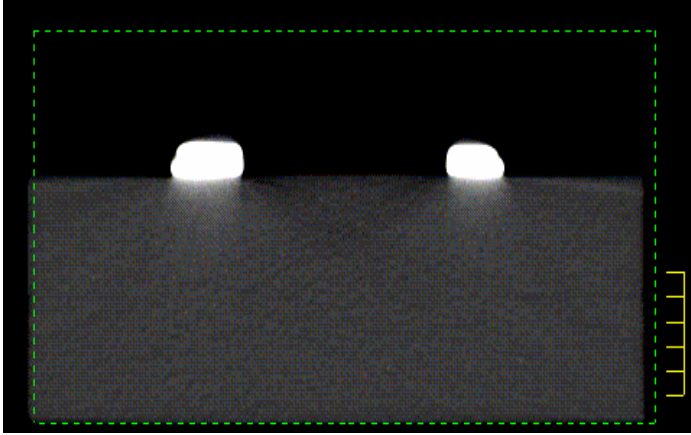
Figure 42. The dose grid (green dash) on an MVCT image with the posterior edge at the posterior edge of phantom.

After the matrices were imported into SigmaPlot® from the Pinnacle[3] workstation, the depth dose and isodose curves were aligned with respect to the back edge of the plastic water®, which corresponded to the back edge of the dose grid. This assured that the 0 cm depth for the depth dose and isodose curves corresponded to the surface of the plastic water® in the kVCT image set.

6.2.5 Treatment planning

A total of twelve treatments were planned on the nine different kVCT configurations and the nine MVCT scanned image sets. Each plan contained an electron beam at an SSD of 100cm, with a prescription of 100 monitor units and included the mask of corresponding size and thickness (Table 12).

Table 12. Treatment plans delivered to MVCT image sets.

Treatment plan	Opening size (cm^2)	Beam energy (MeV)	Mask thickness (mm)	SSD (cm)	MUs
1	3x3	6	6	100	100
2	3x3	9	6	100	100
3	3x3	12	8	100	100
4	3x3	16	10	100	100
5	6x6	6	6	100	100
6	6x6	9	6	100	100
7	6x6	12	8	100	100
8	6x6	16	10	100	100
9	10x10	6	6	100	100
10	10x10	9	6	100	100
11	10x10	12	8	100	100
12	10x10	16	10	100	100

Central-axis depth dose curves and isodose curves were compared in the central axial xz-plane. Doses were taken directly from the planning system. No normalizations were applied. Dose comparisons were evaluated using the same criteria as used in Aims 2 and 3. In the uniform-dose region, dose differences were computed and in high dose-gradient regions, distance-to-agreement (DTA) was measured. The maximum dose difference in the uniform region was calculated by subtracting the MVCT calculated dose matrix from the kVCT calculated dose matrix. The DTAs were measured on superimposed hard copies of isodose plots for each opening and energy. It is noted that there are some large discrepancies in the penumbra region just lateral to the edges of the skin collimation. This is due in part to the fact that the Pinnacle[3] pencil beam algorithm has pencil beams that are 2x2 mm^2. This means that there is a ±1 mm uncertainty in position of the calculated doses at the edge of the beam. Also, the MVCT images show some distortion at the edges of the Cerrobend® mask. They appear slightly rounded when in fact the edges are straight (Fig 43). This adds to the uncertainty in calculated dose at the edge of the collimation.
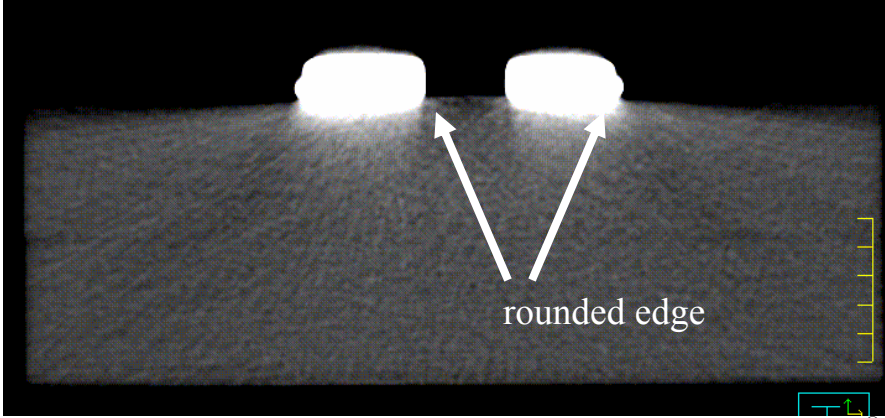
Figure 43. Axial MVCT image showing distorted (rounded) edges of Cerrobend® skin collimation (3x3 cm^2, 10 mm).

6.3 Results
6.3.1 Small opening (3x3 cm^2)

Overlays of the MVCT and kVCT isodose distributions are shown in Figs 44-47. The central axis depth doses are shown in Figs 48-51. Table 12 gives the range of dose differences in the uniform-dose region. There is no instance in which the maximum dose differences meet the hypothesis criterion. All cases fail to meet the criterion and the maximum error is largest in the 12 MeV case, which is the energy with the highest peak in dose along the central axis.

The maximum DTAs in the high dose-gradient regions are also shown in Table 13. In no instance are they within ±2 mm. For the 12 MeV and 16 MeV beams, the maximum DTAs are well above ±2 mm. In addition, the maximum DTA also increases with increasing beam energy.

Table 13. Ranges of dose differences for the 3x3 cm^2 opening in the uniform-dose region and maximum DTAs in high dose-gradient regions.

3x3cm^2 opening	Ranges of dose differences (%) (uniform-dose region)	Maximum DTA (mm) (gradient regions)
6 MeV	2.8, -6.3	3.2
9 MeV	2.7, -6.7	4.0
12 MeV	5.0, -11.8	6.3
16 MeV	5.9, -7.5	7.3

The central-axis depth doses highlight some aspects of the comparison that are not readily apparent in the maximum dose differences and maximum DTA measurements. The depth doses show a decreasing penetration of the beam in the MVCT images relative to the kVCT images as the energy increases. In addition, there is a peaking phenomenon for the MVCT calculated doses. The highest peak occurs for the 12 MeV beam and the longest peak occurs for the 16 MeV beam. This peaking is unique to the small opening case and will be discussed in the analysis section.
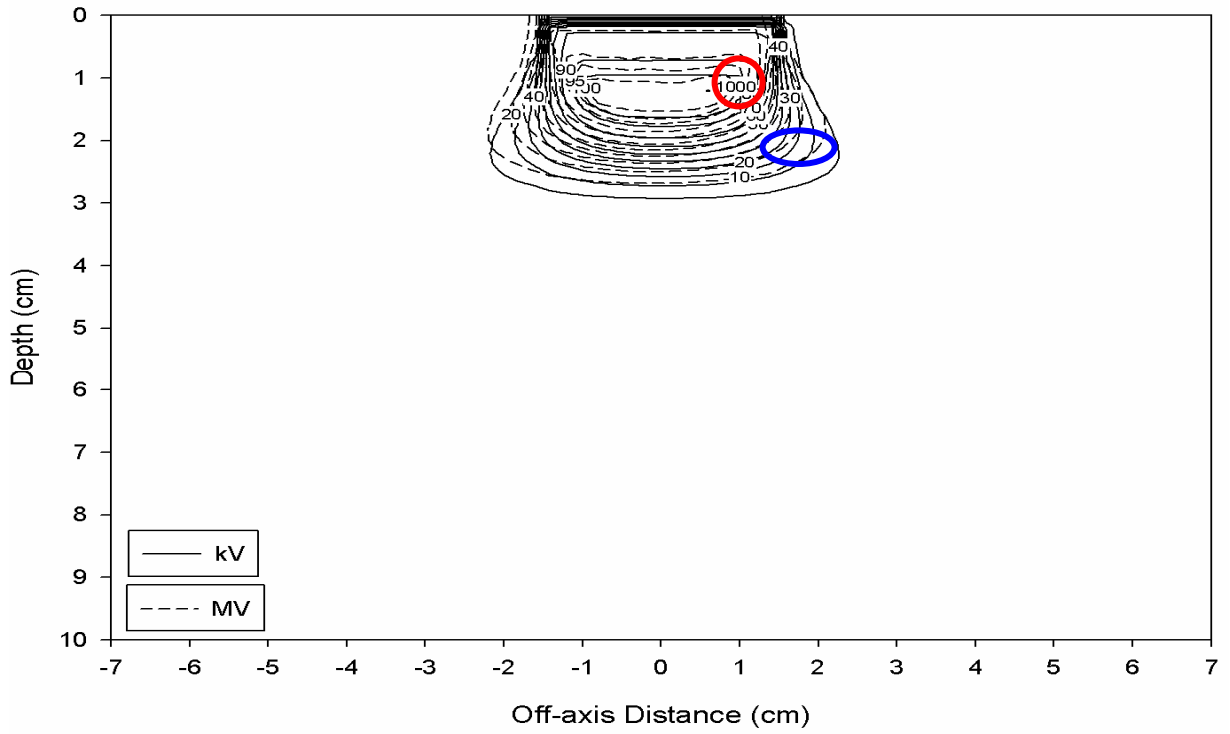
Figure 44. MVCT and kVCT calculated isodose comparison (3x3 cm^2, 6 MeV).
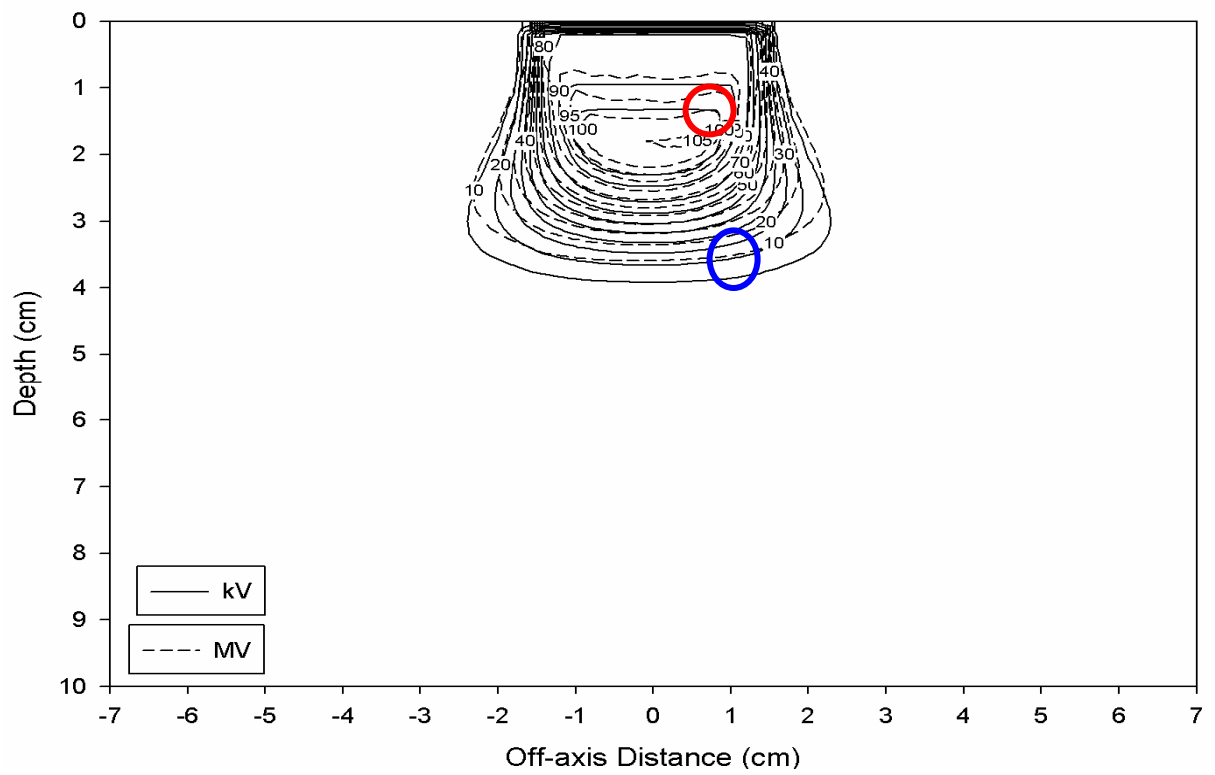
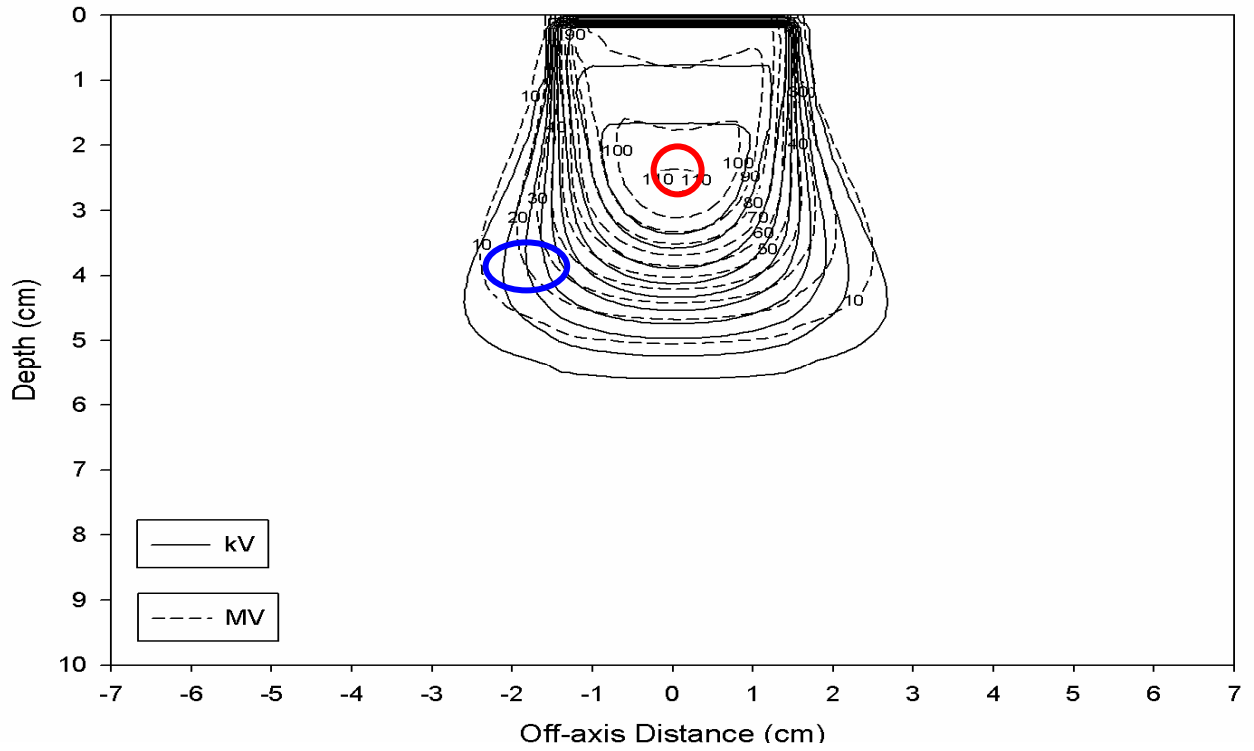Figure 45. MVCT and kVCT calculated isodose comparison (3x3 cm^2, 9 MeV).

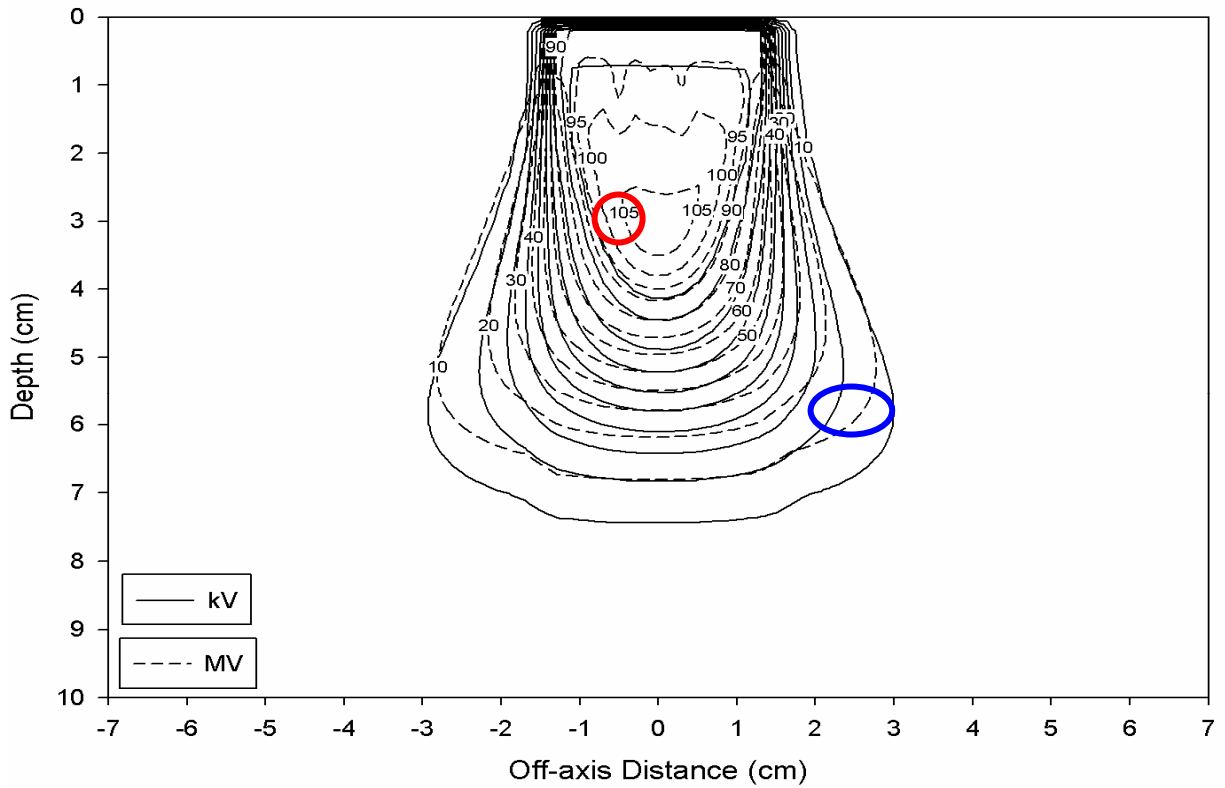Figure 46. MVCT and kVCT calculated isodose comparison (3x3 cm^2, 12 MeV).

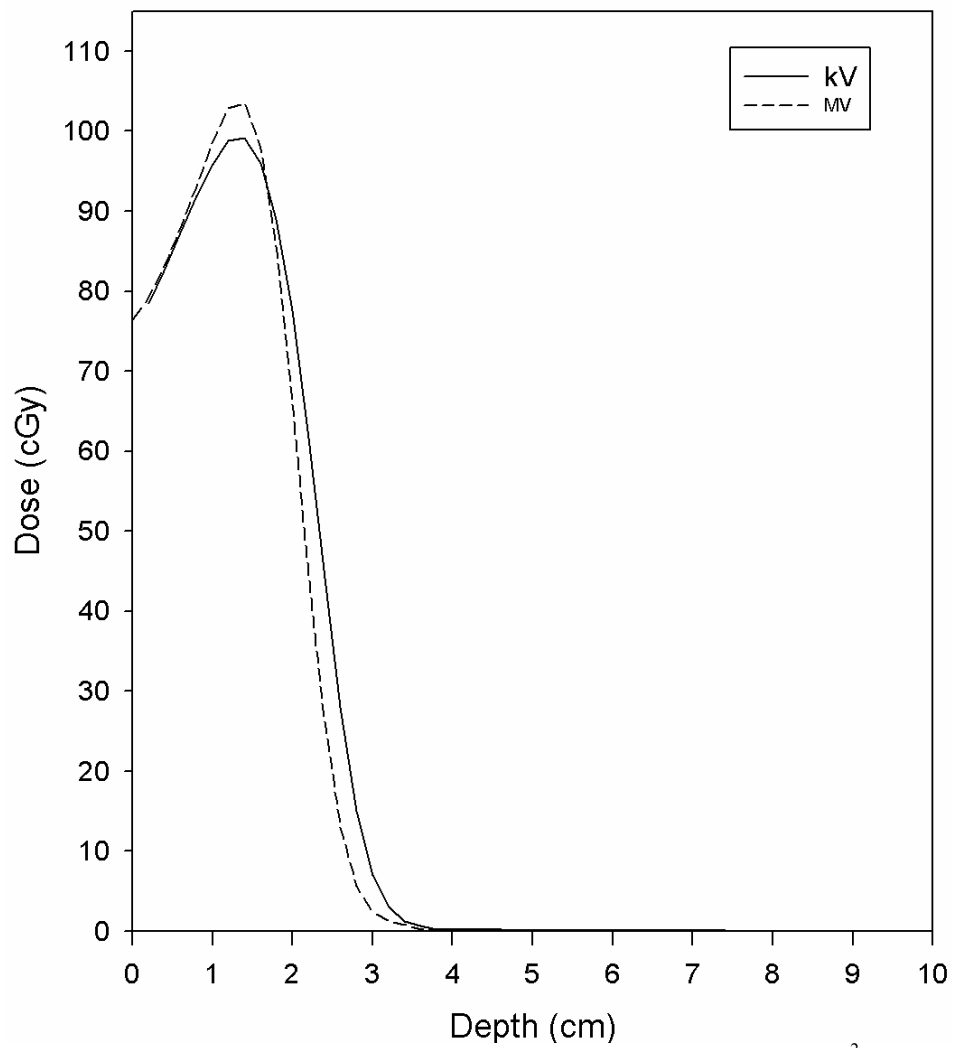Figure 47. MVCT and kVCT calculated isodose comparison (3x3 cm^2, 16 MeV).

Figure 48. MVCT and kVCT calculated depth dose curve comparison (3x3 cm^2, 6 MeV).
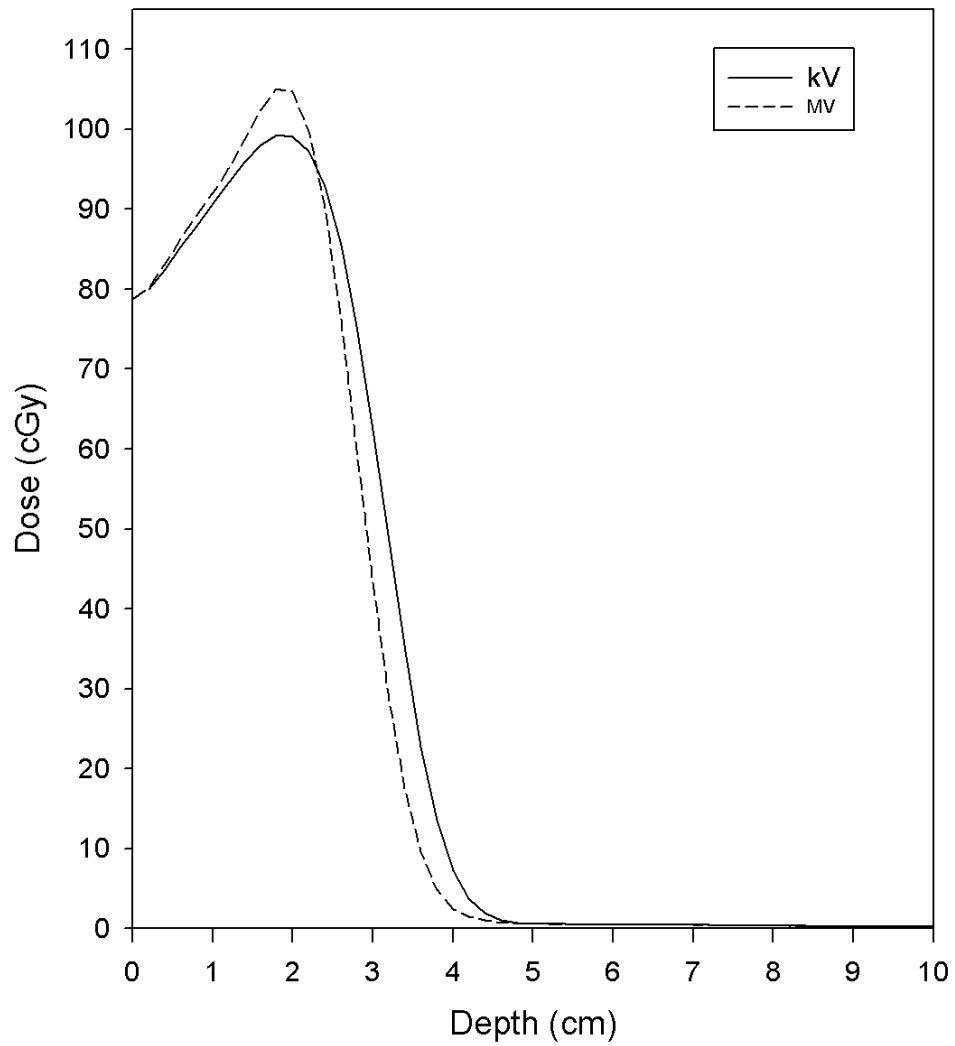
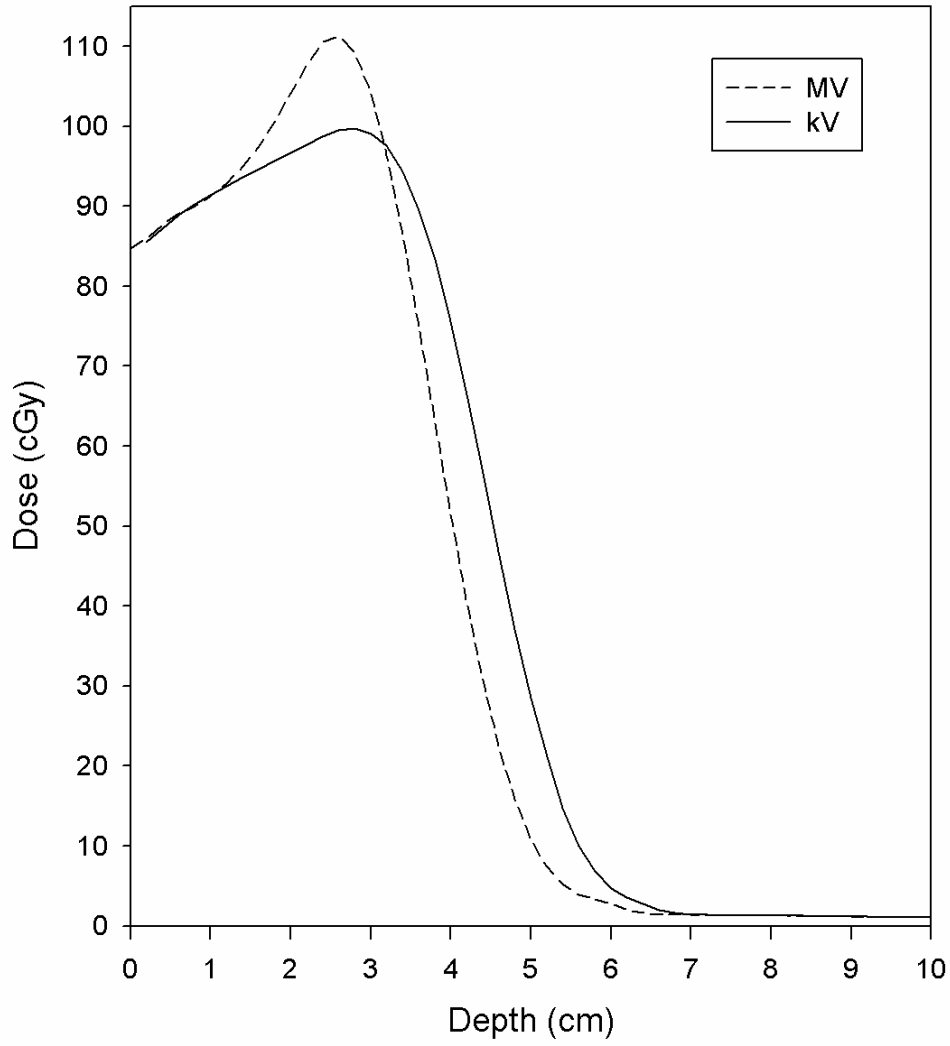Figure 49. MVCT and kVCT calculated depth dose curve comparison (3x3 cm^2, 9 MeV).

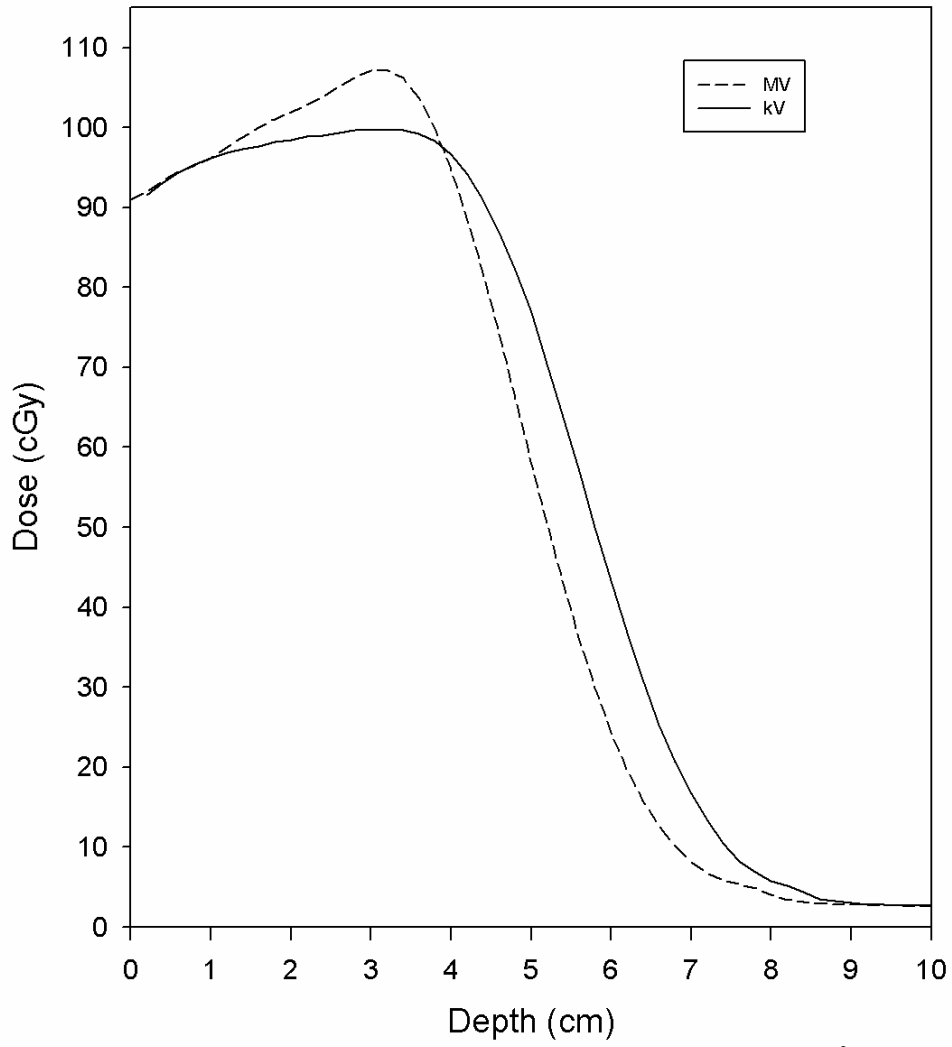Figure 50. MVCT and kVCT calculated depth dose curve comparison (3x3 cm², 12MeV).

Figure 51. MVCT and kVCT calculated depth dose curve comparison (3x3 cm^2, 16 MeV).

6.3.2 Medium opening (6x6cm^2)

   Overlays of the MVCT and kVCT isodose distributions are shown in Figs 52-55. Depth dose curves along the central axis are shown in Figs 56-59. Table 14 gives the range of dose differences in the uniform-dose region. The maximum dose differences fail to meet the hypothesis criterion (±5%) for all beams. The maximum DTAs in the high dose-gradient regions fail to be within ±2 mm for all energies (Table 14). However, the maximum DTAs clearly agree much better than those of the small opening.

Table 14. Ranges of dose differences for the 6x6cm^2 opening in the uniform-dose region and maximum DTAs in high dose-gradient regions.

6x6cm^2 opening	Ranges of dose differences (%) (uniform-dose region)	Maximum DTA (mm) (gradient regions)
6 MeV	6.3, -5.3	2.7
9 MeV	5.2, -7.6	3.0
12 MeV	5.1, -2.6	3.7
16 MeV	3.2, -13.7	3.7

   Comparison of the central-axis depth dose curves shows very good agreement in the penetration of the higher energy beams. Similar to the 3x3 cm^2 opening MVCT depth dose curves, the curves for this opening penetrate less deeply than those of the kVCT. However, in this case, the curves agree much better especially for the lower energies. There also appears to be less variation in the difference with beam energy. It should be noted that in the low energy range (6-12 MeV) there is none of the peaking that occurred for the small opening beams. A slight peak occurs in the high energy (16 MeV) beam and this will be discussed in the analysis section.
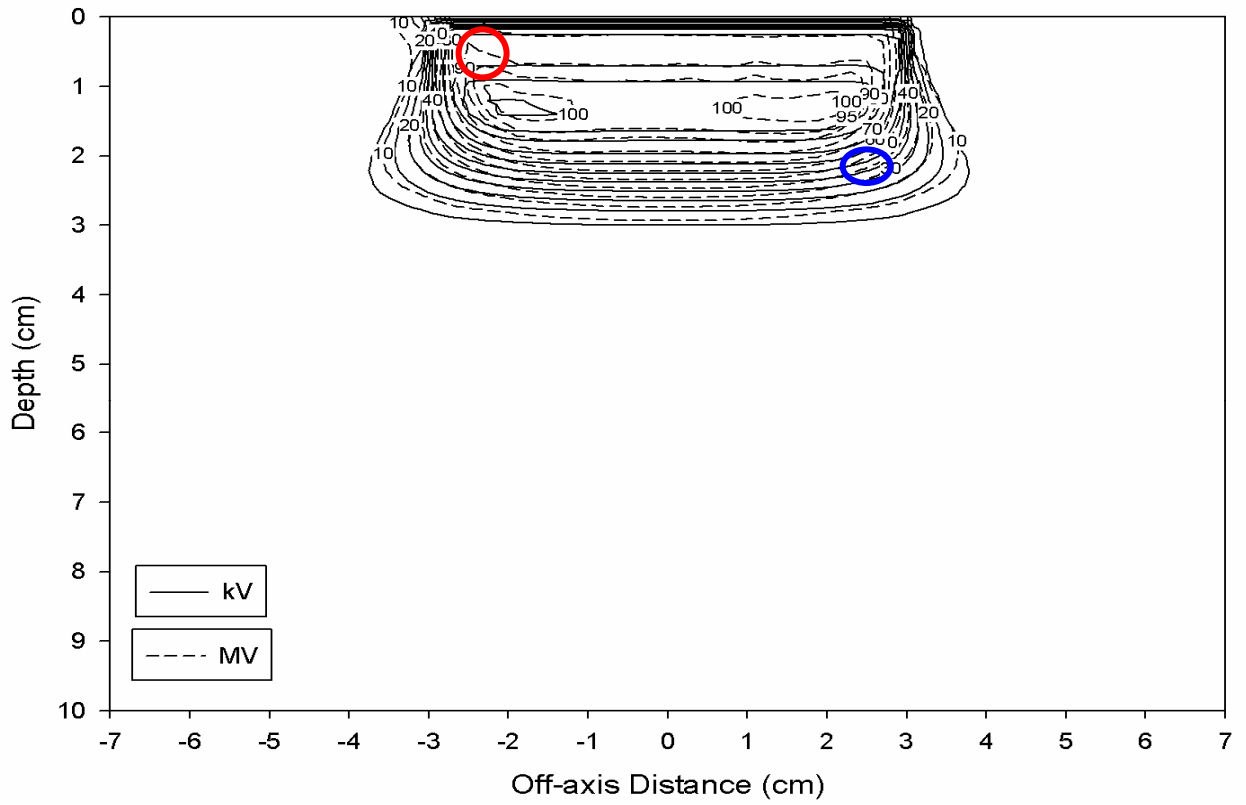
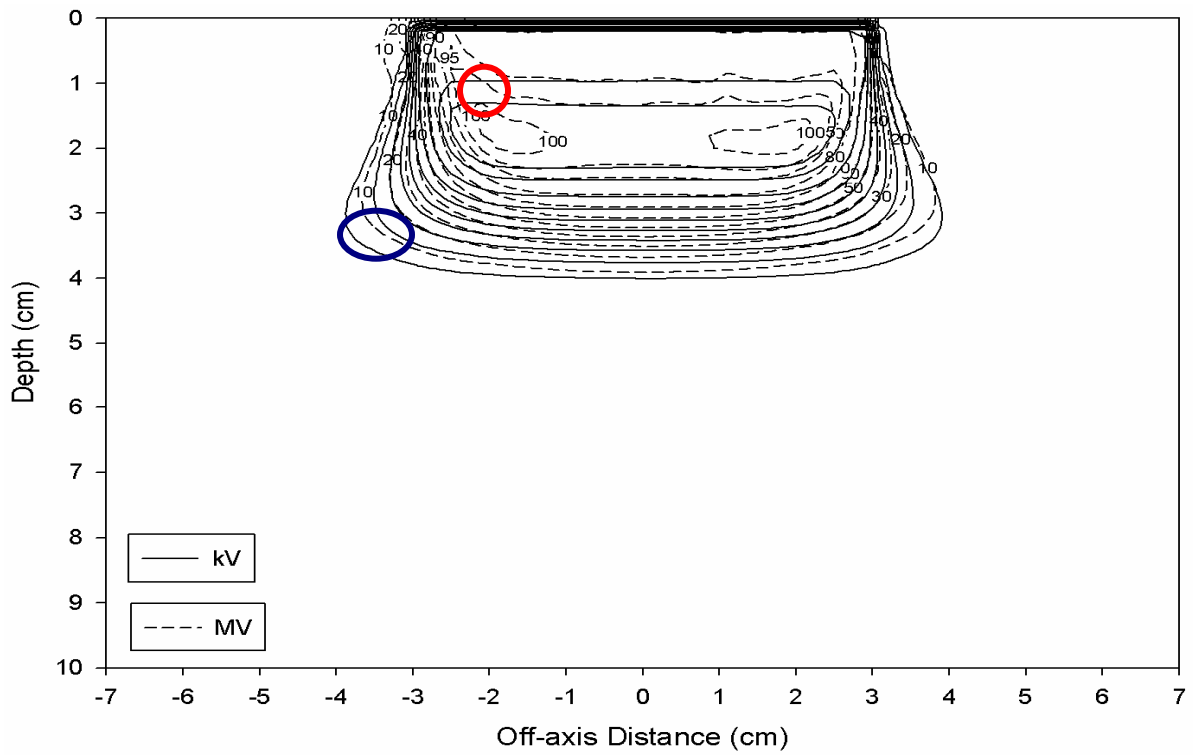Figure 52. MVCT and kVCT calculated isodose comparison (6x6 cm^2, 6 MeV).

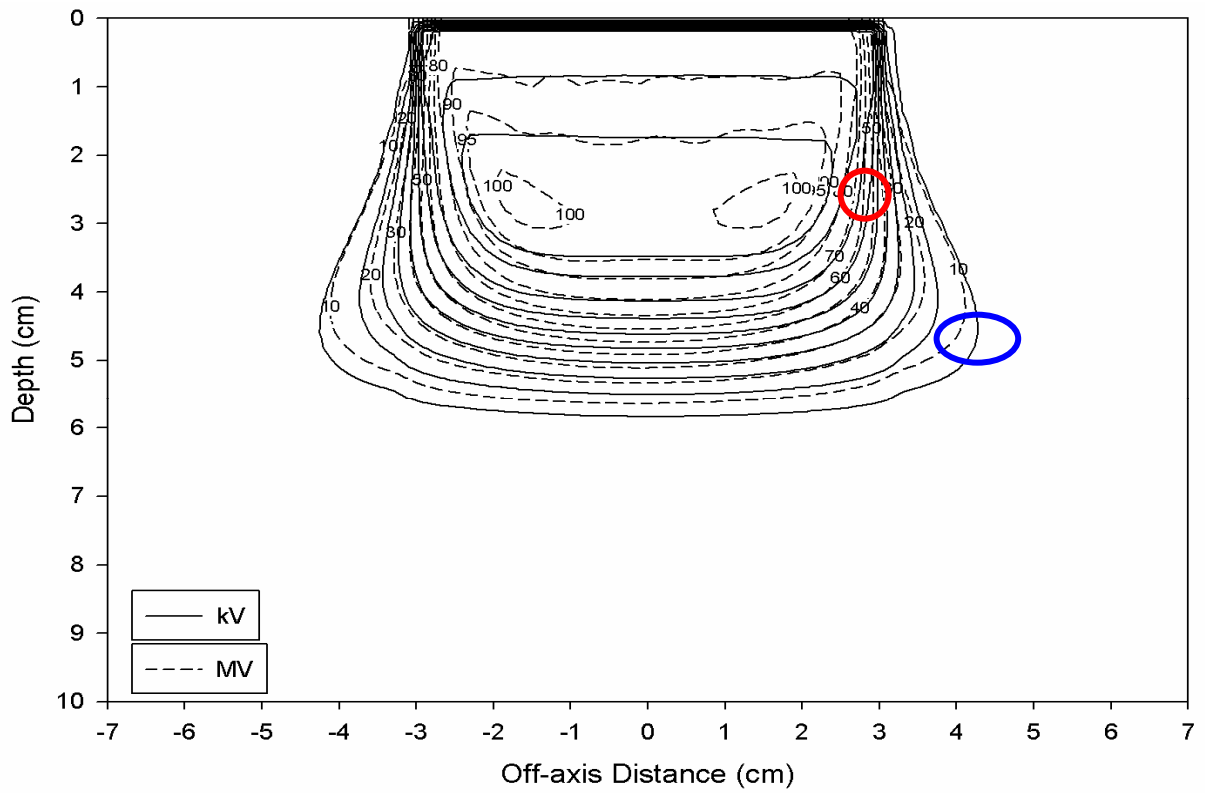Figure 53. MVCT and kVCT calculated isodose comparison (6x6 cm^2, 9 MeV).

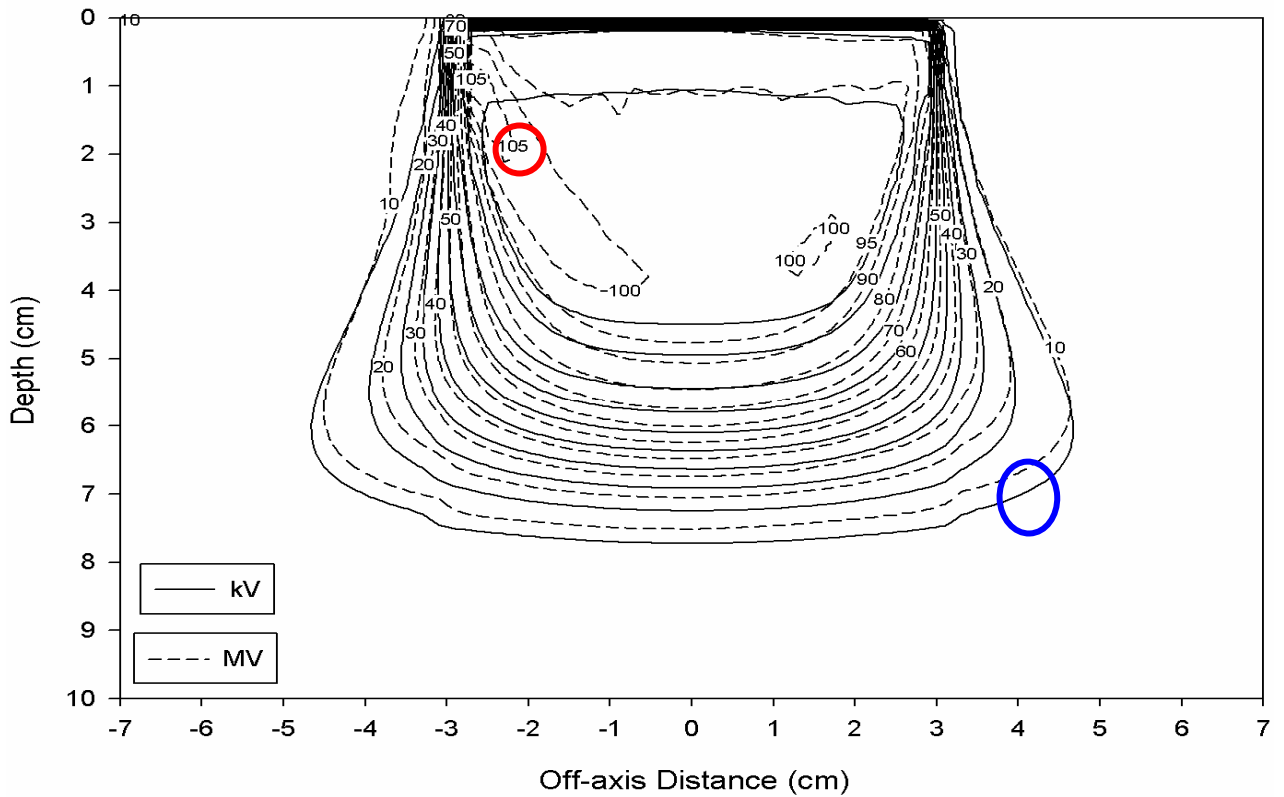Figure 54. MVCT and kVCT calculated isodose comparison (6x6 cm^2, 12 MeV).

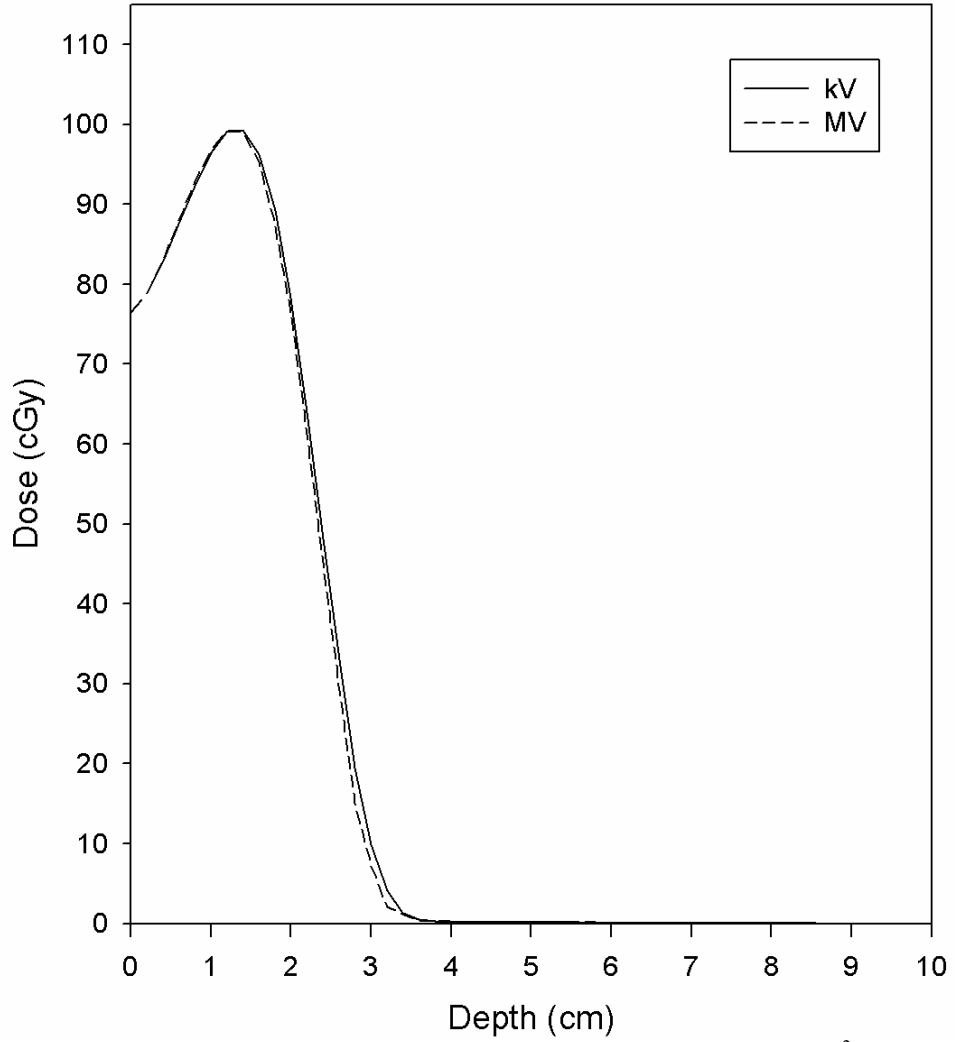Figure 55. MVCT and kVCT calculated isodose comparison (6x6 cm^2, 16 MeV).

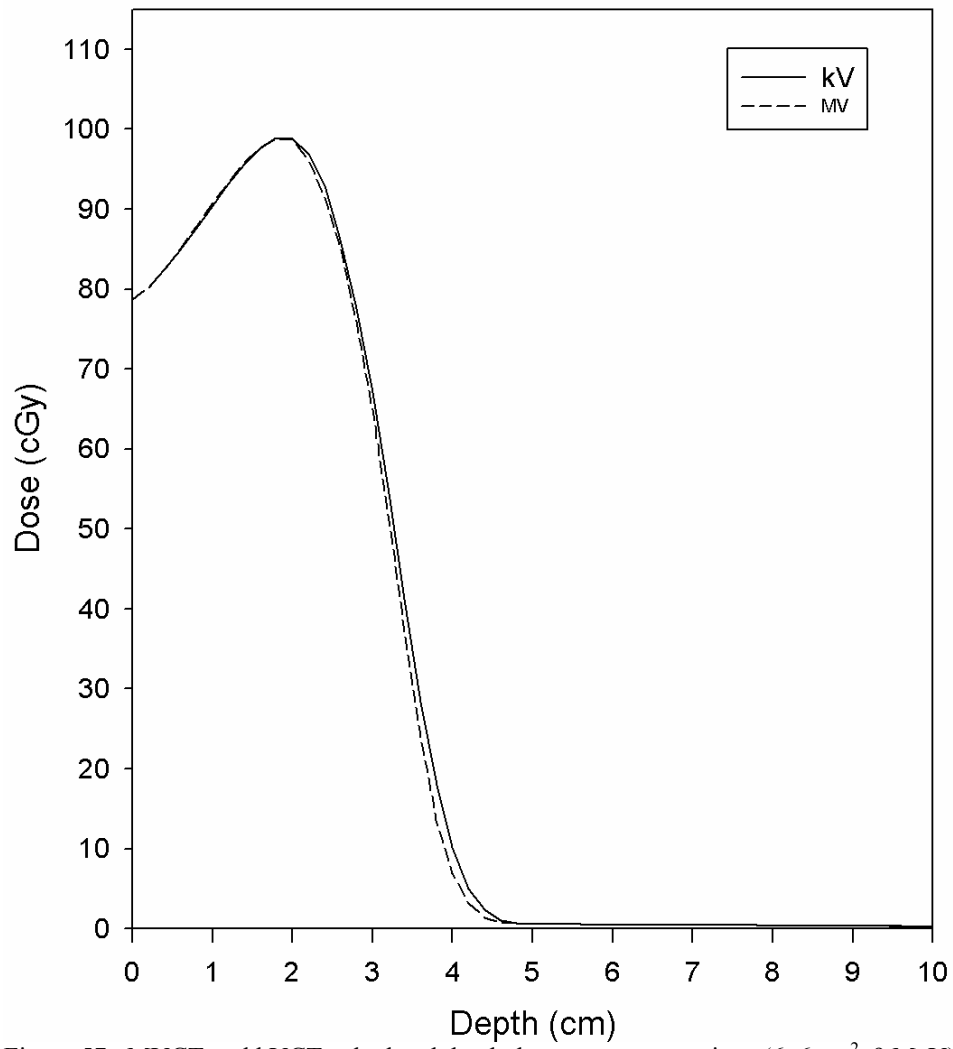Figure 56. MVCT and kVCT calculated depth dose curve comparison (6x6 cm^2, 6 MeV).

.

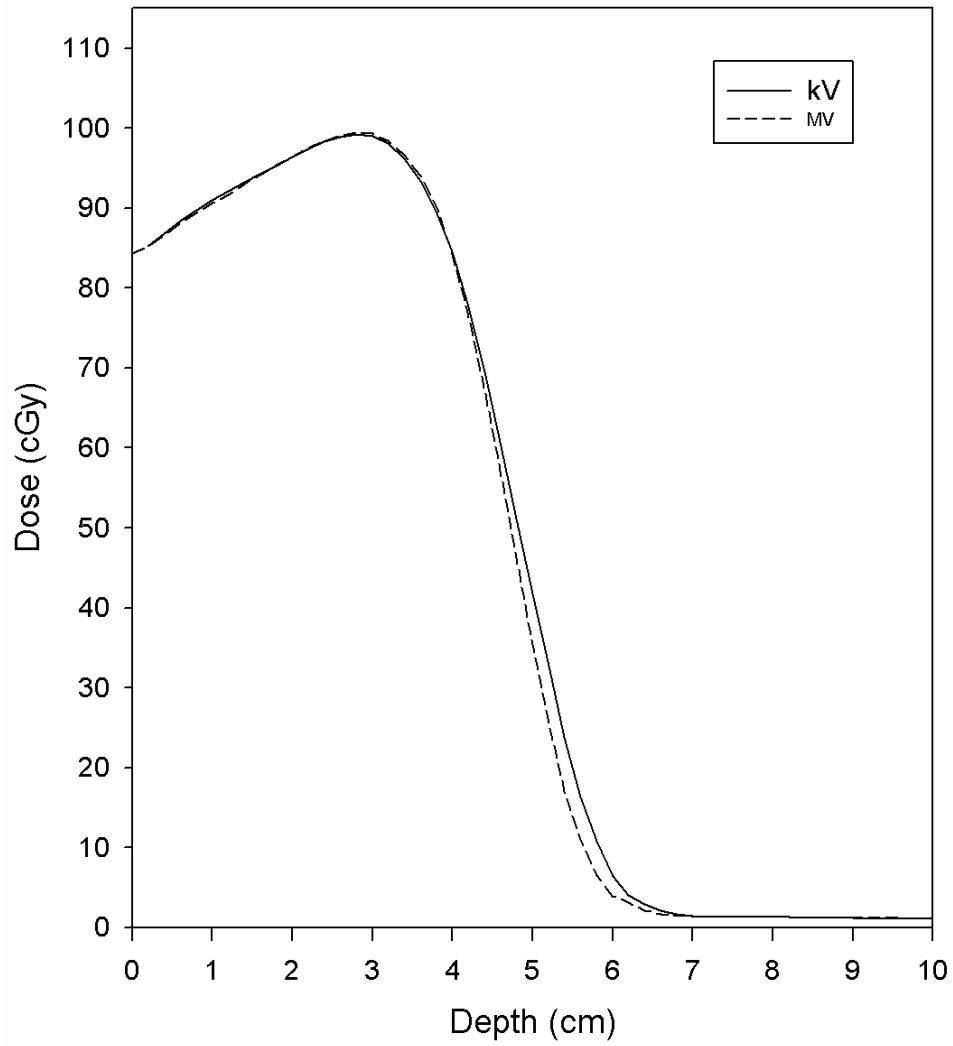Figure 57. MVCT and kVCT calculated depth dose curve comparison (6x6 cm^2, 9 MeV).

Figure 58. MVCT and kVCT calculated depth dose curve comparison (6x6 cm^2, 12 MeV).
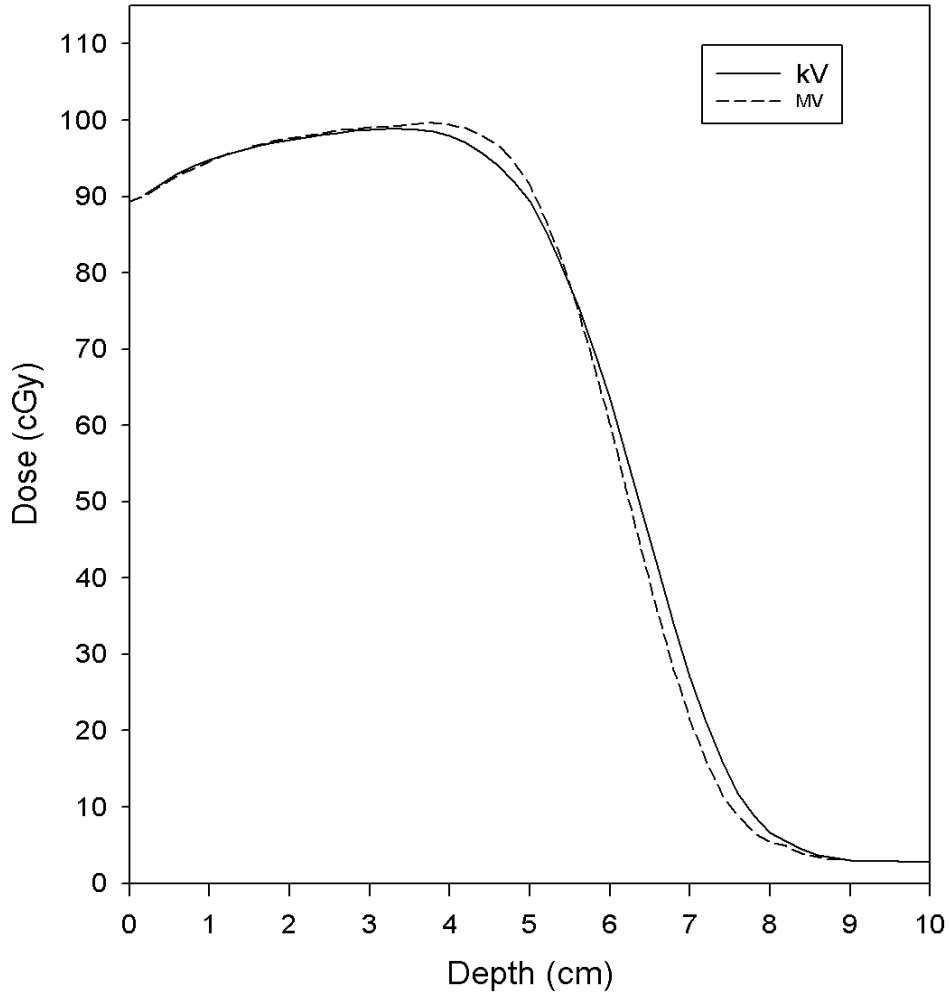
Figure 59. MVCT and kVCT calculated depth dose curve comparison (6x6 cm^2, 16 MeV).

6.3.3 Large opening (10x10cm^2)

Overlays of the MVCT and kVCT isodose distributions are shown in Figs 60-63). Depth dose curves along the central axis are shown in Figs 64-67. Table 15 gives the range of dose differences in the uniform-dose region. In all cases, the maximum dose differences exceeded ±5%. The maximum dose differences appear to be essentially independent of beam energy.

The maximum DTA was greater than ±2 mm for all energies except 16MeV (Table 15). However, the low energies (6, 9MeV) were close to meeting the hypothesis criterion.

Table 15. Ranges of dose differences for the 10x10 cm^2 opening in the uniform-dose region and maximum DTAs in high dose-gradient regions.

10x10cm^2 opening	Ranges of dose differences (%) (uniform-dose region)	Maximum DTA (mm) (gradient regions)
6 MeV	4.8, -5.4	2.0
9 MeV	3.9, -5.5	2.0
12 MeV	4.5, -1.1	2.3
16 MeV	4.9, -2.8	1.7

Figure 60. MVCT and kVCT calculated isodose comparison (10x10 cm^2, 6 MeV).

Figure 61. MVCT and kVCT calculated isodose comparison (10x10 cm^2, 9 MeV).
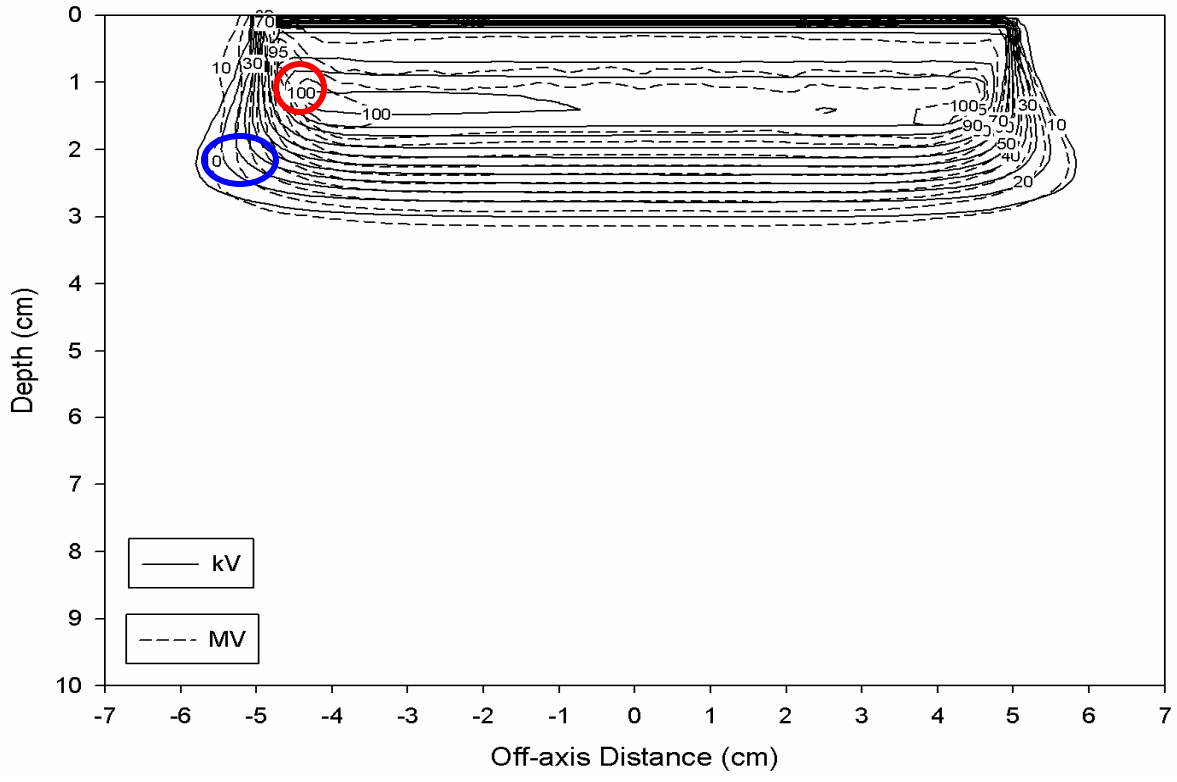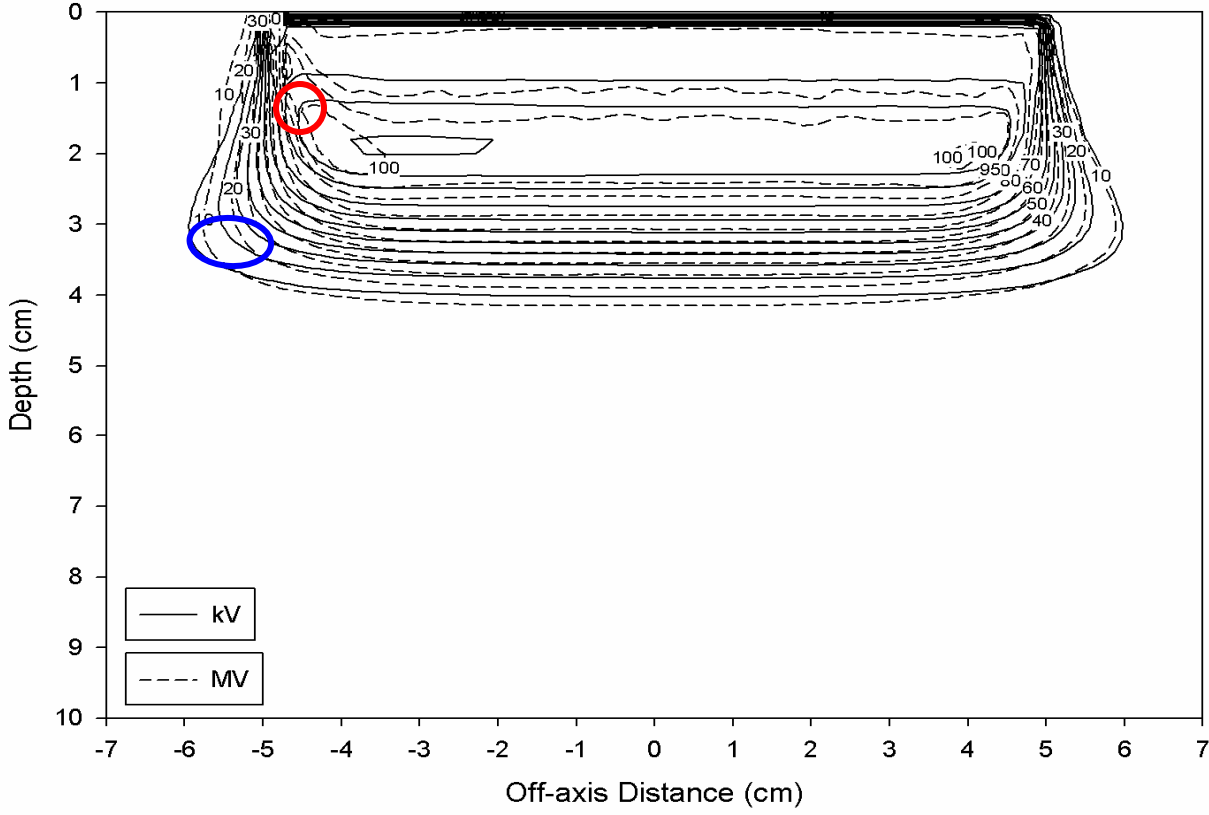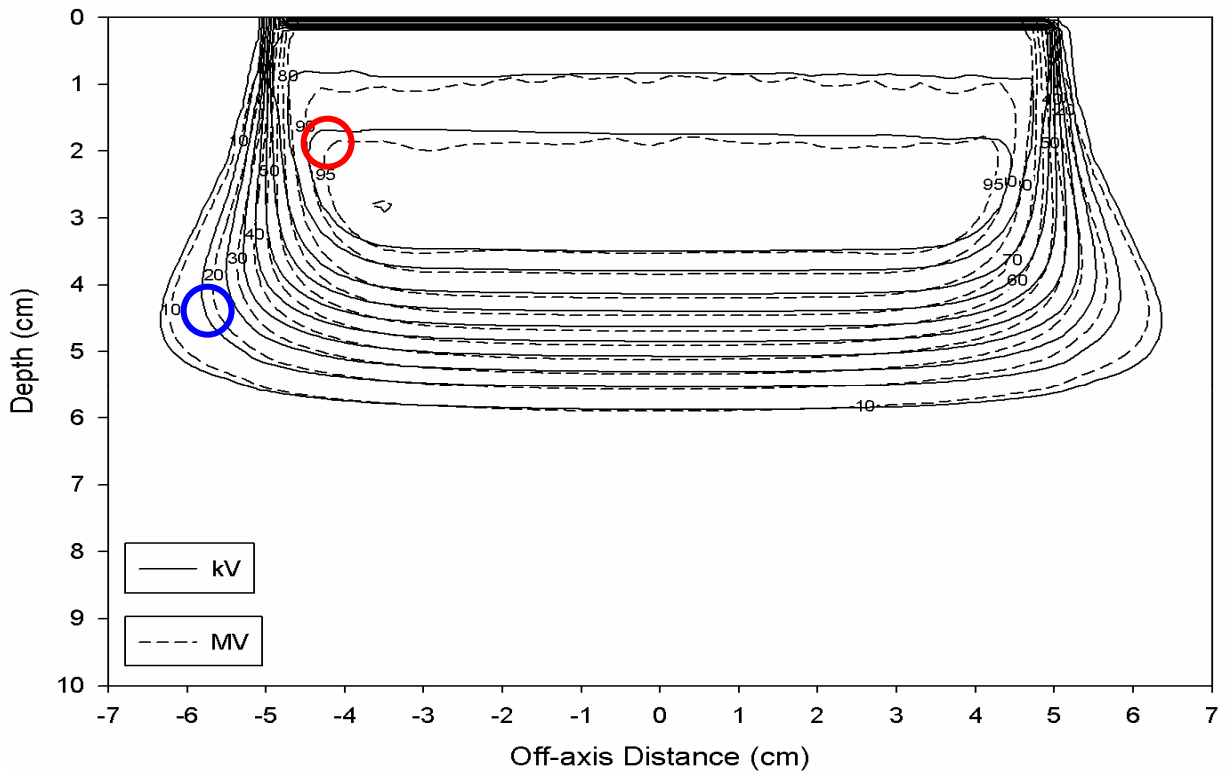
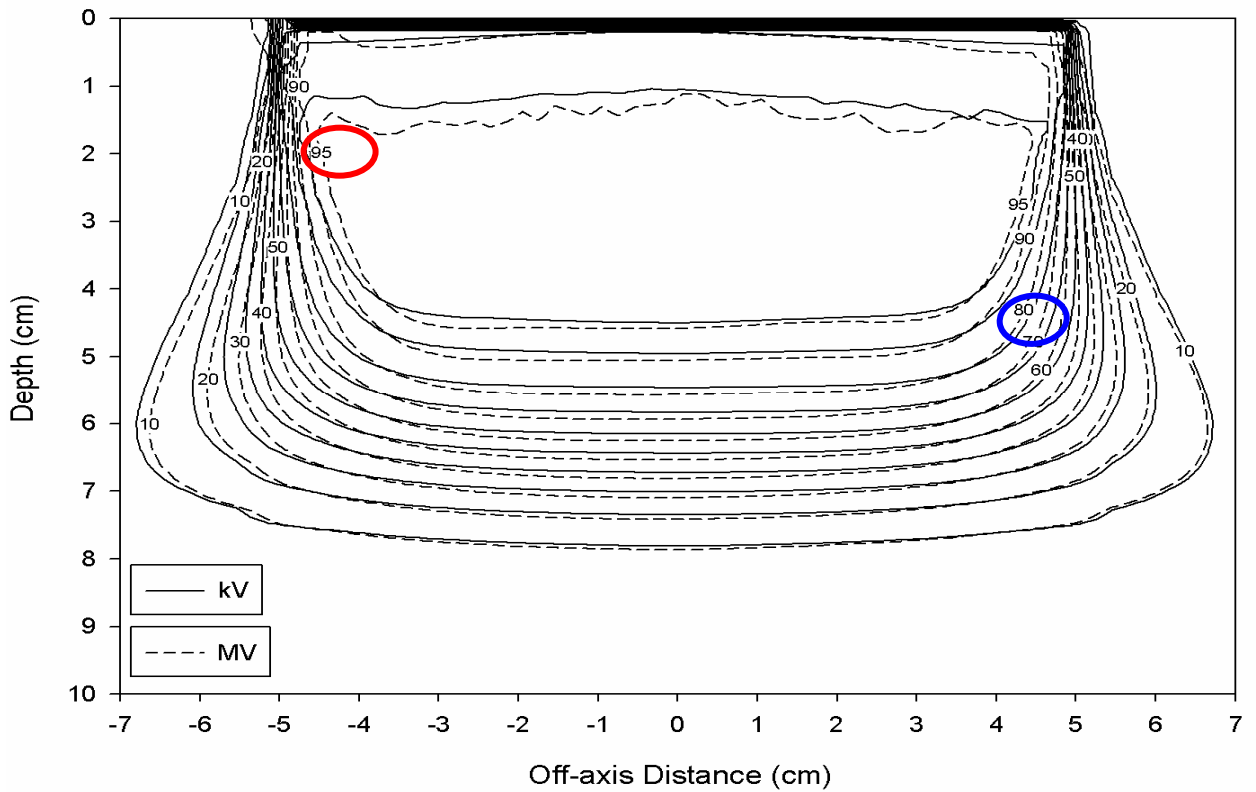Figure 62. MVCT and kVCT calculated isodose comparison (10x10 cm^2, 12 MeV).

Figure 63. MVCT and kVCT calculated isodose comparison (10x10 cm^2, 16 MeV).

The shapes of the MVCT and kVCT central-axis depth dose curves (Figs 64-67) are very similar but the MVCT curves are shifted to greater depth. The amount of shift appears to be essentially independent of beam energy. In addition, there is no peaking in the MVCT calculated dose as was seen for the small opening beams.
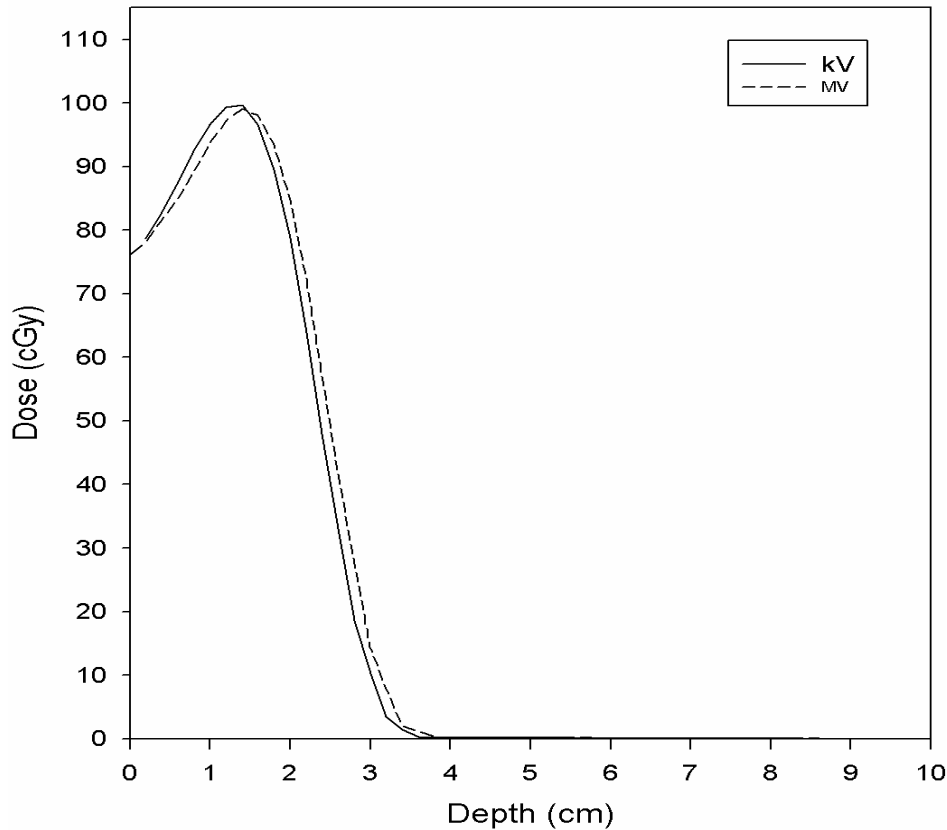

Figure 64. MVCT and kVCT calculated depth dose curve comparison (10x10 cm^2, 6 MeV).

6.3.4 Density versus depth plots

In Figures 68-70, the mean density in ROIs along the central axis is shown as a function of depth for the different mask openings and thicknesses. For comparison, the mean density in ROIs along the central axis as a function of depth is shown for the kVCT image without skin collimation.

For the small opening, mean densities along the central axis are much higher than the corresponding kVCT densities reaching a maximum increase of about 10% over kVCT values for the 10 mm mask. The MVCT densities show a slight trend toward increasing values with increasing mask thickness.

For the medium opening central axis densities are slightly higher in the MVCT images compared to the kVCT images. The maximum density for the MVCT images is only approximately 3% higher than the kVCT values. There is little variation in density with mask thickness except at the most superficial depths (0-2 cm).

For the large opening, the mean MVCT densities are slightly lower than the kVCT densities at the superficial depths (0-3.5 cm). At 1-3 cm depth, they are as much as 3% low. In that depth range, there is some variation in density with mask thickness. At greater depths (>6cm), the MVCT densities are slightly greater than the kVCT densities, but too deep to affect electron doses.

It is interesting that the density versus depth curves seem to have two plateaus. Up to about 4 cm depth, the MVCT densities show a larger variation with opening size than at greater depths. This suggests that the skin collimation produces greater distortions at shallower depths, not a surprising result.
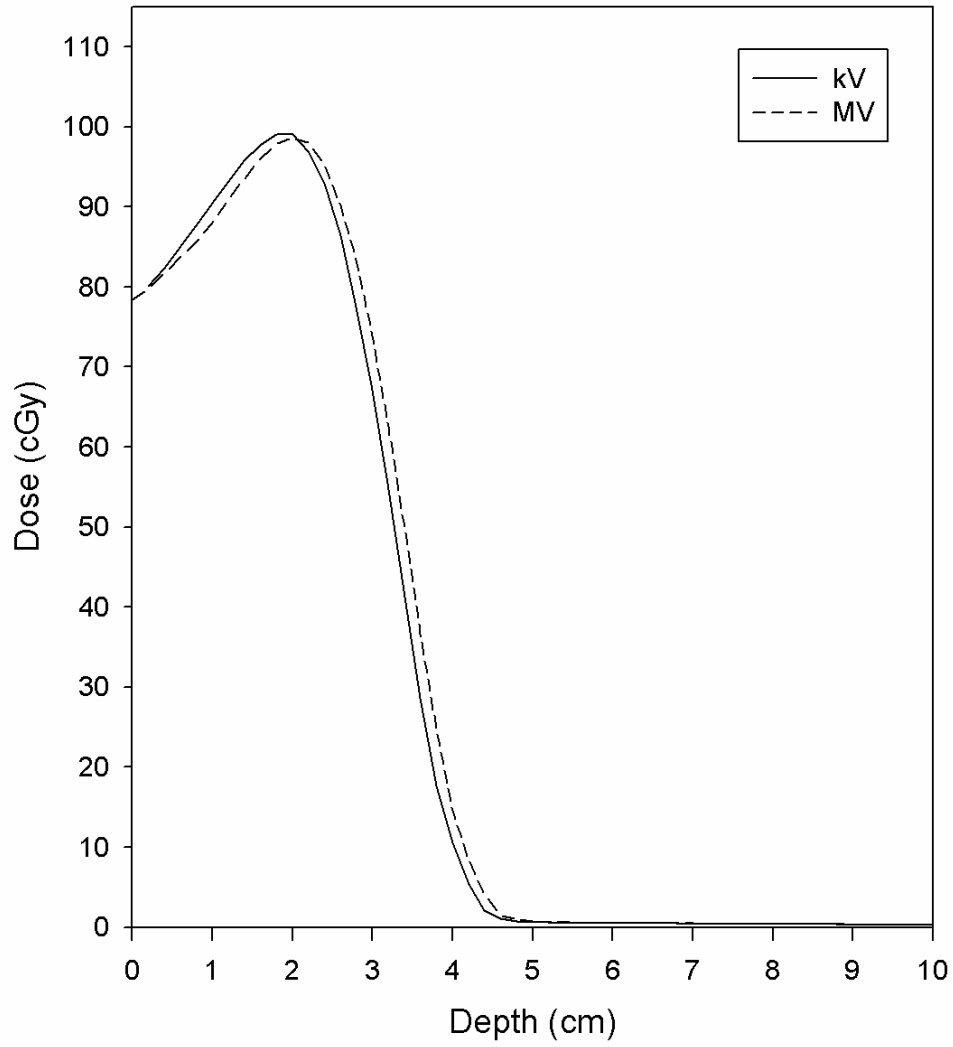
Figure 65. MVCT and kVCT calculated depth dose curve comparison (10x10 cm^2, 9 MeV).
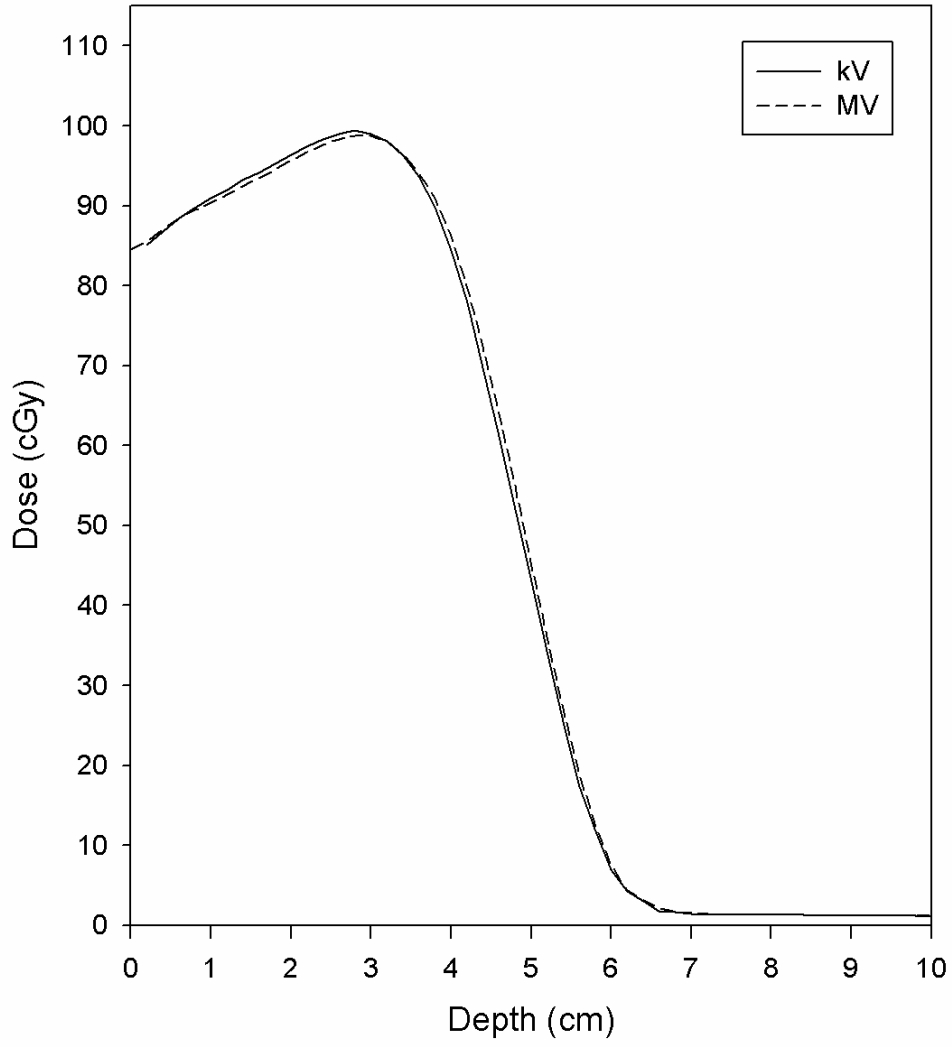
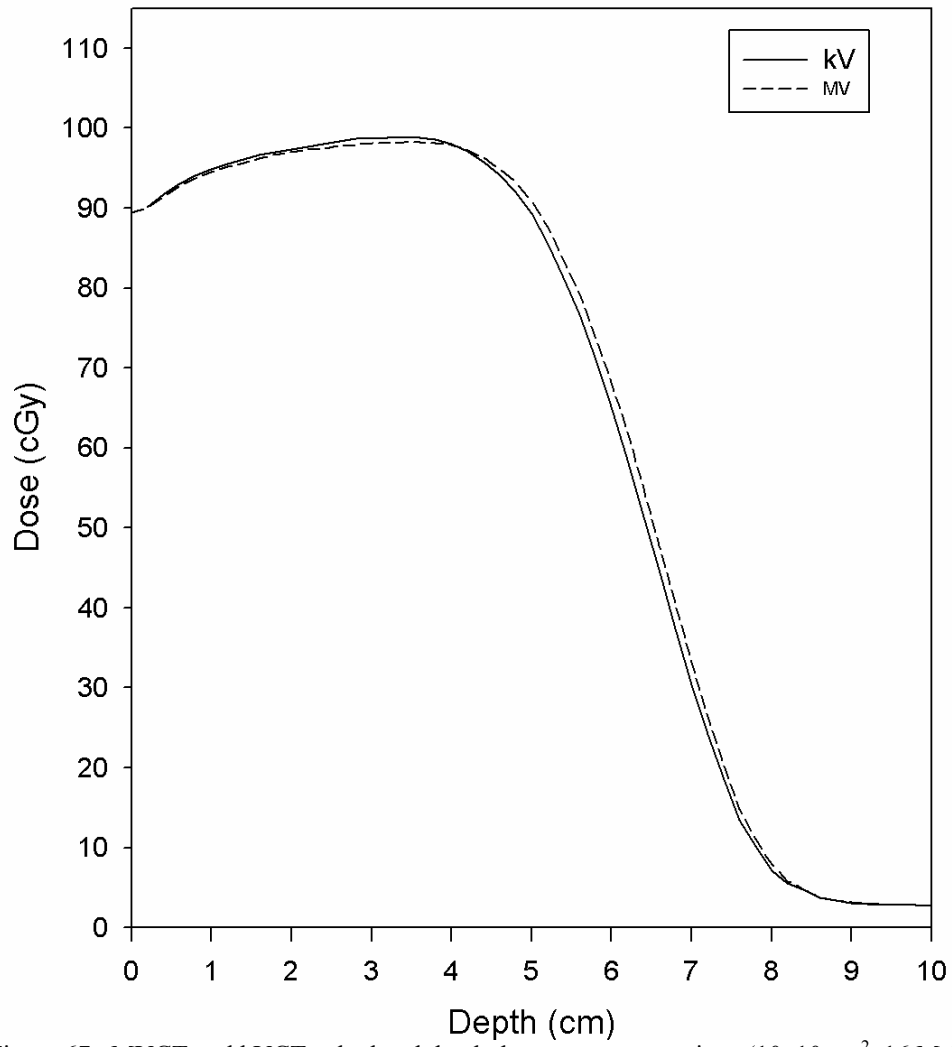Figure 66. MVCT and kVCT calculated depth dose curve comparison (10x10 cm^2, 12 MeV).

Figure 67. MVCT and kVCT calculated depth dose curve comparison (10x10 cm^2, 16 MeV).
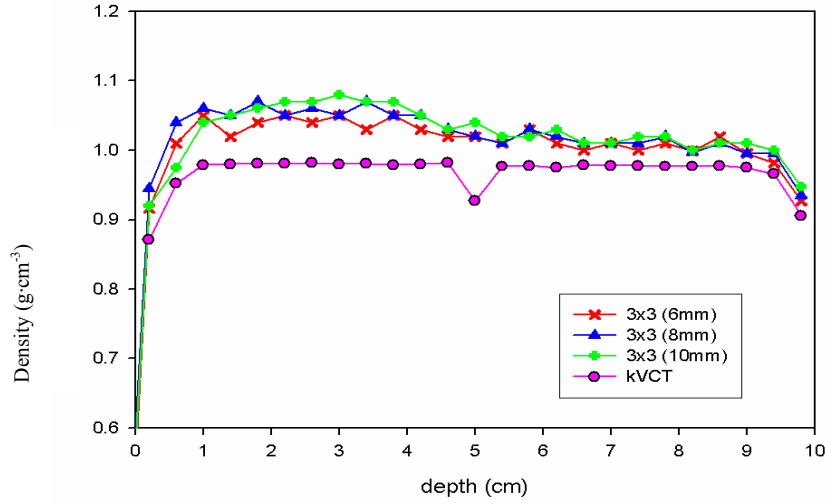
Figure 68. Density versus depth curve for the 3x3 cm^2 opening.
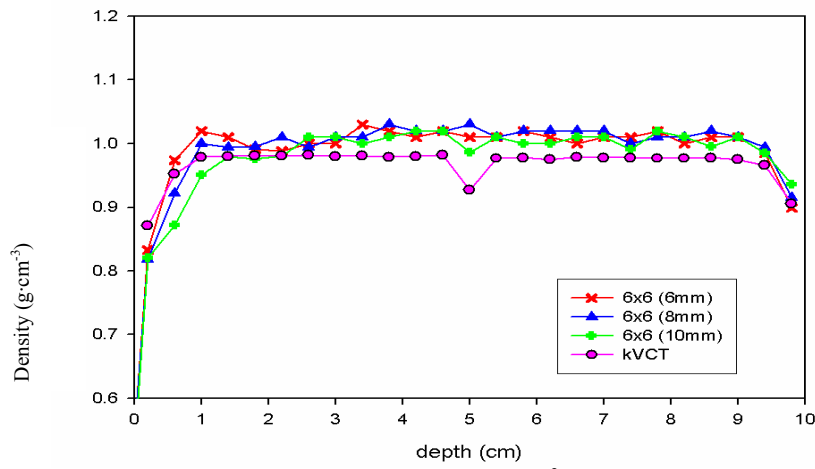

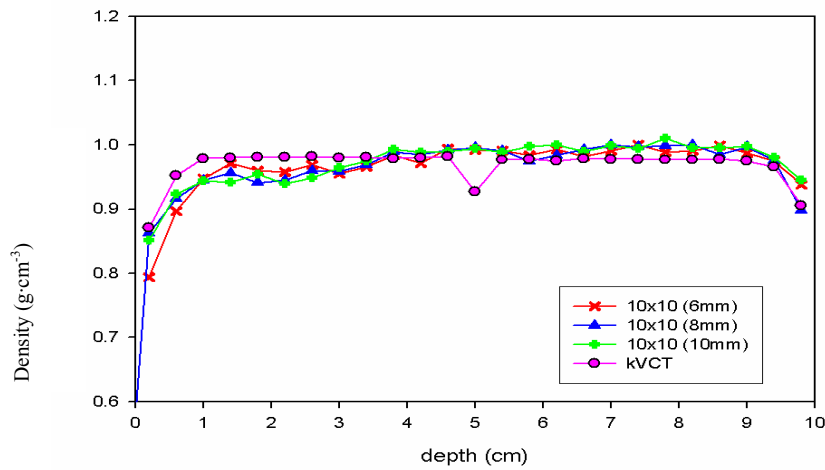Figure 69. Density versus depth curve 6x6 cm^2 opening.

Figure 70. Density versus depth curve 10x10 cm^2 opening.

6.3.5 Dose versus radiological depth

To more directly examine the effects of density distortion on calculated dose, dose was plotted as a function of radiological depth along the central-axis of each beam (Fig 71-82). Radiological depth was computed from mean densities as described in the Methods and Material.

6.4 Analysis of results

With one exception, dose calculations in the MVCT images differed from the kVCT dose calculations by more than ±5% in the uniform-dose region for all opening sizes. Agreement in the gradient regions was better but still exceeded a distance-to-agreement of ±2 mm in 9 of the 12 plans. The large opening showed the best agreement in the gradient regions.

In examining the depth dose curves for each of the opening sizes, it is clear that the shift of the MVCT curve relative to the kVCT curve varies with the size of the opening. For the small opening, the MVCT curves are greatly shifted to shallow depths. For the medium opening, the MVCT curves are shifted to more shallow depths but more closely match the kVCT curves. For the large opening, the MVCT curves are shifted to greater depths. A peak was also observed in the small opening results as well as a small peak in the high energy (16 MeV) case for the medium opening. These are two separate issues and will be discussed separately.

Figure 71. Dose versus radiological depth (3x3 cm^2 opening, 6 MeV).

Figure 72. Dose versus radiological depth (3x3 cm^2 opening, 9 MeV).
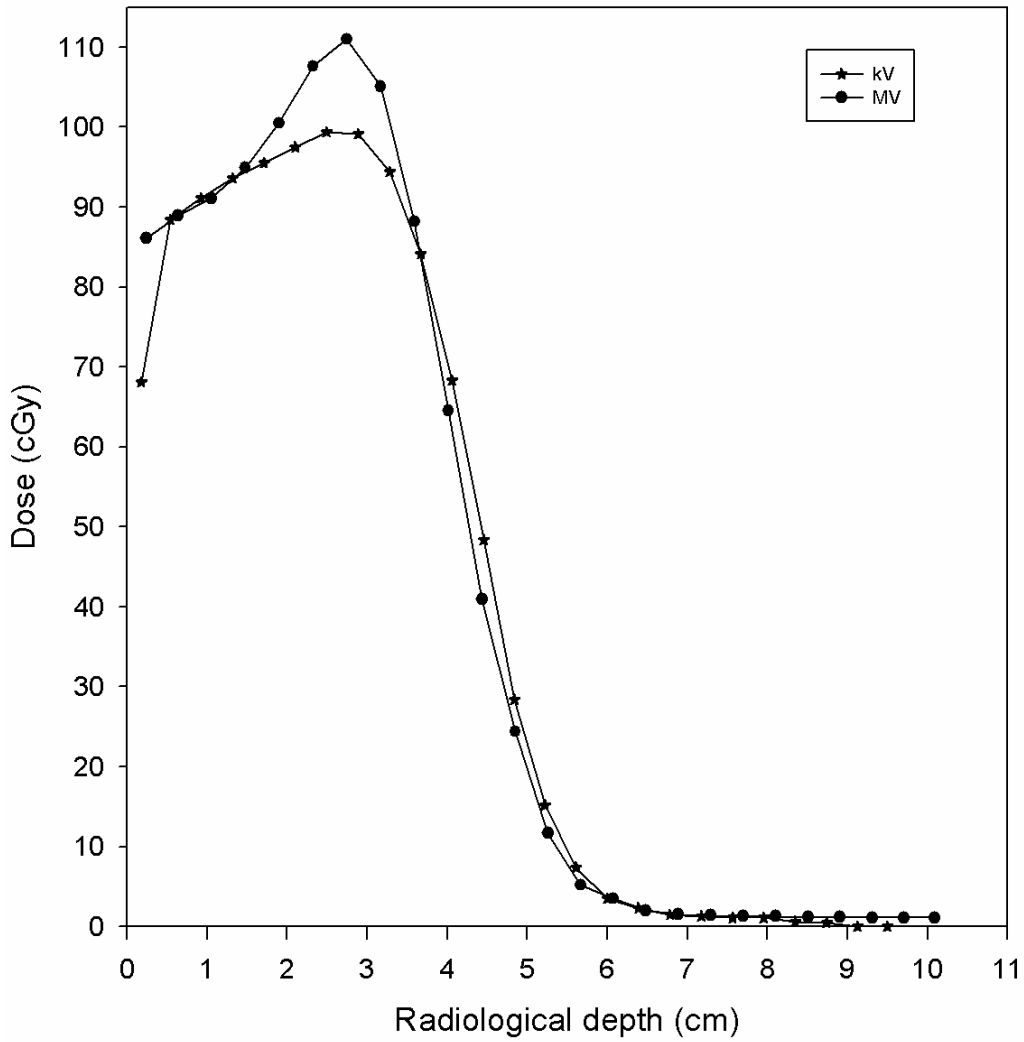
Figure 73. Dose versus radiological depth (3x3 cm^2 opening, 12 MeV).
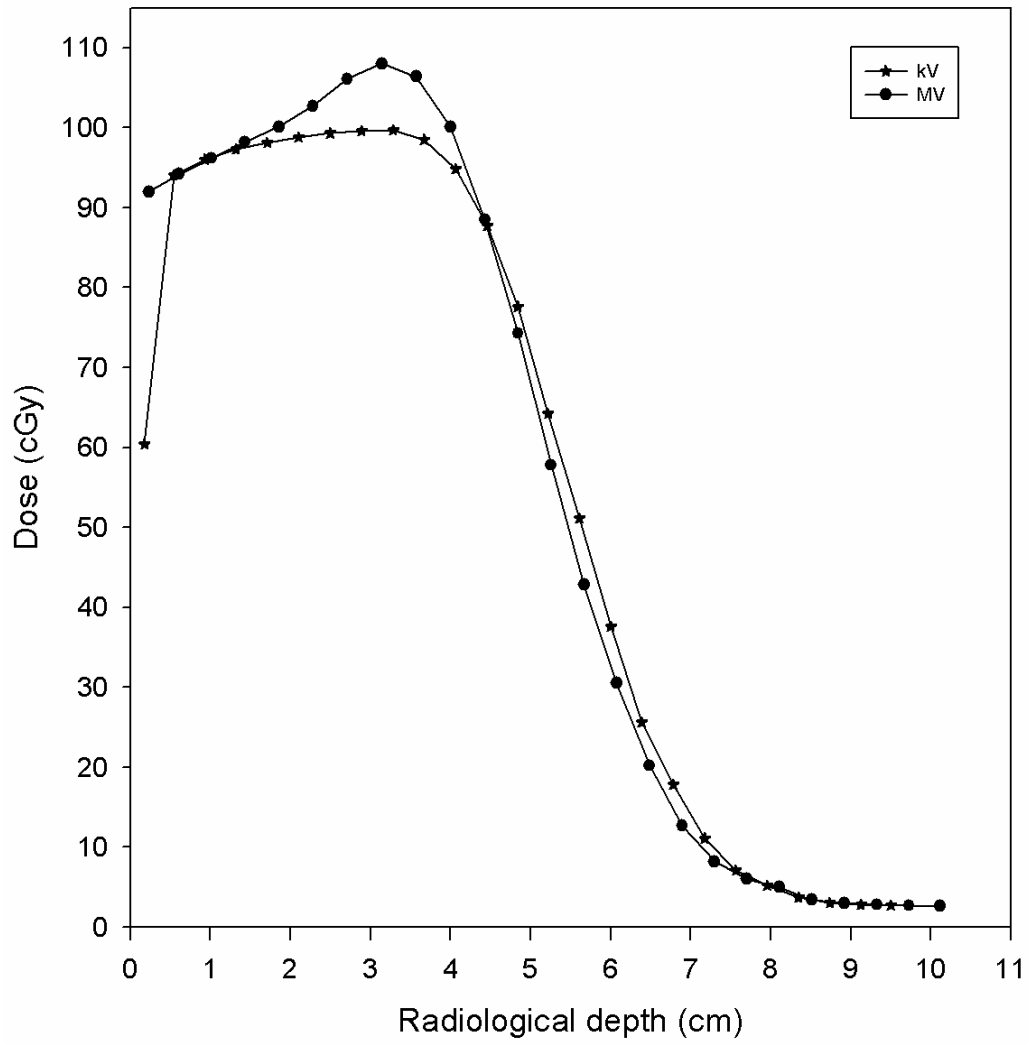
Figure 74. Dose versus radiological depth (3x3 cm^2 opening, 16 MeV).
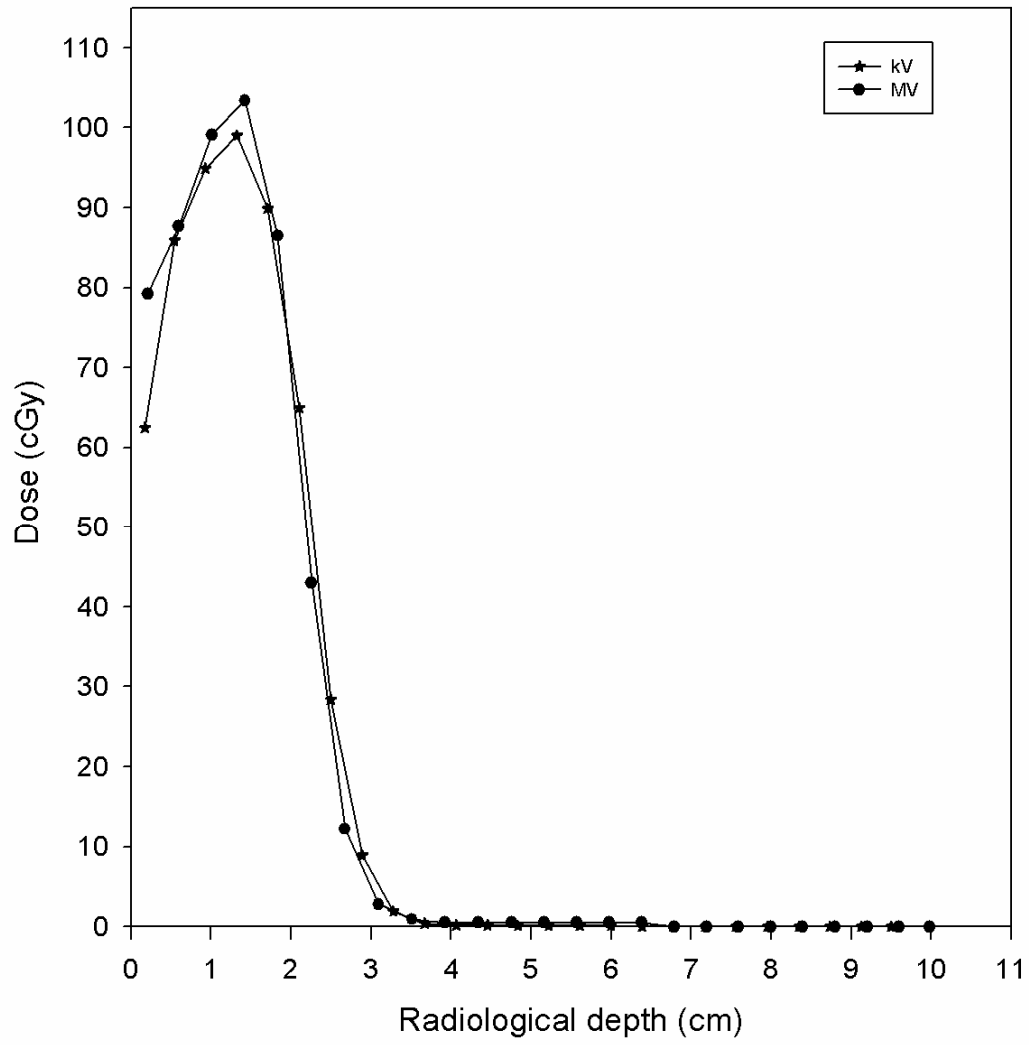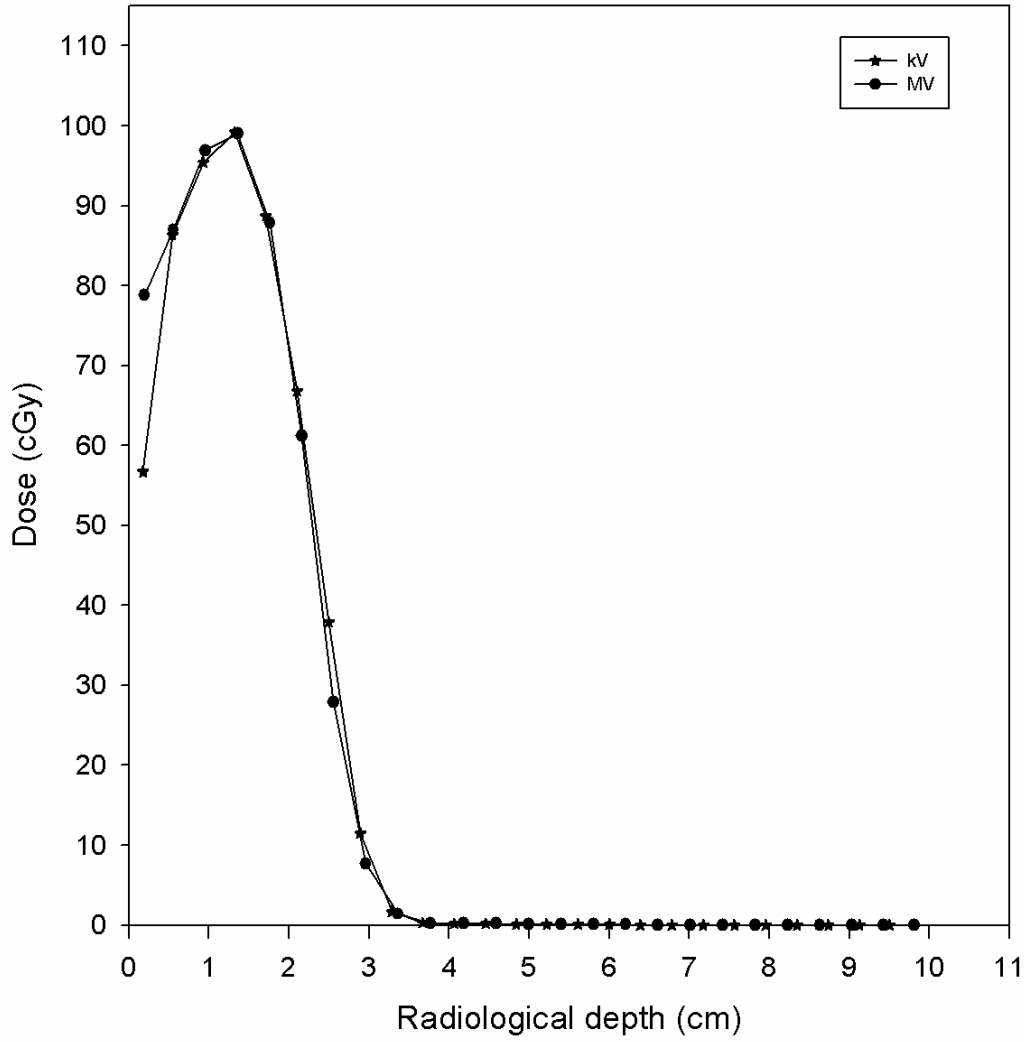
Figure 75. Dose versus radiological depth (6x6 cm^2 opening, 6 MeV).
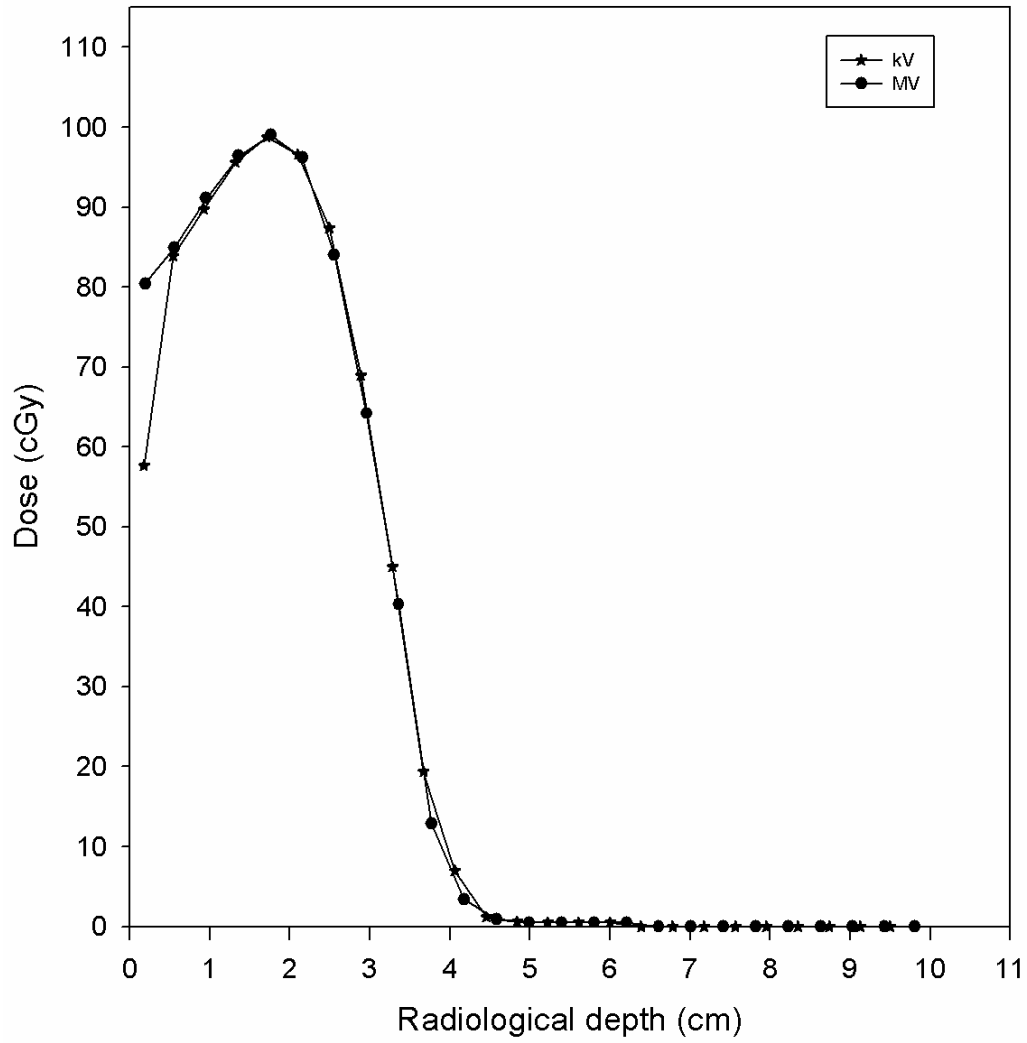
Figure 76. Dose versus radiological depth (6x6 cm^2 opening, 9 MeV).
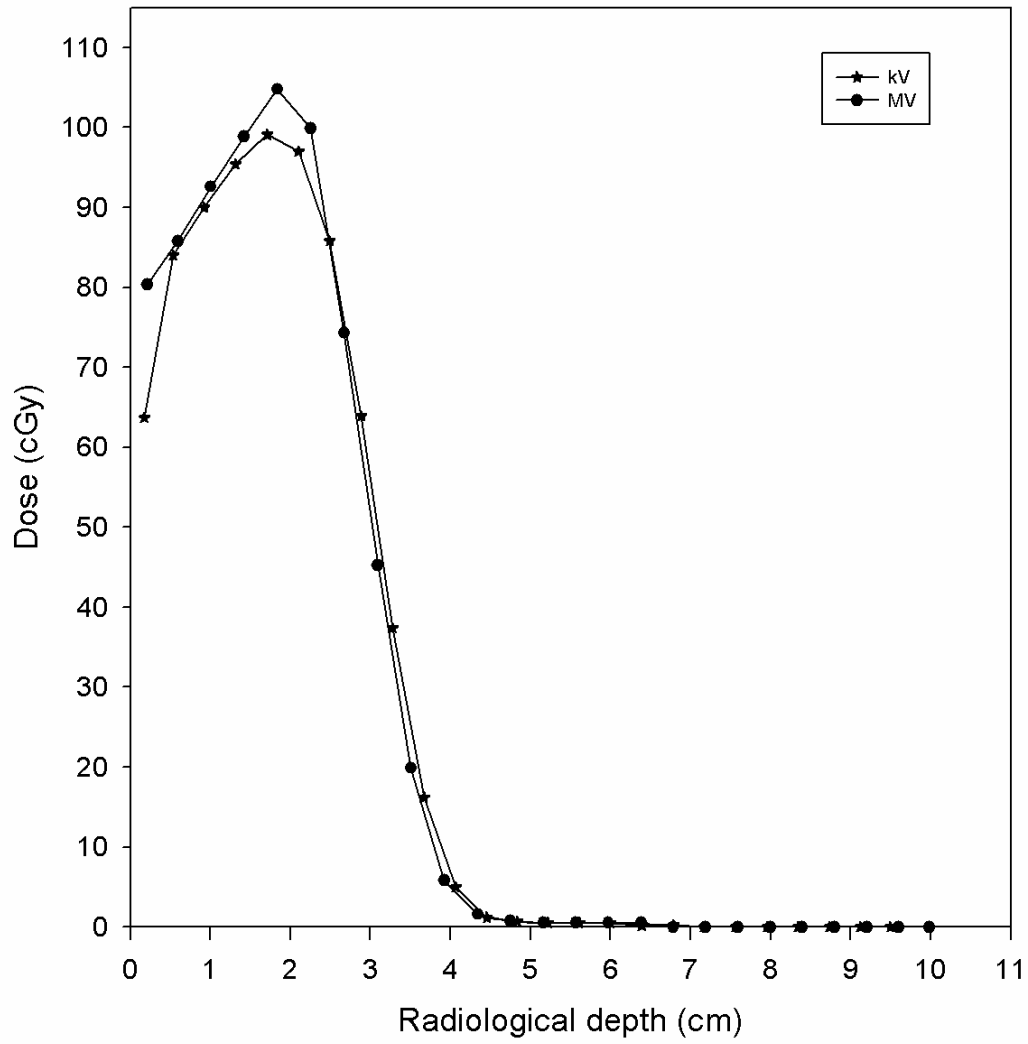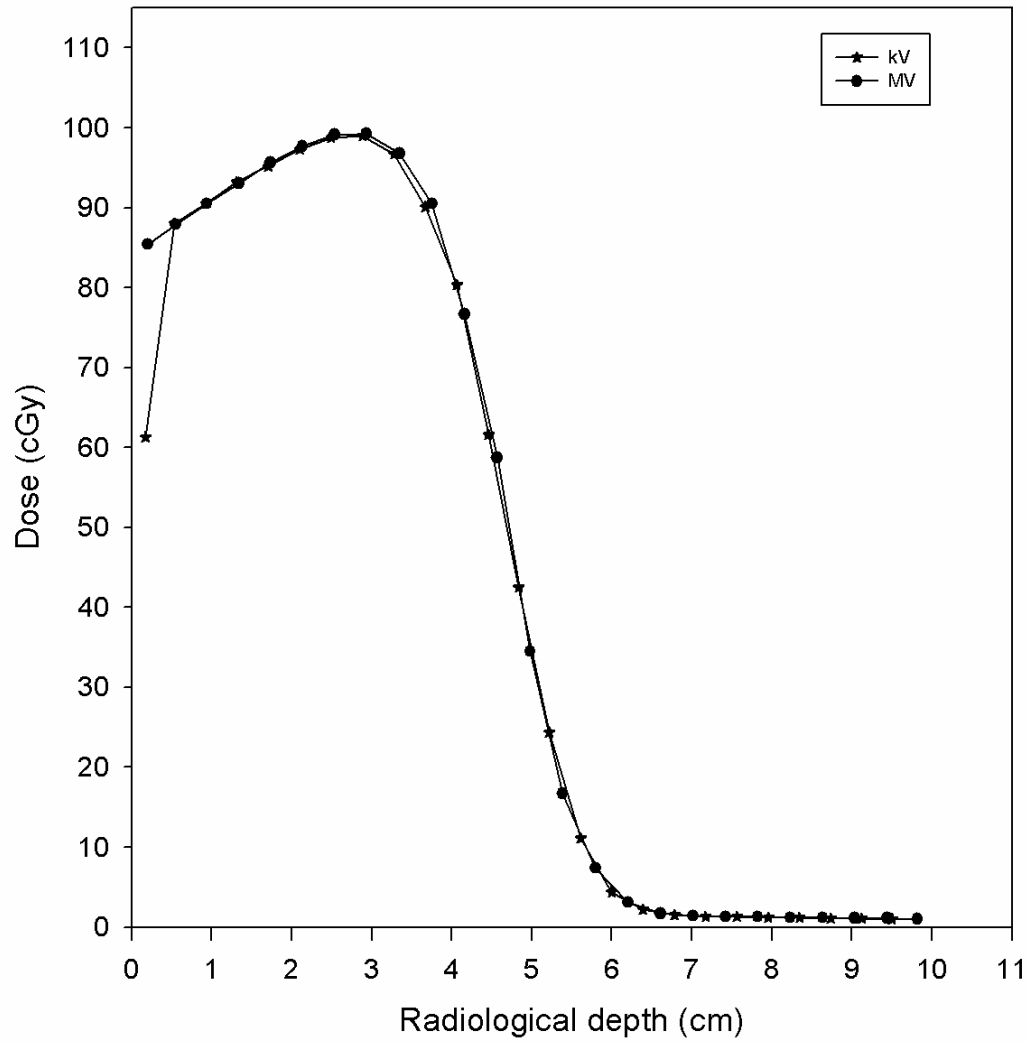
Figure 77. Dose versus radiological depth (6x6 cm^2 opening, 12 MeV).

Figure 78. Dose versus radiological depth (6x6 cm^2 opening, 16 MeV).

Figure 79. Dose versus radiological depth (10×10 cm^2 opening, 6 MeV).

Figure 80. Dose versus radiological depth (10×10 cm^2 opening, 9 MeV).

Figure 81. Dose versus radiological depth (10x10 cm^2 opening, 12 MeV).

Figure 82. Dose versus radiological depth ($10\text{x}10$ cm^2 opening, 16 MeV).
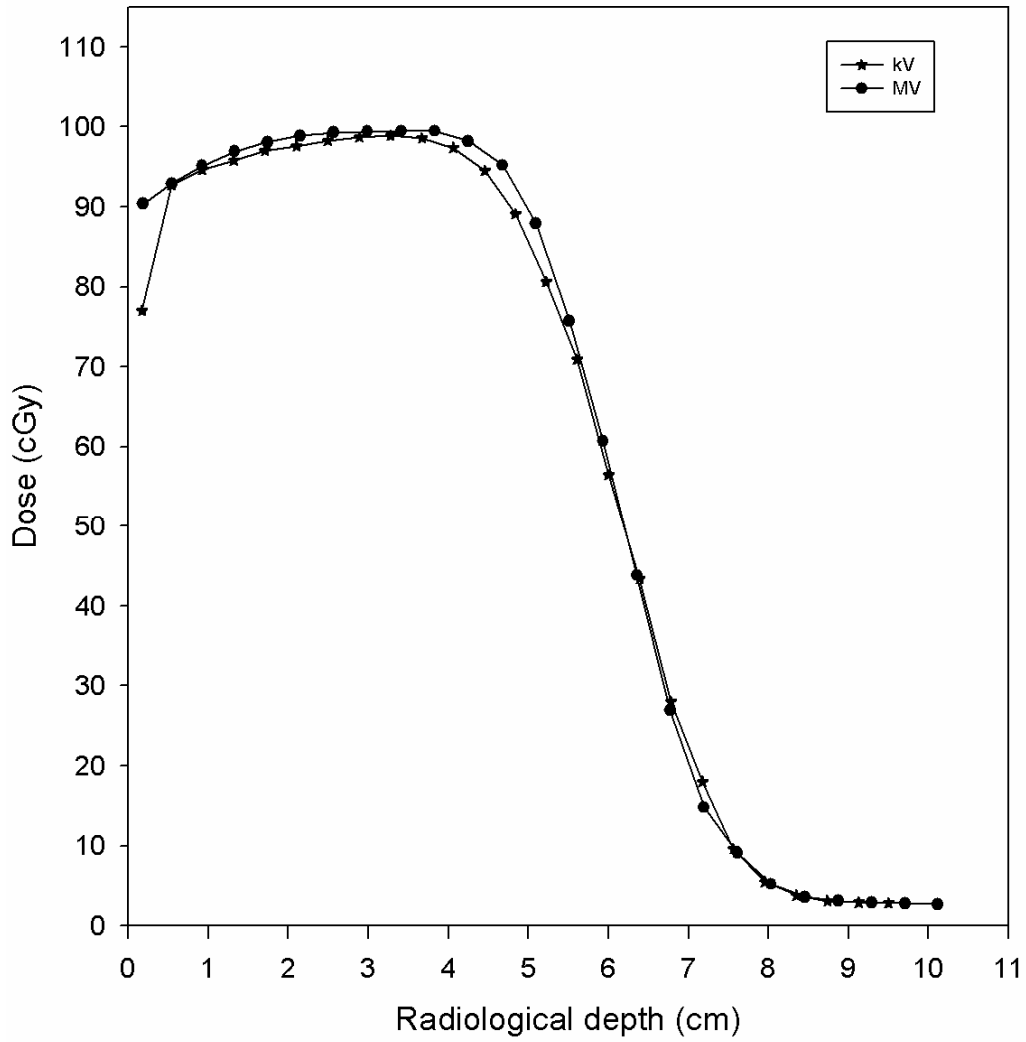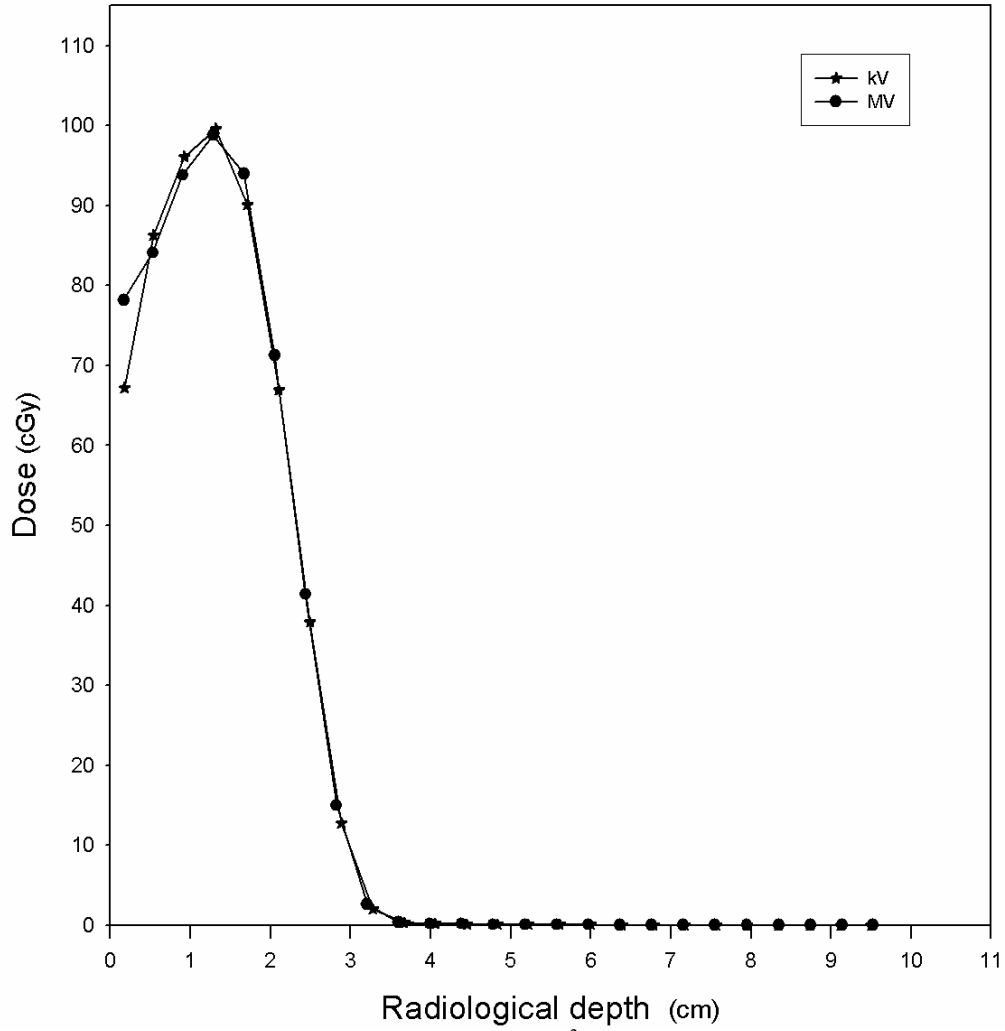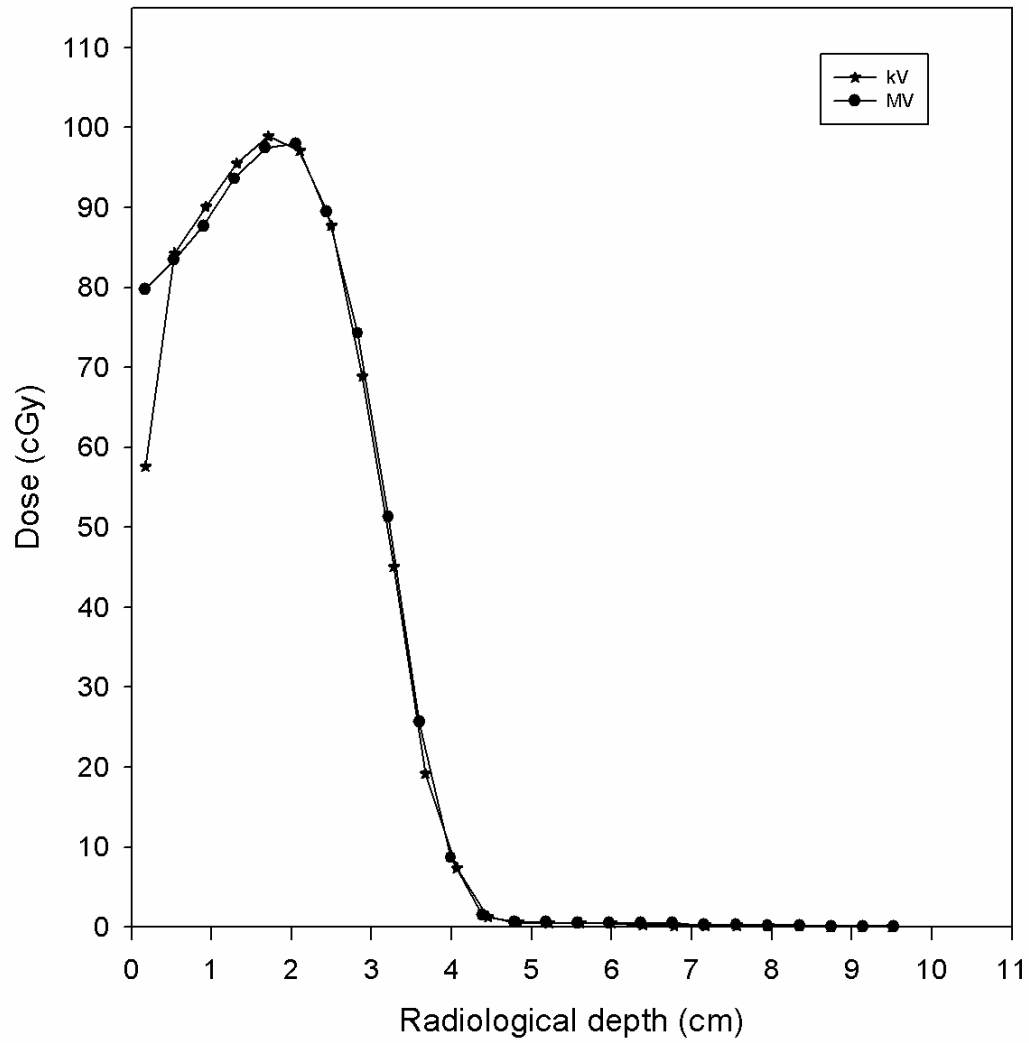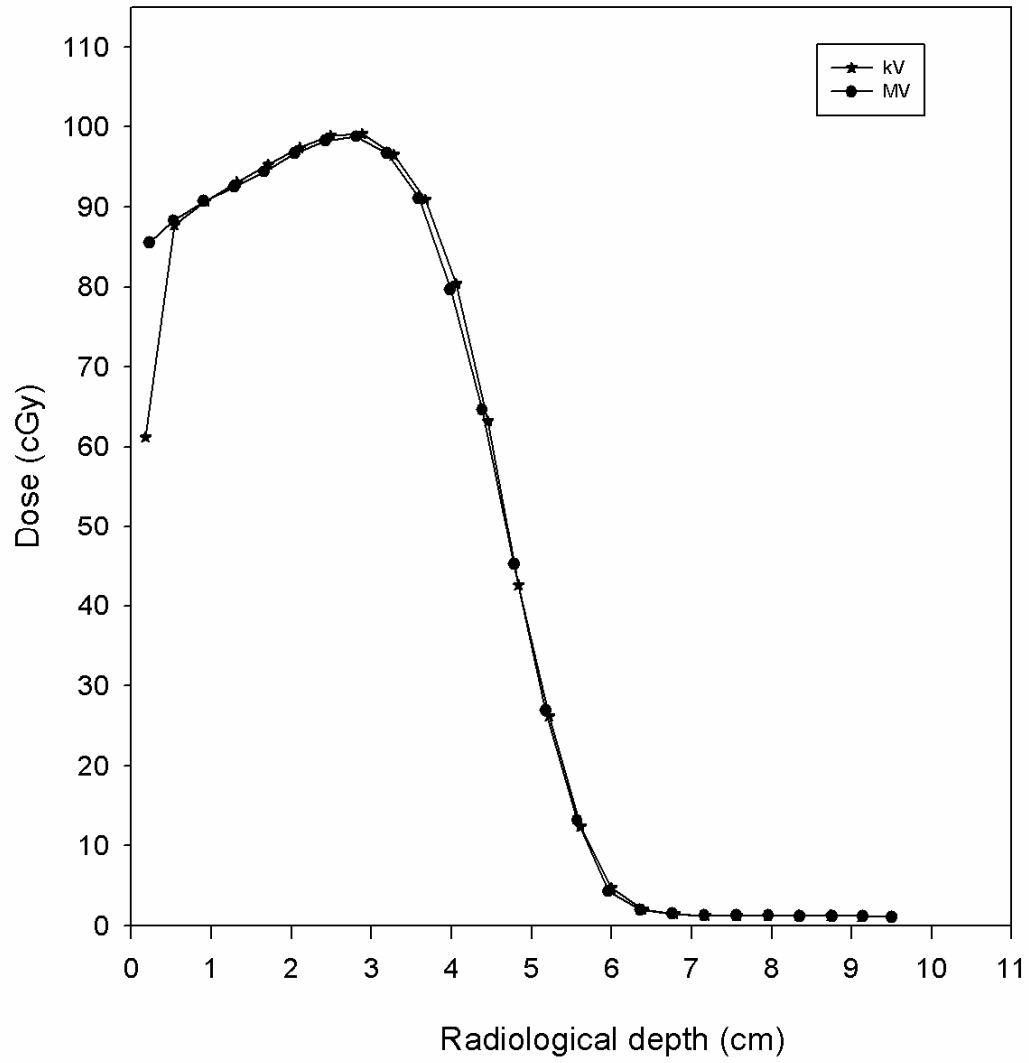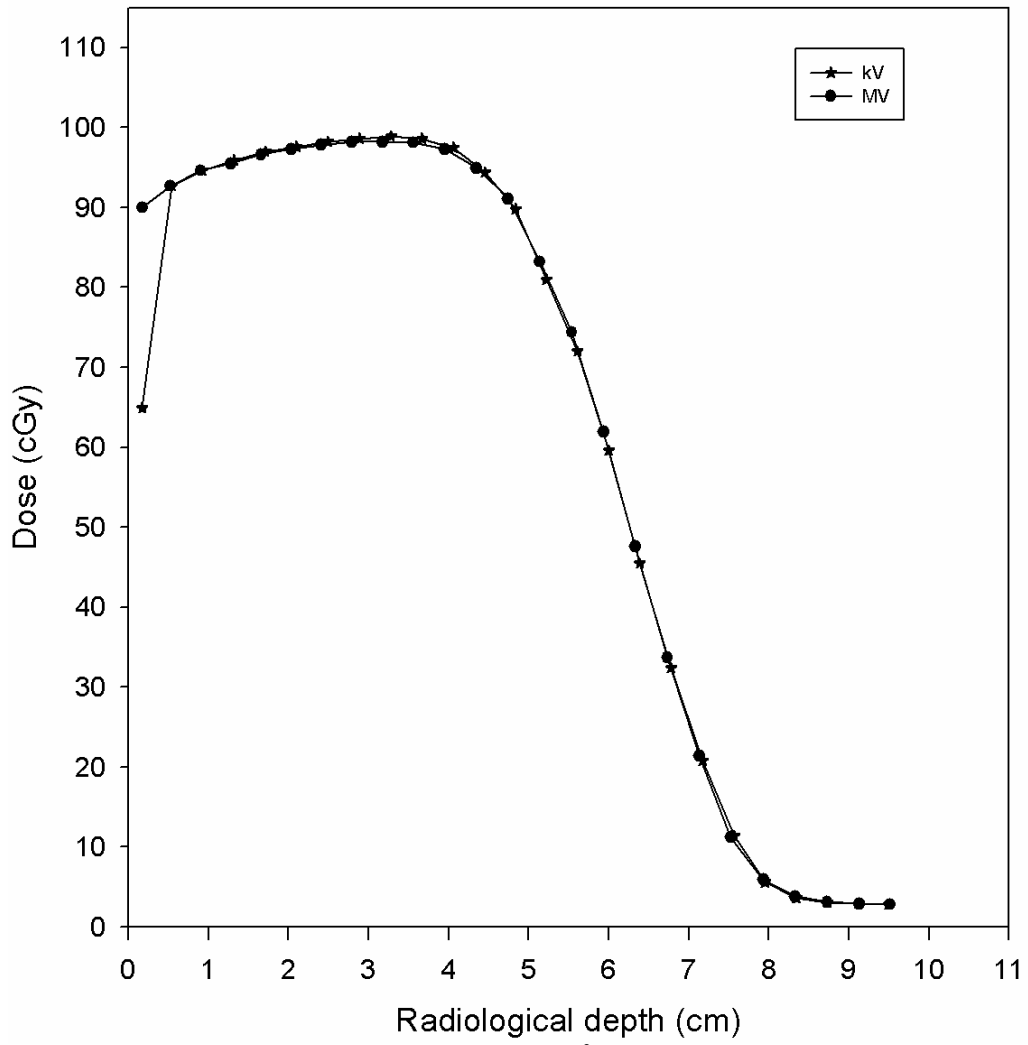
6.4.1 Shifted MVCT curves

The dose shift to shallower depths for the small and medium openings and the shift to greater depth for the large opening are due to CT number distortions in the images caused by the presence of Cerrobend®. These distortions in the CT numbers produce distortions in the density of the material, which cause the electron beam penetration to change depending on the amount of distortion. The density versus depth plots shown in section 6.3.4 clearly reveal this effect. Displaying radiological depth versus dose removes the effect of distortions in the densities of the phantom. The plots of dose versus radiological depth confirm that most, but not all, of the dose differences result from these distortions. For the medium and large openings, these plots are almost identical for the MVCT and kVCT images, confirming that these dose differences are due almost entirely to density distortions in the MVCT images of the phantom.

For the small opening, these density distortions contribute to the dose differences but are not the only effect. Comparing the plots of dose versus radiological depth (Figs 75-77) to the corresponding plots of dose versus depth (Figs 52-54) show that removing the distortions in the phantom MVCT numbers improves the agreement. However, significant differences remain. The remaining significant differences are caused by the second issue, that of peaking.

6.4.2 Peaking in the small opening data

The residual dose differences are attributed to distortions in the images of the skin collimation in the MVCT scans. In the MVCT images, the internal edges of the skin collimation appear slightly rounded, when they are in fact straight (Figure 46). This artificial rounding causes the dose calculation algorithm to overestimate the number of electrons scattered from this inner edge. The extra scattered electrons deposit their dose at superficial depths, including D_{max}, and so do not penetrate to the depth that they would if the collimation were accurately represented. This additional scattering from the edge of the collimation can be seen in the isodose plots of the larger openings as well. There are two hot spots located lateral to the central-axis in every one of the isodose plots for the 6x6 cm^2 and 10x10 cm^2 opening beams except for that of the 16 MeV beam, 10x10 cm^2 opening size (Figs 55-58, 59-61) . The depth dose plots for the medium and large openings are not affected simply because the width of the openings is too great for the collimator-scattered electrons to reach the center of the field. The one exception is seen in the high energy (16 MeV), with medium opening case where the electrons had enough energy to reach the central axis after being scattered off the collimator. These changes in dose from distortion in the image of the collimator are in addition to dose changes due to distortions in the image of the phantom.

6.5 Summary

Two different effects contribute to the discrepancies between MVCT computed doses and kVCT computed doses. The dominant effect is the distortion in density in the MVCT images caused by the high-density Cerrobend®. Although not readily apparent in the MVCT images, the CT numbers below the openings in the path of the beam are changed by the presence of the skin collimation. For the smallest opening, the distortion in CT numbers appears as tissue density increases of up to 10%. With increasing opening size, the CT numbers decrease, producing smaller apparent density shifts. Therefore, the electron beam penetration changes with opening size. A second effect is the distortion of the image of the skin collimation. This distortion causes increases in superficial dose and decreases in dose at depth.

Chapter 7 Conclusion

The hypothesis of this research is that using MVCT images with skin collimation for treatment planning, doses delivered from 6-16 MeV electron beams can be calculated to ±5% dose difference agreement in the uniform-dose region and ±2mm distance-to-agreement in high dose-gradient regions to doses calculated using kVCT images with manually contoured skin collimation. The uniform dose region is defined as those doses $\geq$90% of the maximum dose along the central-axis for a 10x10 cm^2 open field at 100 cm SSD and the high dose-gradient region is defined as 10%<doses<90% of the maximum dose along the central-axis for a 10x10 cm^2 open field at 100 cm SSD.

This hypothesis was tested with five specific aims and two related but distinct goals. Aims 2 and 3 tested the ability of MVCT images to be used for treatment planning with electron beams without the presence of skin collimation. Aim 5 tested the ability of MVCT images to be used for treatment planning with electron beams with skin collimation present.

It was found that doses calculated using MVCT images agreed well with doses calculated using kVCT images when there was no skin collimation. It was sufficiently accurate to meet the criteria of the hypothesis for the simple geometry phantom and the head phantom. It failed for the patient case, but that may have been due to changes in anatomy during the 2 month interval between the scans.

When skin collimation was introduced into the MVCT images, the distortions in the phantom density and distortions in the image of the skin collimation produced errors that were greater than ±5% and maximum DTAs that were greater than ±2 mm in most cases.

The results of this research negate the hypothesis that using MVCT images for treatment planning, doses delivered from 6-16 MeV electron beams can be calculated with the presence of skin collimation to ±5% dose difference in the uniform dose region and ±2 mm DTA in dose gradient regions. Therefore, the hypothesis must be rejected.

References

Coolens, C., and P.J. Childs 2003 Calibration of CT Hounsfield units for radiotherapy treatment planning of patients with metallic hip prostheses: the use of the extended CT scale *Phys. Med. Biol.* **48** 1591-1603.

Hogstrom K. R. and Steadham R. S. Electron beam dose computation. In: J. Palta and T. R. Mackie (ed.), Teletherapy: Present and Future – 1996 Proceedings of the Summer School of the AAPM, pp. 137-174, Vancouver: Advanced Medical Publishing, 1996.

Hogstrom, K. R. Treatment Planning in Electron Beam Therapy. In: J. L. Meyer and J. M. Vaeth (ed.), The Role of High Energy Electrons in the Treatment of Cancer, pp. 30-52, Karger, San Francisco 1991.

Meeks, S., K. Langen, T. Wanger, T. Willoughby, and P. Kupelian 2006 The use of MVCT images for dose calculation in the presence of metallic objects *Med. Phys.* **32** 2115.

Ozer, M., S. Hui, B. Gerbi, P. Higgins, Alaei Parham, and K. Dusenberry 2006 Extended range CT-value analysis in megavoltage CT imaging and therapy *Med. Phys.* **33** 2219.

Ruchala, K. J., G. H. Olivera, E. A. Schloesser, and T. R. Mackie 1999 Megavoltage CT on a tomotherapy system *Phys. Med. Biol.* **44** 2597-2621.

Siddon, Robert L 1985 Calculation of the radiological depth *Med. Phys*. **12(1)** 84-87.

Tapley, Norah duV., Ed. "Clinical Applications of the Electron Beam." New York: John Wiley & Sons, 1976.

Yazdia, Mehran, Luc Gingras, and Luc Beaulieu 2005 An adaptive approach to metal artifact reduction in helical computed tomography for radiation therapy treatment planning: Experimental and clinical studies *Int. J. Radiation Oncology Biol. Phys.* **62** 1224-1231.

Vita

Allen Beardmore was born in Pittsburgh, Pennsylvania in 1982. He grew up in Carlisle, Pennsylvania and attended college at Furman University in Greenville, South Carolina. He received his B.S. in physics from Furman in the spring of 2004 and his M.S. in medical physics from Louisiana State University in the summer of 2007. Allen is married with one child.